CONTENTS

sciendo

DOI 10.2478/ama-2019-0001

acta mechanica et automatica, vol.13 no.1 (2019)

INVESTIGATION OF GAS FOIL BEARINGS WITH AN ADAPTIVE AND NON-LINEAR STRUCTURE

Grzegorz ŻYWICA,* Paweł BAGIŃSKI*

*Department of Turbine Dynamics and Diagnostics, Institute of Fluid Flow Machinery, Polish Academy of Sciences,
ul. Fiszera 14, 80-231 Gdansk, Poland

gzywica@imp.gda.pl, pbaginski@imp.gda.pl

received 7 September 2018, revised 25 February 2019, accepted 28 February 2019

Abstract: The article discusses the results of simulation-based and experimental research carried out on gas foil bearings. Owing to the use of a set of flexible thin foils in such bearings, they exhibit certain beneficial features that cannot be found in other types of bearings. They have nonlinear operational characteristics and allow the dissipation of excess energy, thus reducing the vibration level. Moreover, gas foil bearings can self-adapt themselves to the current operating conditions by changing the shape of the lubrication gap. Therefore, they can be used to improve the dynamic performance of rotors, in particular, those operating at very high rotational speeds. This article explains the mechanisms for changes of stiffness and vibration damping in compliant components of a foil bearing. The results of the analysis of the bearing's subassemblies using advanced numerical models are presented. They are followed by conclusions that were drawn not only from these results but also from the results of the experimental research. It has been proven that the rotor supported on carefully designed foil bearings is capable of maintaining a low vibration level, even if it operates at a high rotational speed.

Key words: foil bearings, high-speed rotors, adaptive structure, non-linear stiffness

1. INTRODUCTION

Modern machines and devices have to meet increasingly higher requirements in terms of power efficiency and operational reliability. This also applies to devices used in distributed power generation, which additionally should be small in size and have a low impact on the surrounding environment (i.e., low noise and emissions). As far as cogeneration systems and trigeneration systems (in which heat energy is generated simultaneously with electricity and cold) are concerned, such requirements can easily be met by using high-speed fluid-flow machines such as microturbines (Kiciński, 2015, Kosowski et al., 2018, Włodarski, 2018). In order to enable microturbine rotors to operate at increasingly higher rotational speeds, novel bearing systems must be developed.

Foil bearings are one of the unconventional bearing systems (DellaCorte, 2012). An external lubricant supply system is not needed and such bearings are lubricated using air or a fluid situated in their immediate vicinity. Among all types of foil bearings that can be the components of a microturbine, gas foil bearings offer the greatest development potential for the future; they can be lubricated with the working medium from the thermodynamic cycle (which is the same medium that powers the microturbine). Owing to this, gas foil bearings can operate at high temperatures and high rotational speeds (even over 100,000 rpm). In comparison to rolling element bearings, which are de facto the most common type of bearings (Shen et al., 2014; Zhao et al., 2016), foil bearings have higher durability and improved vibration damping. Even though magnetic bearings can also be used in high-speed machinery (Ji et al., 2008), in particular, active magnetic bearings (Wu et al., 2018), the multi-component system of devices that are required to control the position of the rotor and a high price of such devices severely limit their usability. A somewhat new approach in the field of bearing systems is the use of slide bearings with electrorheological and magnetorheological liquids as lubricants. The application of such liquids was aimed at changing to some extent the properties of the bearings (Peng and Zhu, 2005, Urreta et al., 2010). The electromagnetic field could be used to support the bearings' operation, improving their load capacity and dynamic characteristics. Work on such bearings is, however, at an initial stage, and their use at high temperatures is rather impossible. When discussing innovative bearing systems, shape memory alloys are worth mentioning. As demonstrated by the research already carried out, these types of alloys can be used to change the properties of supports in rotor-bearing systems (Enemark et al., 2015), which allows us to actively control the characteristics of the rotating system during its operation (in a certain range).

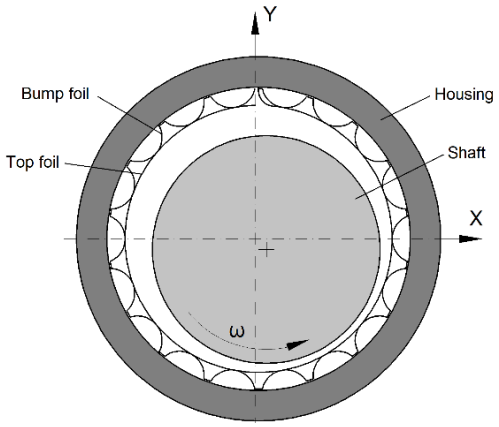

Fig. 1. The exemplary geometry of the first-generation foil bearing

All in all, foil bearings have the potential of wider utility in high-speed fluid-flow machines in the years to come. Although they

DOI 10.2478/ama-2019-0001

have a fairly simple construction (Fig. 1), their operation is associated with physical phenomena whose experimental research requires advanced measurement techniques and computer-aided simulations should be conducted using sophisticated numerical models (von Osmanski et al., 2017). To improve the vibration-damping capability of such bearings, additional elements in the form of thin foils are placed between the journal and the sleeve. They are not only capable of dissipating energy (Żywica et al., 2016a) but also enable changes in the shape of the lubrication gap during the bearing's operation, thus adapting it to the current operating conditions (Żywica et al., 2016b). The replacement of the foils makes it possible to change the stiffness of the bearing. Foils can have various thickness and the geometry of the bump foil can be modified. In this way, it is possible to alter the dynamic characteristics of the bearings and of the entire rotor-bearings system (Kiciński and Żywica, 2012). One can distinguish several generations of foil bearings (all of which have significantly different capacities), depending on the construction of the set of foils and the materials used (DellaCorte et al., 2008).

2. SELF-ADAPTIVE PROPERTIES OF FOIL BEARINGS

Thin metal foils used for the construction of foil bearings are characterized by high compliance. They change their shape depending on the current load and temperature. Because the support made of thin foils has very low inertia, it immediately reacts to dynamic excitations. The high compliance of the supporting elements makes it possible to change the properties of the foil bearings during their operation. At a certain speed (called lift-off speed) in a properly designed bearing, a thin gaseous layer forms itself between the mating elements, namely, between the journal and the top foil (Tkacz et al., 2017). Under these conditions, the bearing works wear-free. The assembly of top and bump foils should be designed in such a way that the fluid friction occurs in the widest possible ranges of speed and load. At the moment of increased static load, along with the movement of the journal towards the sleeve, the geometry of the assembly of foils should change in such a way that they become more rigid. Reacting to fast-changing dynamic loads, the top foil separated from the journal by a gas layer should move with it, and the bump foil should dissipate part of the energy of the rotating system and stabilise it. This principle of operation can be obtained thanks to the non-linear properties of the structural supporting layer. It can also be said that foil bearings have this unique capability of self-adapting themselves to demanding operating conditions (e.g., when they are subjected to external dynamic forces and/or large fluctuations of temperature). None of the classical slide bearings can withstand such operating conditions.

From the mechanical point of view, a foil bearing can be treated as the system shown in Fig. 2. This scheme includes all key subassemblies of the bearing that affect its static and dynamic properties. In general, it can be said that foil bearings resemble adaptive-passive systems for vibration reduction, which are used in various types of dynamic systems. Displacements and vibrations of the journal depend not only on characteristics of the lubrication film (which is speed-dependent) but also on the characteristics of the compliant assembly of foils, which changes as the load changes. In order to prevent high-amplitude vibrations, the assembly of foils that displays a progressive characteristic is usually used. A bearing that has such a characteristic is discussed in the following part of this article.

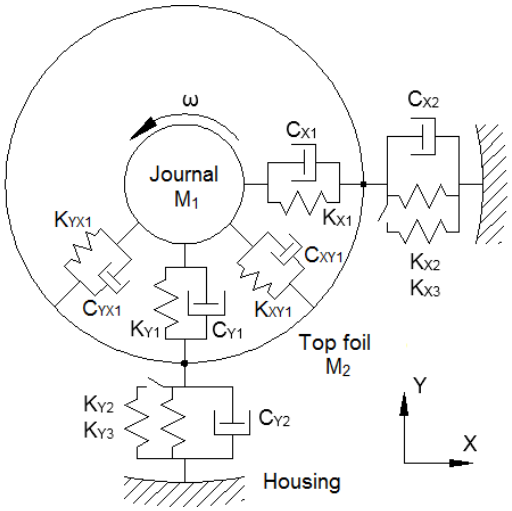

Fig. 2. Scheme of a foil bearing with the progressive stiffness (K – stiffness, C – damping, M – mass)

The use of properly formed foils, made of carefully selected materials, enables long-lasting and wear-free operation of bearings (Howard, 1999; Żywica et al., 2016a). Because foil bearings do not require external lubrication and are able to ensure stable rotor operation at high rotational speeds, they have made a major contribution to the downsizing of turbomachinery while maintaining or sometimes even exceeding the original power level. Their drawbacks are the quite high starting torque and the lack of the lubrication film at low speeds (the reason for accelerated wear). Therefore, scientists and companies continue their efforts to improve the construction of foil bearings, which could soon allow us for the better use of their application potential. The development of foil bearings took a two-track approach: experimental research and numerical calculations. Much attention is also paid to tribology-related problems (Fanning and Blanchet, 2008; Gupta et al., 2009). As a matter of fact, a foil bearing is a very difficult system for theoretical description due to many mechanical processes that can not only coexist simultaneously but can also affect each other. Simplified models of such a bearing can be used only at the initial stage of the design engineering process. In many scientific centres, methods for modelling and analysing foil bearings are constantly developed (Aksoy et al., 2015), which are then verified using the results of experimental research (Żywica, 2013; Feng et al., 2015).

The following parts of the article present the selected results of the experimental research and computer-aided simulations, which all bear witness to the exceptional properties of foil bearings. The conducted experimental research has shown that the characteristics of a foil bearing can improve during its operation. A numerical analysis of a fragment of a foil bearing allowed to better understand the processes that occur during the build-up of the external load.

3. EXPERIMENTAL INVESTIGATION

3.1. Experimental setup

The experimental research was carried out on a test rig, which had been specially designed for testing foil bearings subjected to elevated temperature (Fig. 3). A high-speed electrospindle (which

enables a smooth speed adjustment of up to 24,000 rpm) served to drive the rotor supported on two foil bearings. The bearing supports consist of two parts, which allows for easy replacement of bearing sleeves. All the elements of the test rig were attached to a steel plate. The plate was equipped with vibration isolation footers that isolated this plate from the frame bearer it is sitting on. The steel plate, rotor and bearing supports had a total mass of approx. 130 kg. The measurement system enabled to measure the following parameters: rotational speed, relative vibrations of the rotor, absolute vibrations of bearing supports and temperature distributions in bearings.

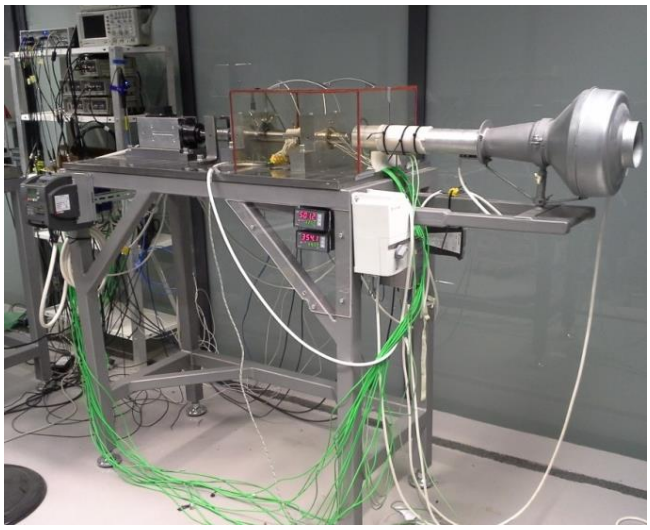

Fig. 3. The test rig for testing the rotor with foil bearings at elevated temperature

The research was conducted for the classical foil bearing, whose bump foils were made of several segments. Three bump foils were placed along the circumference of the bearing sleeve, and each of them consisted of 4 segments, obtained by a transverse cut of the foil. The geometry of the tested foil bearing was described in detail in a previous publication (Żywica et al., 2016a). The final shape of a bump foil was achieved by a two-step process. During the first stage, the bumps formed on a flat foil (Fig. 7). Next, the final curvature of a bump foil was obtained, having a radius almost equal to a radius of the hole in the bearing sleeve (Fig. 6). The nominal diameter of the tested foil bearing was 34 mm (a diameter of the journal). In order to assemble a bearing system, a journal must be pushed into a pre-assembled bearing, and such an arrangement has no radial clearance (assembly preload). After a gradual wearing-in of a bearing, when the mating foils fit smoothly, some radial clearance is obtained. The magnitude of the radial clearance depends on many factors, such as: ambient temperature, the way in which the wearing-in process proceeds, static and dynamic load, thickness of the top foil's coating and so on.

3.2. Experimental results

In the course of the research, it turned out that the dynamic and thermal characteristics of the foil bearings changed during their operation. It was the most noticeable during the run-up and run-down of the rotor. Very interesting results were obtained for the bearing with a new top foil in which the antifriction coating was wearing-in during the first seconds of the operation. A plot that presents how the temperature of the top foil of this bearing (measured in its bottom part, at the central cross-section) was changing is shown in Fig. 4. The measurement was made using a thermocouple, whose measuring junction was in contact with the top foil. The rotational speed of the rotor was increased gradually and a speed of 15,000 rpm was reached after 50 seconds. This speed was maintained until the 230th second of the measurement, and then it was reduced to 12,000 rpm. At the beginning of the measurement, the temperature of the top foil increased rapidly up to 65°C at the maximum speed. Subsequently, the temperature of the foil dropped equally quickly, and after the 150th second, it was lower than 35°C.

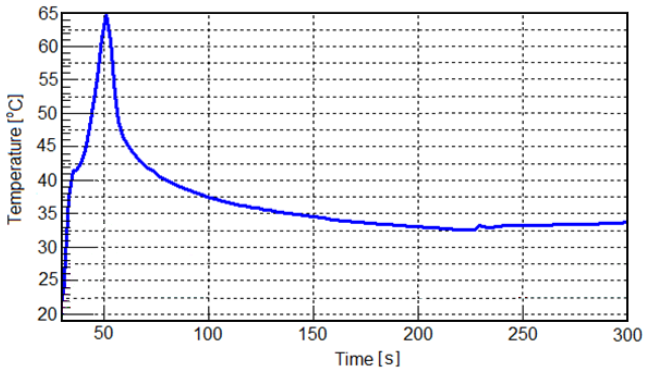

Fig. 4. Temperature of the top foil measured during wearing-in process vs. time of operation

The temperature distribution resulted from the bearing load and rotational speed. The highest load – gravitational force, was acting at the bottom of the bearing. It was noted that the increase of temperature was accompanied with higher friction torque, which impeded the start-up of the rotor. Subsequently, after wearing-in of the fop foil and journal coating, friction decreased significantly and the speed control of the electrospindle using a frequency converter was much easier.

During the discussed research, measurements of absolute vibrations of bearing pedestals and relative vibrations of the rotor were also made. The measurement results of the relative vibrations of the bearing journals showed that for the speeds lower than the lift-off speed (in the area of mixed friction), vibration amplitudes of the journals were high and reached a value of 0.4 mm (Fig. 5). After the rotor achieved a speed of 20,000 rpm, the vibration amplitude of both bearings declined significantly and remained at a very low level (about 0.04 mm). Such a low vibration level indicated very good dynamic properties of the rotating system equipped with foil bearings.

On the basis of the obtained outcomes of the research, it can also be noted that when the rotational speed of the rotor increased, the foil bearing constantly adapted itself to the ever-changing operating conditions. At low speeds, when there were no gaseous films in the bearings yet, the vibration level was quite small, which results from the very good vibration-damping capability of the thin foils. Then, when the rotational speed was increased, an increase in vibration level of the rotor could be observed until stable lubricating films formed themselves in the bearings. The largest vibration amplitudes occurred at the speeds from the range of 8,000 rpm to 10,000 rpm when the lubricating film was not stable yet and there was a physical contact between the journal and the top foil (Fig. 5). Moreover, at these speeds, the

DOI 10.2478/ama-2019-0001

rotating journal kept on rubbing itself against the antifriction coating of the top foil. The operation at these speeds is the most unfavourable for the tested foil bearing as fast wear can occur. Therefore, it is important to rapidly increase the speed of the rotor to not let it work at dangerous speeds for too long. At higher speeds, gaseous lubricating film stabilises itself in the bearing and the flexible foils adapt their shape to new operating conditions. In these conditions, the gaseous supporting layer usually has a thickness of a few to a dozen or so micrometres, which means that it is very rigid and has poor vibration-damping capability. The set of appropriately formed foils has then the role of a damping element; it enables the rotor to rotate at extremely high speeds and the vibration level is very low.

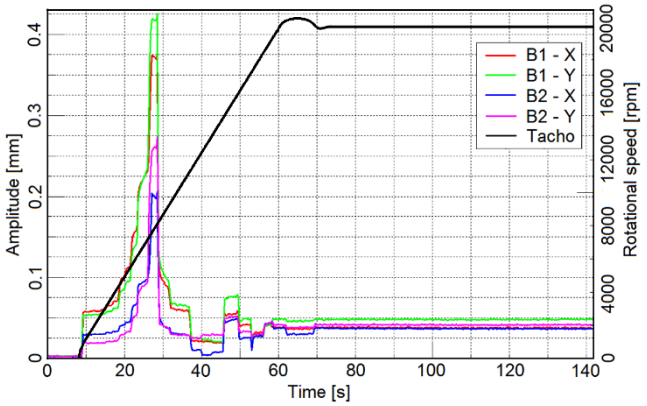

Fig. 5. The relative vibrations of the bearing journals during the run-up of the rotor up to a speed of 20,000 rpm vs. time (B1 – bearing No. 1, B2 – bearing No. 2, X and Y – horizontal and vertical direction)

4. NUMERICAL ANALYSIS OF FOIL BEARINGS

Due to the small size of the flexible elements of the foil bearing and their very small displacements during operation (at the level of micrometres), their measurement on the test rig is very difficult in practice. That is why an advanced numerical model, which had been developed using the finite element method (FEM), was used to thoroughly analyse the deformations and displacements of the top and bump foils.

4.1. Non-linear model of the foil bearing structure

An analysis of foil bearings must take into account the non-linear properties of the structural supporting layer, which arise from its geometry and the support conditions. This section of the article discusses the model of the foil bearing structure implemented in the Abaqus CAE interface and developed using the finite element method. A three-dimensional numerical model has been developed in order to represent the geometry of the actual system as faithfully as possible. In this model, the contact phenomena between all mating surfaces (including friction) were also considered. In the first-generation foil bearings, the structural supporting layer consists of elastic damping elements that are evenly spaced along the perimeter; the top foil rests on these elements. Therefore, only a fragment of the assembly of foils was implemented in the numerical model for the purposes of analyses, the purpose of which was to provide only a general explanation of the mechanical processes occurring during loading the system. The rationale behind doing so is the fact that in a majority of modern foil bearings, the above-mentioned layer consists of several sets of short bump foils (evenly spaced along the circumference) on which the top foil rests. So the properties of the whole set of foils are affected by the characteristics of its component parts, namely the characteristics of individual fragments of the bump foil. Fig. 6 demonstrates the analysed zoomed-in fragment of the structural supporting layer and its location on the sleeve.

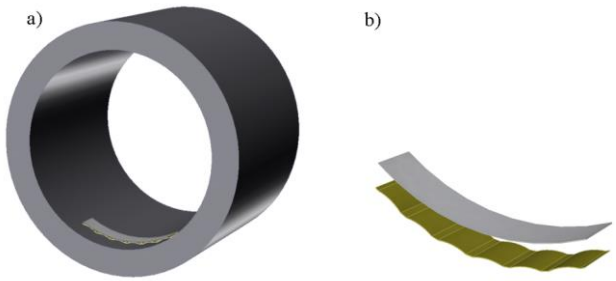

Fig. 6. The analysed fragment of the foil bearing (a – location in the bush, b – zoomed-in fragment of the top and bump foils

Simulations were conducted using the model in which the sleeve curvature was not taken into account. Such an approach is quite common in the literature (Le Lez et al., 2007). Exact dimensions of the top and bump foils, incorporated into the model that served for the analysis of the assembly of these foils, are shown in Fig. 7. It was assumed that both foils were made of steel with the following properties: ρ = 7,800 kg/m^3, E = 2.1·10^{11} Pa and ν = 0.3.

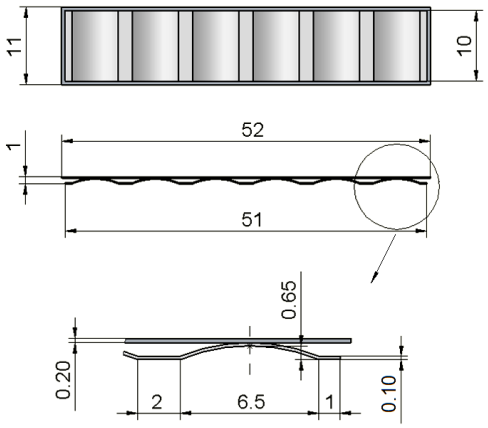

Fig. 7. Dimensions of the analysed fragment of the foil bearing

In order to carry out a deformation analysis of the assembly of foils, the following boundary conditions were adopted: (1) constraints corresponding to all the outer edge nodes of the top foil are symmetrical (such boundary conditions are used when there is a need to analyse only a fragment of a system in which displacements in the direction perpendicular to the parting plane are not important); (2) the sleeve surface on which the bump foil rests is treated as infinitely rigid (account has to be taken of the fact that very considerable difference exists between the stiffness of thin steel foils and of the sleeve made of solid material); (3) displacements of the one end of the bump foil were limited by fixing all

degrees of freedom, thus creating a rigid connection with the sleeve; (4) surface-to-surface contact elements were used to model contact between the upper surface of the bump foil and the lower surface of the top foil as well as between the lower surface of the top foil and the surface of the sleeve; (5) coefficient of friction was set to 0.1.

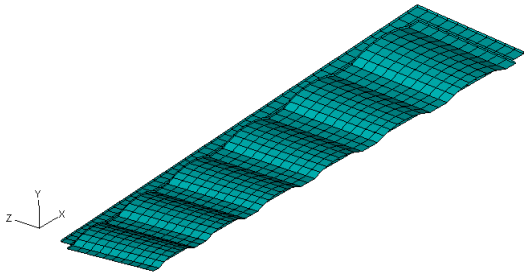

Fig. 8. FEM model of the assembly of foils

Figure 8 presents a discrete model of the assembly of foils, obtained after the optimisation of the FEM mesh. The accuracy and time of calculations were the optimisation criteria used. Three-dimensional hexahedral finite elements of the type C3D8R were employed. These are eight-node brick elements with reduced integration. Such elements are recommended for the analyses in which contact phenomena occur. The FEM model being discussed herein was also subjected to an experimental verification, the outcomes of which confirmed its high usefulness in predicting the properties of the structural supporting layer (Żywica, 2013). Some other time, a model of the structural part of a foil bearing, developed in a similar manner, was used for the simulation analysis aimed, among other things, to investigate the impact of various parameters on the properties of the structural supporting layer of a foil bearing, taking into account such parameters as the foil thickness, the number of bumps and their geometry, properties of the construction material and the coefficient of friction. Similar analyses are often done at the development stage of new foil bearings and allow for their optimisation, thus narrowing the scope of experimental tests to be carried out.

4.2. Predicted characteristics of foil bearings

In this section of the article, we would like to take a closer look at the foil bearing's structure and its geometric nonlinearity that has a very significant impact on both static and dynamic properties of each rotating system equipped with such a bearing. It turns out that the stiffness of the tested bearing can change greatly during its operation and is strongly dependent on the level of loading (Fig. 9). In the case study in question, the assembly of foils was subjected to the pressure that acted on the top foil. The same process of loading the foils occurs in a real foil bearing after a gaseous lubricating film formed itself. During the analysis, the pressure was higher than in a real foil bearing (it usually does not exceed 0.2 MPa), and this approach allowed to determine the characteristics in a broader range. Such a high pressure may only occur for a short period of time, for example, as a result of dynamic loads. The curve that shows the displacement of the top foil is almost linear for low pressure, but after exceeding a value of 0.35 MPa, its character changes. A similar change can be observed when the load was increased to 0.65 MPa, which means that the stiffness of the assembly of foils had increased even more.

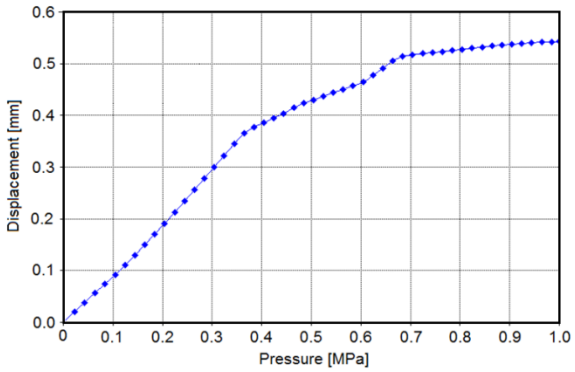

Fig. 9. Displacement of the top foil vs. load

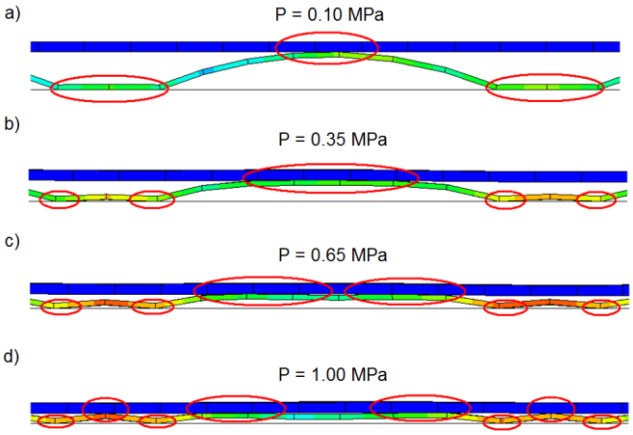

Fig. 10. The occurrence of additional contact points between the top and bump foils, according to the load (a–d)

A thorough analysis of deformations of the assembly of foils (using the developed FEM model) shed some light on this anomaly. It turned out that these deformations depend upon the level of load and are related directly to the way in which the top and bump foil interact with each other (Fig. 10). As the load increases, a higher number of support points between the mating foils appear and the higher the load, the more support points occur (Fig. 10b and Fig. 10c). At the highest load, the bump foil became nearly flat (Fig. 10d), which means that the system has a very high stiffness. The same can be observed at a lower load when thinner foils are used. This progressive nature of the structural supporting layer is beneficial because displacements of the bearing journal decrease as the load increases. This fact also has a good effect on the accuracy of the shaft alignment. The analysed process of loading is irreversible, as part of the energy of the system is dissipated as a result of friction. The bump foil is fixed on one end only, and thus, the pressure exerted by the top foil causes the bump foil to move along the surface of the sleeve. This has a beneficial effect on the dynamics of the rotor, because it reduces the vibration level. It can even be said that the shape of the bump foil allows the rigidity of the support to adjust itself to the acting load. In this way, one can explain why the bearing was able to adjust itself to the current operating conditions of the rotor, what was observed during the experimental research. Due to the high compliance of the structural supporting layer at lower loads, there was no direct contact between the journal and the top foil because the stiffness of the thin gaseous lubricating film was higher than the stiffness of the structure. A high rotational speed must, however, be considered as one of the conditions for the appearance of a stable lubricating film.

5. CONCLUSIONS

The article discusses selected issues related to distinctive features of gas foil bearings. Particular attention was paid to the self-adaptation capability of such bearings to the current operating conditions and their non-linear properties. Selected results of the experimental and computational research were presented and discussed. Results of the experimental research have shown that both dynamic and thermal characteristics of gas foil bearings can change significantly during the operation of a turbomachine. Simulations, on the other hand, allowed to improve knowledge and understanding of mechanical phenomena in which structural components of bearings play a key role. The performed analyses are also proof that the stiffness of a foil bearing can be modified to a very large extent, which greatly facilitates adjusting its characteristics to a particular rotating system. A foil bearing with an active regulation of its stiffness during operation is one of the new areas of research. It can be done using smart materials and electronic control systems. Work on these issues is already ongoing and will be continued by the authors of this article (Lubieniecki et al., 2016).

Gas foil bearings have some distinctive properties that are unheard of in other bearing types. The structural supporting layer of such a bearing has a progressive stiffness, which means that its deformations decrease progressively as the load increases. The main advantage of a foil bearing is the capability of adjusting itself to the load conditions. This capability has been verified experimentally, namely, it was observed that the vibration level of bearing journals was very low at high rotational speeds. Even though there was a sharp increase in the bearing temperature and in the vibration amplitude during the run-up of the rotor (observed within a very narrow speed range), the system exhibited very good dynamic properties after the speed was further increased. That is why foil bearings are increasingly being used in newly designed fluid-flow machinery equipped with lightly loaded rotors that rotate at high speeds.

REFERENCES

1. **Aksoy S., Aksit M.F.** (2015), A fully coupled 3D thermo-elastohydrodynamics model for a bump-type compliant foil journal bearing, *Tribology International*, 82, 110–122.
2. **DellaCorte C.** (2012), Oil-Free shaft support system rotordynamics: Past, present and future challenges and opportunities, *Mechanical Systems and Signal Processing*, 29, 67–76.
3. **DellaCorte C., Radil K.C., Bruckner R.J., Howard A.** (2008), Design, Fabrication, and Performance of Open Source Generation I and II Compliant Hydrodynamic Gas Foil Bearings, *Tribology Transactions*, 51(3), 254–264.
4. **Enemark S., Savi M.A., Santos I.F.** (2015), Experimental analyses of dynamical systems involving shape memory alloys, *Smart Structures and Systems*, 15(6), 1521–1542.
5. **Fanning C.E., Blanchet T.A.** (2008), High-temperature evaluation of solid lubricant coatings in a foil thrust bearing, *Wear*, 265, 1076–1086.
6. **Feng K., Hu J., Liu W., Zhao X., Li W.** (2015), Structural characterization of a novel gas foil bearing with nested compression springs: analytical modeling and experimental measurement, *ASME Journal of Engineering for Gas Turbines and Power*, 138(1), 012504–11.
7. **Gupta S., Filimonov D., Zaitsev V., Palanisamy T., El-Raghy T., Barsoum M.W.** (2009), Study of tribofilms formed during dry sliding of Ta2AlC/Ag or Cr2AlC/Ag composites against Ni-based superalloys and Al2O3, *Wear*, 267, 1490–1500.
8. **Howard S.A.** (1999), Rotordynamics and design methods of an oil-free turbocharger, *Tribology Transactions*, 42(1), 174–179
9. **Ji J.C., Hansen C.H., Zander A.C.** (2008), Nonlinear dynamics of magnetic bearing systems, *Journal of Intelligent Material Systems and Structures*, 19(12), 1471–1491.
10. **Kiciński J.** (2015), The dynamics of microturbines lubricated using unconventional agents, *Bulletin of the Polish Academy of Sciences: Technical Sciences*, 63(2), 369–377.
11. **Kiciński J., Żywica G.** (2012), The numerical analysis of the steam microturbine rotor supported on foil bearings, *Advances in Vibration Engineering*, 11(2), 113–119.
12. **Kosowski K., Piwowarski M., Stępień R., Włodarski W.** (2018), Design and investigations of the ethanol microturbine, *Archives of Thermodynamics*, 39(2), 41–54.
13. **Le Lez S., Arghir M., Frene J.** (2007), Static and dynamic characterization of a bump-type foil bearing structure, *Journal of Tribology*, 129, 75–83.
14. **Lubieniecki M., Roemer J., Martowicz A., Bagiński P., Żywica G., Uhl T.** (2016), An experimental evaluation of the control methodology for distributed actuators integrated within a foil bearing, *ICAST2016, 27th International Conference on Adaptive Structures and Technologies*, New York, USA.
15. **Peng J., Zhu K.-Q.** (2005), Hydrodynamic characteristics of ER journal bearings with external electric field imposed on the contractive part, *Journal of Intelligent Material Systems and Structures*, 16(6), 493–499.
16. **Shen C., Wang D., Liu Y., Kong F., Tse P.W.** (2014), Recognition of rolling bearing fault patterns and sizes based on two-layer support vector regression machines, *Smart Structures and Systems*, 13(3), 453–471.
17. **Tkacz E., Kozanecki Z., Kozanecka D., Łagodziński J.** (2017), A self-acting gas journal bearing with a flexibly supported foil – Numerical model of bearing dynamics, *International Journal of Structural Stability and Dynamics*, 17(5), 1740012.
18. **Urreta H., Leicht Z., Sanchez A., Agirre A., Kuzhir P., Magnac G.** (2010), Hydrodynamic bearing lubricated with magnetic fluids, *Journal of Intelligent Material Systems and Structures*, 21(15), 1491–1499.
19. **Von Osmanski S., Larsen J.S., Santos I.F.** (2017), A fully coupled air foil bearing model considering friction – Theory & experiment, *Journal of Sound and Vibration*, 400, 660–676.
20. **Włodarski W.** (2018), Experimental investigations and simulations of the microturbine unit with permanent magnet generator, *Energy*, 158, 59–71.
21. **Wu R.Q., Zhang W., Yao M.H.** (2018), Nonlinear dynamics near resonances of a rotor-active magnetic bearings system with 16-pole legs and time varying stiffness, *Mechanical Systems and Signal Processing*, 100, 113–134.
22. **Zhao Y., Zhang B., An G., Liu Z., Cai L.** (2016), A hybrid method for dynamic stiffness identification of bearing joint of high speed spindles, *Structural Engineering and Mechanics*, 57(1), 141–159.
23. **Żywica G.** (2013), The dynamic performance analysis of the foil bearing structure, *Acta Mechanica et Automatica*, 7(1), 58–62.
24. **Żywica G., Bagiński P., Banaszek S.** (2016a), Experimental studies on foil bearing with a sliding coating made of synthetic material, *Journal of Tribology*, 138(1), 011301.
25. **Żywica G., Kiciński J., Bagiński P.** (2016b), The static and dynamic numerical analysis of the foil bearing structure, *Journal of Vibration Engineering & Technologies*, 4(3), 213–220.

The research was financed by the National Science Centre in Poland, under the research project No. 2016/21/D/ST8/01711 entitled 'Examination and modelling of anti-vibration processes occurring in high-speed bearings with variable geometry'.

sciendo

DOI 10.2478/ama-2019-0002

acta mechanica et automatica, vol.13 no.1 (2019)

MATHEMATICAL MODELLING OF STATIONARY THERMOELASTIC STATE FOR A PLATE WITH PERIODIC SYSTEM OF INCLUSIONS AND CRACKS

Volodymyr ZELENYAK*

*Department of Mathematics, Institute of Applied Mathematics and Fundamental Sciences, Lviv Polytechnic National University, S. Bandery str., 12, 79013, Lviv, Ukraine

volodymyr.zelenyak@gmail.com

received 8 November 2018, revised 3 March 2019, accepted 7 March 2019

Abstract: Two-dimensional stationary problem of heat conduction and thermoelasticity for infinite elastic body containing periodic system of inclusions and cracks is considered. Solution of the problem is constructed using the method of singular integral equations (SIEs). The numerical solution of the system integral equations are obtained by the method of mechanical quadrature for a plate heated by a heat flow, containing periodic system elliptic inclusions and thermally insulated cracks. There are obtained graphic dependences of stress intensity factors (SIFs), which characterise the distribution of intensity of stresses at the tops of a crack, depending on the length of crack, elastic and thermoelastic characteristics inclusion, relative position of crack and inclusion.

Keywords: Stress Intensity Factor, Singular Integral Equation, Inclusion, Heat Conduction, Thermoelasticity, Crack

1. INTRODUCTION

Singular integral equations (SIEs) are often applied in studying the stressed state of bodies with cracks. First, they were used only for very simple rectilinear and arcwise cuts. The construction of equations of this kind for systems of rectilinear cracks arbitrarily located in the elastic plane became a substantial step forward in this direction. The results obtained enabled the researchers to find the numerical and analytic solutions of the plane and antiplane problems of the theory of elasticity, the steady-state problems of heat conduction and thermoelasticity and the problems of bending of thin plates and gently sloping shells for domains with cuts (Panasyuk et al., 1976). Later, these results were generalised to the case of curvilinear cuts (cracks) and multiply connected domains with holes and cuts of any configuration (Savruk,1981).

However, for homogeneous bodies with cracks (cuts), the problems of thermoelasticity remain poorly investigated, and, in particular, in the available literature, one can find almost no solution for noncircular (e.g. elliptic) inclusions and especially for multicomponent bodies with cracks.

The two-dimensional problems of thermoelasticity for semi-infinite bodies with cracks have already been investigated in the literature. Thus, in particular, the thermoelastic state of a half plane containing an internal rectilinear crack was investigated, and different temperature and force conditions imposed on the crack lips and on the edge of the half plane were analysed in (Sekine, 1975; Tweed and Love, 1979). The method of SIE was used for the analysis of the plane thermoelastic state in a half space locally heated over a part of its free surface by a heat flow and containing an internal arbitrary-oriented rectilinear crack or a periodic system of cracks of this sort (Matysiak et al,1999) or internal curvilinear crack (Zelenyak and Kolyasa, 2016) .

The SIE for stationary problems of heat conduction and thermoelasticity for infinite and finite (Savruk and Zelenyak,1987) piecewise homogeneous planes weakened by curvilinear cracks with given temperature or heat flows specified on their lips are deduced by the method of integral representations of complex temperature and stress potentials. The SIE of heat conduction and thermoelasticity with special Cauchy-type kernels for a plane with thermally insulated cracks or heat-conducting cuts located in a circular foreign inclusion; for a body with thermal cylindrical inclusions and crack (Kit and Chernyak,2010); for an infinite body with two identical coplanar thermally active circular cracks (Sushko, 2013); and for a half space locally heated over a part of its free surface by a heat flow and containing an internal rectilinear crack (Kit and Ivas'ko, 2013) are deduced by the method of functions of complex variable. The mechanical problem of interaction of a curvilinear crack with a circular inclusion in an infinite elastic plane is studied in Cheesman and Santare (2000). The distribution of temperature stresses near the crack tips in three-component region (i.e. in a plane containing a foreign two-component inclusion and crack) at a constant temperature was studied in Zelenyak (2012). The two-dimensional elastic problem in a similar three-component region was presented in (Xiao and Chen, 2001). The method of SIEs was used for finding the solution of two-dimensional problems of thermoelasticity for a three-layer circular hollow cylinder weakened by a crack (Zelenyak, 2015). The solutions of the thermoelasticity problem for a plane with a crack based on the edge method (Chen et al., 2016) and the Fourier integral transform method (Choi et al., 2014) was presented.

Dynamic steady-state growth in 3D of a semi-infinite plane brittle crack in a coupled thermoelastic solid is considered. An asymptotic solution is obtained in an analytic form and subjected to a criterion of the Griffith type for the case of a compressive point force (Brock, 2016). The multiple cracks problem in an elastic half-plane is formulated into SIE using the modified complex potential with free traction boundary condition. A system of SIEs is

obtained with the distribution dislocation function as unknown and the traction applied on the crack faces as the right-hand terms (Elfakhakhre, 2017). The problem of the stress concentration in the vicinity crack tips for a crack of finite length located perpendicular to the interface of two elastic bodies – a half-plane and a strip – is considered. Using the method of generalised integral transforms, the problem reduces to the solution of an SIE with a Cauchy kernel (Rashidova and Sobol, 2017). Local frictional heating of surface of a layered plate with inclusion was investigated in Havrysh (2017, 2015).

The aim of this article is (1) to construct a two-dimensional mathematical model of the stationary problems of heat conduction and thermoelasticity for infinite elastic body containing periodic system inclusions and cracks in the form of system SIE; (2) to determine the numerical solutions to SIE (using the method of mechanical quadratures) in particular case of periodic system elliptic inclusions and thermally insulated cracks. This makes it possible to determine stress intensity factors (SIFs) at the tops of the crack, which are subsequently used to determine critical values of the heat flow at which a crack starts to grow.

2. PROBLEM STATEMENT

Consider an infinite body consisting of a matrix S and a periodic system of inclusions and cracks, and in the main band of periods of width d (along the axis Ox), there are M inclusions, bounded by smooth closed contours $L_k\left(k=\overline{1,M}\right)$ and N-M curvilinear cracks $L_k\left(k=\overline{M+1,N}\right)$, located in both the matrix and the inclusions. We assume that all contours $L_k\left(k=\overline{1,N}\right)$ do not have common points. Each contour is connected with a local coordinate system $x_kO_ky_k$ whose axis O_kx_k forms an angle α_k with the axis Ox, and the points O_k are determined in the coordinate system xOy by complex coordinates z_k^0. Bypassing the contours $L_k\left(k=\overline{1,M}\right)$ in a positive direction, the area S_k remains to the left (Fig. 1).

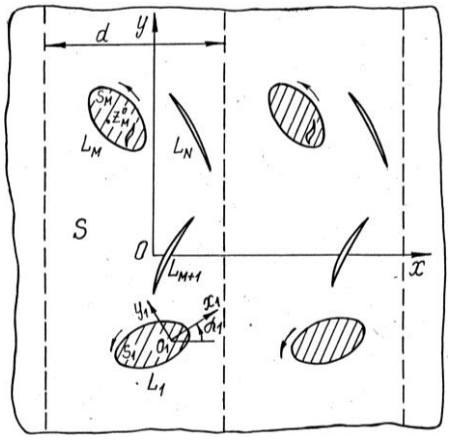

Fig. 1. Geometric scheme of the problem

Consider the problem of heat conduction with the following conditions of thermal contact. We will assume that along the closed contours, the conditions for an ideal thermal contact (temperature and heat equivalence) are given:

$$\lambda_k\frac{\partial T^+}{\partial n}=\lambda\frac{\partial T^-}{\partial n},\ T^+=T^-\ t_k\in L_k,k=\overline{1,M}, \tag{1}$$

and on the shores of cracks, heat fluxes are given:

$$\lambda_k^*\frac{\partial T^\pm}{\partial n}=\tau_k(t_k)\pm\mu_k(t_k),t_k\in L_k,k=\overline{M+1,N}. \tag{2}$$

In this case, the total amount of heat going through the contour $L=UL_k\left(k=\overline{M+1,N}\right)$ is zero, that is,

$$\sum_{k=M+1}^{N}\int_{L_k}\mu_k(t_k)\mathrm{d}s_k=0. \tag{3}$$

Here n is the outer normal to the closed contour $L_k\left(k=\overline{1,M}\right)$ or to the left face of the cut $L_k\left(k=\overline{M+1,N}\right)$; $\lambda(\lambda_k)$ is the coefficient of thermal conductivity of the matrix (inclusion S_k); $T(x,y)$ is the temperature; t_k is the complex coordinates of points on the contours L_k in local coordinate systems; s_k is the arc abscissa of the point; $\lambda_k^*=\lambda$ if the contour $L_k\left(k=\overline{M+1,N}\right)$ is located in the matrix and $\lambda_k^*=\lambda_k$ if it lies in the inclusion; the plus and minus indices indicate the boundary values of the corresponding values on the left and the right of the approach to the contour L_k.

In the problem of thermoelasticity, we assume that on the junction lines, the inclusions and the matrices $L_n\left(n=\overline{1,M}\right)$ of the stress are continuous, and the displacement has a gap:

$$[N_n(t_n)+\mathrm{i}\,T_n(t_n)]^+=[N_n(t_n)+\mathrm{i}\,T_n(t_n)]^-, \tag{4}$$

$$(u_n+\mathrm{i}v_n)^+-(u_n+\mathrm{i}v_n)^-=g_n^*(t_n),t_n\in L_n,n=\overline{1,M}. \tag{5}$$

Suppose that the plane is subjected to the action of a stationary temperature field $T(x,y)$. Assume that in the process of deformation, the crack lips are not in contact and they have a self-equilibrium load:

$$[N_n(t_n)+\mathrm{i}\,T_n(t_n)]^\pm=p_n(t_n),\ t_n\in L_n\ ,n=\overline{M+1,N}. \tag{6}$$

In relations (4), (5) and (6), $N_n(t_n)$ and $T_n(t_n)$ are the normal and tangential components of the load and u_n,v_n are the components of displacement.

3. THE PROBLEM SOLUTION

3.1. The system of integral equations of the problem of heat conduction

We represent the temperature in the form $\mathrm{T(x,y)}=\mathrm{Ref(z)},\mathrm{z}\in\mathrm{S}$ and use the complex temperature potential $\mathrm{F(z)}=\mathrm{f'(z)}$ (Savruk,1981).

$$F(z)=F_0(z)+\frac{1}{\mathrm{id}}\sum_{k=1}^{N}\int_{L_k}H_k(t_k)\mathrm{ctg}\left[\frac{\pi}{d}(T_k-z)\right]\mathrm{d}t_k, \tag{7}$$

$$H_k(t_k)=\gamma_k'(t_k)+i\mu_k(t_k)e^{-i\theta_k},\gamma_k'(t_k)=0\left(k=\overline{1,M}\right).$$

Here $\mathrm{f_0(z)}=\int\mathrm{F_0(z)dz}$ is the potential that determines the temperature field $T_0(x,y)$ in a continuous homogeneous plane without inclusions, and the function $T_0(x,y)$ is periodic with respect to the coordinate x with period d.

By satisfying the boundary conditions (1) and (2) with the help of the complex temperature potential (7), we obtain in the heat conduction problem the system of N SIEs of the first and second kinds for the N unknown functions $\mu_k(t_k)\left(k=\overline{1,M}\right)$ on the contours of inclusions and $\gamma_k'(t_k)\ \left(k=\overline{M+1,N}\right)$ on the contours of cracks:

$$i\delta_n H_n(t_n')e^{i\theta_n'} - \frac{1}{d}\sum_{k=1}^{N}\int_{L_k}\mathrm{Im}[K_{\mathrm{nk}}(t_k,t_n')H_k(t_k)\mathrm{d}t_k] =$$

$$= (\delta_n - 1)\tau(t_n')/\lambda_n^* + \Delta_n \mathrm{Im}\left[F_0(T_n')e^{i(\theta_n'+\alpha_n)}\right], \quad (8)$$

$$t_n' \in L_n, n = \overline{1,N}.$$

Here $\delta_n = 1$ for $n = \overline{1,M}$ and $\delta_n = 0$ for $n = \overline{M+1,N}$, $T_n' = t_n' e^{i\alpha_n} + z_n^0$,

$$K_{\mathrm{nk}}(t_k,t_n') = \frac{\Delta_n}{i}\mathrm{ctg}\left[\frac{\pi}{d}(T_k - T_n')\right]e^{i(\theta_n'+\alpha_n)},$$

$$\Delta_n = ((\lambda_n - \lambda)/(\lambda_n + \lambda) - 1)\delta_n + 1.$$

The solution of system (8) must satisfy the conditions

$$\int_{L_n}\gamma_n'(t_n)\mathrm{d}t_n = 0, n = \overline{M+1,N}, \quad (9)$$

guaranteeing continuity of temperature in traversing the contours of cracks. Under condition (9), the system of integral equations (8) for its arbitrary right-hand side has a unique solution in the class of the functions (Savruk, 1981) $\gamma_k'(t_k) \in H$, $t_k \in L_k$ $\left(k = \overline{1,M}\right)$ *and* $\gamma_k'(t_k) \in H^*$, $t_k \in L_k$ $\left(k = \overline{M+1,N}\right)$.

Note that the choice of the complex potential in form (7) ensures the identical satisfaction of the second equality in condition (1) based on such a choice of analytic continuation from the matrix region into the inclusion region, in which for the approach to the left and right of the contour of inclusion temperatures are equal.

3.2. The system of integral equations of the problem of thermoelasticity

Complex stress potentials can be represented in the form (Savruk,1981):

$$\Phi(z) = \frac{1}{2d}\sum_{k=1}^{N}\int_{L_k} Q_k(t_k)\mathrm{ctg}\left[\frac{\pi}{d}(T_k - z)\right]e^{i\alpha_k}\mathrm{d}t_k, \quad (10)$$

$$\Psi(z) = \frac{1}{2d}\sum_{k=1}^{N}\int_{L_k}\overline{Q_k(t_k)}\mathrm{ctg}\left[\frac{\pi}{d}(T_k - z)\right]e^{-i\alpha_k}\overline{\mathrm{d}t_k} -$$

$$-\begin{Bmatrix}\mathrm{ctg}\left[\frac{\pi}{d}(T_k - z)\right] + \\ -\frac{\pi}{d}\left(\overline{T_k} - T_k + z\right)\mathrm{cosec}^2\left[\frac{\pi}{d}(T_k - z)\right]\end{Bmatrix} Q_k(t_k)e^{i\alpha_k}dt_k,$$

where:

$$Q_k(t_k) = \begin{cases} g_k(t_k), t_k \in L_k, k = \overline{1,M}; \\ g_k'(t_k) + \dfrac{i\beta_*}{1+\chi_*}[f^+(t_k) - f^-(t_k)], t_k \in L_k, \end{cases}$$

$k = \overline{M+1,N}$.

We will assume that unknown functions $\mathrm{g_k'(t_k)}$ are sought in the class of the Hölder functions with integrable singularities at the tips of cracks: $g_k(t_k) \in H\left(k = \overline{1,M}\right)$, $g_k'(t_k) \in H^*\left(k = \overline{M+1,N}\right)$. The functions $\mathrm{f^{\pm}(t_k)}$ are the boundary values of the potential $\mathrm{f(z)}$.

By satisfying the boundary conditions (5) and (6) with the help of the complex potentials (10), we obtain in the problem of thermoelasticity, the system of *N* SIEs of the first and second kinds for the *N* unknown functions $Q_k(t_k)$ on the contours of inclusions $\left(\mathrm{k} = \overline{1,\mathrm{M}}\right)$ and cracks $\left(\mathrm{k} = \overline{\mathrm{M}+1,\mathrm{N}}\right)$:

$$A_n Q_n(t_n') + \frac{1}{2d}\sum_{k=1}^{N}\int_{L_k}\begin{bmatrix}K_{nk}(t_k,t_n')Q_k(t_k)dt_k + \\ +L_{nk}(t_k,t_n')\overline{Q_k(t_k)dt_k}\end{bmatrix}$$

$$= R_n(t_n'), t_n' \in L_n, n = \overline{1,N}, \quad (11)$$

where

$$K_{\mathrm{nk}}(t_k,t_n') = e^{i\alpha_k}\begin{Bmatrix}B_n\mathrm{ctg}\left[\frac{\pi}{d}(T_k - T_n')\right] - \\ -D_n\frac{\overline{dt_n'}}{dt_n'}\mathrm{ctg}\left[\frac{\pi}{d}(T_k - T_n')\right]e^{-2i\alpha_n}\end{Bmatrix},$$

$$L_{\mathrm{nk}}(t_k,t_n')$$

$$= -D_n e^{-i\alpha_k}\begin{Bmatrix}\left(1 - \frac{\overline{dt_n'}}{dt_n'}\right)\mathrm{ctg}\left[\frac{\pi}{d}(T_k - T_n')\right] \\ -\frac{\pi}{d}\left(T_k - T_n' + \overline{T_n'} - \overline{T_k}\right) \\ \times\frac{\overline{dt_n'}}{dt_n'}\mathrm{cosec}^2\left[\frac{\pi}{d}(T_k - T_n')\right]\mathrm{e}^{-2i\alpha_n}\end{Bmatrix},$$

$A_n = i\delta_n[1 + \chi_n + \Gamma_n(1+\chi)]/2$, $B_n = (\chi_n - \Gamma_n\chi - 1)\delta_n + 1$, $D_n = (2 - \Gamma_n)\delta_n - 1, \Gamma_n = G_n/G$,

$R_n(t_n') = [\Gamma_n\beta^+ f^-(T_n') - \beta_n^t f^+(T_n') + 2G_n g_n'(t_n')]\delta_n + (1 - \delta_n)p(t_n')$.

Here is the designation $\chi = (3-\mu)/(1+\mu)$, $\beta^t = \alpha^t E(1+\mu)$, $(\chi_n = (3-\mu_n)/(1+\mu_n)$, $\beta_n^t = \alpha_n^t E_n/(1+\mu_n)$ for a plane stressed state; α^t, G, E (α_n^t, G, E_n) is the coefficient of linear thermal expansion, shear modulus, Young's modulus; $\mu(\mu_n)$ is Poisson's ratio material of the matrix (respectively, inclusion).

In the class of the functions $g_k(t_k) \in H\left(k = \overline{1,M}\right)$, $g_k'(t_k) \in H^*\left(k = \overline{M+1,N}\right)$, the system integral equation (11) has a unique solution for its arbitrary right-hand side under the conditions

$$\int_{Ln} g_n'(t_n)\mathrm{d}t_n = 0, n = \overline{M+1,N}. \quad (12)$$

Condition (12) ensures the uniqueness of displacements in traversing the contours of cracks.

We note that the choice of complex potentials in equation (10) ensures the identical satisfaction of the boundary condition (4) on the contours of inclusions based on such a choice of an analytic continuation from the matrix region into the inclusion region, in which the stresses are continuous, and the displacements have a gap (for the approach to the contours of inclusions left and right). It should also be noted that condition (3) provides the limitation on the infinity of the function $f(z)$ and the stress component.

The SIFs K_I and K_{II} at the crack tips are found according to formulas (Savruk,1981).

$$K_I^{\pm} - \mathrm{iK_{II}^{\pm}} = \mp\lim_{t_k \to l_k^{\pm}}\left[\sqrt{2\pi|t_k - l_k^{\pm}|}Q_k(t_k)\right], \quad (13)$$

$k = \overline{M+1,N}$,

where the lower signs correspond to the beginning of the crack (l_k^-) and the upper ones correspond to the end of the crack (l_k^+).

DOI 10.2478/ama-2019-0002

4. THE NUMERICAL ANALYSIS

Let in the band of periods of width d (along the axis Ox), there is an elliptic inclusion with semi axes a and b, bounded by closed contour L_1 and an unloaded thermally insulated rectilinear crack $L_2(p_2(t_2) = \tau_2(t_2) = \mu_2(t_2) = 0)$ with a length $2l$. We will assume that along the closed contour L_1, the conditions for an ideal mechanical contact $(g_1^*(t_1) = 0)$ are given,

The crack is located along the axis Ox $(z_2^0 = d_1, \alpha_2 = 0)$, and its center is at the point $(d_1, 0)$. At an infinitely distant point, a temperature field $T_\infty(x, y) = q(x\cos\gamma + y\sin\gamma) + T_0$ is given, where T_0 is the constant temperature and q is the homogeneous heat flux at an angle γ to the axis Ox (Fig. 2).

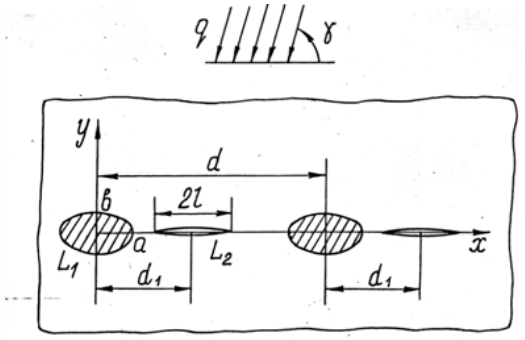

Fig. 2. A periodic system of elliptic inclusions and rectilinear cracks

The solution of the problem consists in solving the system of two integral equations (8) and (9) of the heat conduction problem with respect to functions $\mu(t_1)$, $\gamma'(t_2)$ and substituting them into the system of two equations (11) and (12) of the thermoelasticity problem for the determination of functions $Q_k(t_k), k = 1, 2$. Then we calculate the SIFs $K_I^{\pm}, K_{II}^{\pm}$, which are the real quantities that characterise the stress-deformed state in the vicinity of the crack tips, according to formula (13). The numerical solution of the system of equations (8), (9), (12) and (13) is found using the method of mechanical quadrature (Erdogan et. el.; 1973). The dimensionless SIFs $K_I^{\pm}/K_0$, $K_{II}^{\pm}/K_0$ where $K_0 = q\beta^t l\sqrt{\pi l}\,/\,(1+\chi)$ are obtained for different values of the thermal, mechanical and geometric parameters of the problem for $\chi = \chi_1 = 2$. In this case, if the heat flow g is directed perpendicularly to the line of cracks $(\gamma = \pi/2)$, then $K_I^{\pm} = 0$, $K_{II}^{\pm} \neq 0$; if parallelly $(\gamma = 0)$, then $K_I^{\pm} \neq 0$, $K_{II}^{\pm} = 0$.

The numerical values in the numerator corresponding to K_{II}^-/K_0 (left tip of the crack), and in the denominator corresponding to K_{II}^+/K_0 (right tip of the crack) are given in Table 1. The values of SIFs in the left tip of the crack are greater (or lesser) than those in the right tip of the crack when $\lambda_1/\lambda < 1$ (or $\lambda_1/\lambda > 1$) for different ratio α_1^t/α^t.

We plotted the dependences of dimensionless SIFs $\mathrm{K_I^{\pm}/K_0}$ on the half-length of the crack $\delta = \mathrm{l/a}$ for $\gamma = 0, \frac{\mathrm{d_1}}{\mathrm{a}} = 2$ and $\mathrm{d/a} = 6$ (Figs. 3 and 4). Curve 1 correspond to the value of $\Gamma_1 = 2$; curve 2 to that of $\Gamma_1 = 0.5$ for $\lambda_1/\lambda = 0.5$, $\alpha_1^t/\alpha^t = 4$; curves 3 to that of $\Gamma_1 = 2$; curves 4 to that of $\Gamma_1 = 0.5$ for $\lambda_1/\lambda = 4$, $\alpha_1^t/\alpha^t = 4$.

Tab. 1. The dimensionless numerical values $\mathrm{K_{II}^{\pm}/K_0}$ for $\gamma = \pi/2$, $\mathrm{b/a} = 0.5$, $\mathrm{l/a} = 0.8$, $\mathrm{d_1/a} = 2$ depending on the relative values $\Gamma_1 = \mathrm{G_1/G}$ and different values of the parameters λ_1/λ, α_1^t/α^t, d/a

$\Gamma_1 = \mathrm{G_1/G}$	$\lambda_1/\lambda = 0.5$ $\alpha_1/\alpha = 4$		$d/a = 6$	
	$d/a = 6$	$d/a = 12$	$\lambda_1/\lambda = 4$ $\alpha_1^t/\alpha^t = 4$	$\lambda_1/\lambda = 0.5$ $\alpha_1^t/\alpha^t = 0.5$
0.2	−1.740/0.916	−1.879/0.863	−0.812/0.907	−1.584/0.905
0.5	−1.754/1.006	−2.181/0.984	−0.710/0.969	−1.401/0.974
2	−2.216/1.175	−3.726/1.283	−0.583/1.086	−1.164/1.023
5	−2.921/1.348	−5.795/1.601	0.509/1.223	−1.078/0.971
20	−3.844/2.044	−9.556/2.388	0.145/1.903	−1.192/0.558

The solid lines correspond to the SIF K_I^+/K_0 at the right crack tip and the dashed lines correspond to the SIF K_I^-/K_0 at the left crack tip (closer to the inclusion). In this case, when the heat flux is directed in parallel $(\gamma = 0)$ to the cracks and large axes of the elliptic inclusions $(b < a)$, the values of the SIFs at both tips of the crack are larger for the harder ones than the matrix $(G_1 > G)$ inclusions compared with the case of less rigid $(G_1 < G)$ inclusions when $\alpha_1^t/\alpha^t > 1$ (Fig. 3). This means that the strength of the body increases with a decrease in the rigidity of inclusion in terms of fracture mechanics. If the large axes of the elliptic inclusions are perpendicular to the cracks and the heat flux $(b > a)$, then, on the contrary, the strength of the body decreases with a decrease in the stiffness of the inclusion (Fig. 4).

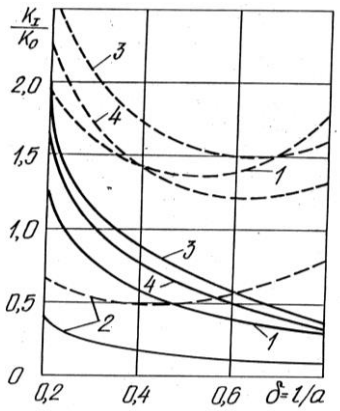

Fig. 3. Dependences of dimensionless SIFs $K_I^{\pm}/K_0$ on the half-length of the crack $\delta = l/a$ for $b/a = 0.5$

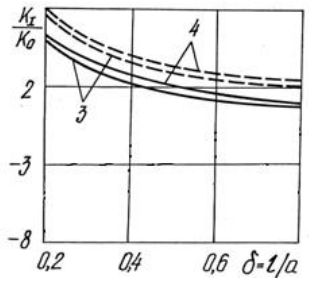

Fig. 4. Dependences of dimensionless SIFs $K_I^{\pm}/K_0$ on the half-length of the crack $\delta = l/a$ for $b/a = 2$

If the large axes of the inclusions are perpendicular to the direction of the heat flux and the cracks $(b > a)$, then the values of

the SIF K_I>0 when $\lambda_1/\lambda > 1$ (Fig. 4). If the large axes of inclusions are parallel ($b < a$) to the direction of the heat flow, then the K_I>0 for different values of the ratio λ_1/λ (Fig. 3).

It should also be noted that this does not take into account the possible contact of the shore of the crack. Therefore, in some cases, SIF $K_I < 0$. Such a result can be used to obtain a solution of the problem using the method of superposition for the action, in addition to the given temperature field, other temperature or force factors, which together do not cause the contact of the shores of the crack.

In the considered problem, do not cause the contact of the shores of the crack if the heat flux is parallel to the large axes of the elliptic inclusions ($b < a$) and the crack line and also when the flow is perpendicular ($b > a$) for $\lambda_1/\lambda > 1$. Then, according to the σ_θ-criterion (based on the hypothesis of the initial growth of the crack) from equations of the boundary equilibrium (Panasyuk et al., 1976), it is possible to find the critical values of the heat flux q_{cr} at which the growth of the crack begins and the local destruction of the body, according to the formula:

$$q_{\rm cr} = K_q \frac{K_{1C}}{\cos^3\frac{\theta_*}{2}\left(k_1^{\pm} - 3k_2^{\pm}\operatorname{tg}\frac{\theta_*}{2}\right)}, K_q = \frac{1+\chi}{\alpha^t \mathrm{El}\sqrt{\pi l}}, \qquad (14)$$

where K_{1C} is the constant of a material that characterises the resistance of the material to the destruction and is determined experimentally; $\theta_* = 2\operatorname{arctg}\frac{k_1^{\pm} - \sqrt{\left(k_1^{\pm}\right)^2 + 8\left(k_2^{\pm}\right)^2}}{4k_2^{\pm}}$ – angle of initial growth of the crack, $k_1^{\pm} = K_I^{\pm}/K_0$, $k_2^{\pm} = K_{II}^{\pm}/K_0$.

In the partial case, when the heat flux is directed parallelly to the cracks ($\gamma = 0$) for $\lambda_1/\lambda = 4$, $\alpha_1^t/\alpha^t = 4$, $\delta = l/a$= 0.6, with $b/a = 0.5$, obtained: if $\Gamma_1 = 2$, then $q_{\rm cr} = 0.86K_qK_{1C}$; if $\Gamma_1 = 0{,}5$, then $q_{\rm cr} = 1.04K_qK_{1C}$; when $b/a = 2$, received: if $\Gamma_1 = 2$, then $q_{\rm cr} = 0.54K_qK_{1C}$; if $\Gamma_1 = 0.5$, then $q_{\rm cr} = 0.44K_qK_{1C}$.

On the basis of the analysis of the obtained critical values of the heat flow, it follows that a more rigid than an elliptic inclusion matrix with a large axis parallel to the heat flux ($b < a$) determines a less critical value of the heat flux q_{cr} (at which the growth of the crack in the left tip begins) when compared with less tough inclusion. If the large axis of elliptic inclusions is perpendicular to the heat flux ($b > a$), then, on the contrary, it causes an increase. A similar situation is observed for the right tip of the crack.

5. CONCLUSIONS

Two-dimensional mathematical models of the problems of stationary heat conductivity and thermoelasticity for an infinite elastic plane with a periodic system of curvilinear inclusions and cracks in the form of system SIEs of the first kind on the contours of cracks and the second kind on the contours of inclusions are constructed. This approach allows to obtain a numerical solution of system SIE by applying the method of mechanical quadrature .

A numerical solution of system SIE in the partial case of a plane with a periodic system of elliptic inclusions and rectilinear thermally insulated cracks in the action of a given heat flux is obtained. On the basis of this solution, SIF at the crack tips are calculated, which in the future are used to determine the critical values of the heat flux for which the crack begins to grow.

REFERENCES

1. **Brock L.M**. (2016), Contours for planar cracks growing in three dimensions: Coupled thermoelastic solid (planar crack growth in 3D), *Journal of Thermal Stresses*, 39(3), 345–359.
2. **Cheesman B.A., Santare M.H.** (2000), The interaction of a curved crack with a circular elastic inclusion, *Int. J. Fract.,*103, 259-278.
3. **Chen H., Wang Q., Liu G. , Sun J**. (2016), Simulation of thermoelastic crack problems using singular edge-based smoothed finite element method, *Int. J. of Mech. Sci.,* 115,116, 23-134.
4. **Choi H.J.** (2014), Thermoelastic interaction of two offset interfacial cracks in bonded dissimilar half-planes with a functionally graded interlayer, *Acta Mechanica* , 225(7),2111–2131.
5. **Elfakhakhre N.R.F., Nik L., Eshkuvatov N.M.A.** (2017), Stress intensity factor for multiple cracks in half plane elasticity, *AIP Conference*, 1795(1).
6. **Erdogan F., Gupta B.D., Cook T.S.** (1973), The numerical solutions of singular integral equations, *Methods of analysis and solutions of crack problems. Leyden: Noordhoff Intern. publ*., 368-425.
7. **Havrysh V.I.** (2015), Nonlinear boundary-value problem of heat conduction for a layered plate with inclusion, *Phis.-chim. mechanica materialiv (Materials Science)*, 51(3), 331–339.
8. **Havrysh V.I**. (2017) Investigation of temperature fields in a heat-sensitive layer with through inclusion, *Phis.-chim.mechanica materialiv (Materials Science)*, 52(4), 514–521.
9. **Kit H.S., Chernyak M.S.** (2010), Stressed state of bodies with thermal cylindrical inclusions an cracks (plane deformation), *Phis.-chim. mechanica materialiv (Materials Science),* 46(3), 315–324.
10. **Kit, G.S. , Ivas'ko, N.M**. (2013), Plane deformation of a semi-infinite body with a heat-active crack perpendicular to its boundary, *Teoret. I prikl. Mehanika*, 53(7), 30–37.
11. **Matysiak S.J., Evtushenko A.A., Zelenjak V.M.** (1999), Frictional heating of a half–space with cracks. I. Single or periodic system of subsurface cracks, *Tribology Int*., 32, 237-243.
12. **Panasyuk V.V., Savruk M.P., Datsyshyn O.P.** (1976), *Distribution tense neighborhood of cracks in the plates and shells* (in Russian), Kiev, Naukova dumka
13. **Rashidova E.V., Sobol B.V**. (2017), An equilibrium internal transverse crack in a composite elastic half-plane*, Journal of Applied Mathmatics and Mechanics*, 81(3), 236–247
14. **Savruk M.P., Zelenyak V.M.** (1986), Singular integral equations of plane problems of thermal conductivity and thermoelasticity for a piecewise–uniform plane with cracks, *Phis.-chim. mechanica materialiv (Materials Science)*, 22(3), 297–307.
15. **Savruk M.P.** (1981), *Two-dimensional elasticity problem for bodies with cracks* (in Russian), Kiev, Naukova dumka.
16. **Sekine H**. (1975), Thermal stress singularities at tips of a crack in a semi-infinite medium under uniform heat flow , *Eng. Fract. Mech*. , 7 (4) , 713-729.
17. **Sushko O.P**. (2013), Thermoelastic state of a body with two coplanar thermally active circular cracks, *Journal of Mathematical Sciences*, 190(5), 725–739.
18. **Tweed I., Lowe S.** (1979), The thermoelastic problem for a half-plane with an internal line crack, *Int. J. Eng. Sci*., 17(4), 357-363.
19. **Xiao Z..M., Chen B.J.** (2001), Stress intensity factor for a Griffith crack interacting with a coated inclusion, *Int. J. Fract.,* 108*,* 193-205.
20. **Zelenyak B.M**. (2015), Thermoelastic equilibrium of a three-layer circular hollow cylinder weakened by a crack, *Phis.-chim. mechanica materialiv (Materials Science)*, 50(1), 14–19.
21. **Zelenyak V.M.** (2012), Thermoelastic interaction of a two–component circular inclusion with a crack in the plate, *Phis.-chim. mechanica materialiv (Materials Science)*, *Materials Science*, 48(3), 301–307.
22. **Zelenyak, V.M., Kolyasa, L.I.** (2016). Thermoelastic state of a half plane with curvilinear crack under the conditions of local heating, *Phis.-chim. mechanica materialiv (Materials Science)*, 52(3), 315-322.

DOI 10.2478/ama-2019-0003

POSITION/FORCE CONTROL OF MANIPULATOR IN CONTACT WITH FLEXIBLE ENVIRONMENT

Piotr GIERLAK*

*Faculty of Mechanical Engineering and Aeronautics, Department of Applied Mechanics and Robotics
Rzeszow University of Technology, al. Powstańców Warszawy 12, 35-959 Rzeszów, Poland

pgierlak@prz.edu.pl

received 26 June 2018, revised 3 March 2019, accepted 7 March 2019

Abstract: The paper presents the issue position/force control of a manipulator in contact with the flexible environment. It consists of the realisation of manipulator end-effector motion on the environment surface with the simultaneous appliance of desired pressure on the surface. The paper considers the case of a flexible environment when its deformation occurs under the pressure, which has a significant influence on the control purpose realisation. The article presents the model of the controlled system and the problem of tracking control with the use of neural networks. The control algorithm includes contact surface flexibility in order to improve control quality. The article presents the results of numerical simulations, which indicate the correctness of the applied control law.

Key words: Robotics, robot control, nonlinear control systems

1. INTRODUCTION

The number of industrial applications, in which robots come in contact with the environment and where it has a significant influence on the robotised processes realisation quality, is constantly increasing (Birglen and Schlicht, 2018; Denkena et al. 2017; Hashemiet et al., 2013; Iglesias et al., 2015; Lotz et al., 2014; Mendes and Neto, 2015). The aforementioned processes include, among others, robotised mechanical processing such as grinding (Zhu et al., 2015), polishing (Gracia et al., 2018; Tian et al., 2016), or edge deburring (Burghardt et al., 2017b). Therefore, modelling and control of robots in interaction with the environment becomes crucial, particularly if the actual features of the environment are taken into account, such as flexibility or damping. Manipulator-environment system modelling is a complex issue, and the weakest point of the model is partly connected with the environment and model of manipulator's contact with the surface. A significant difficulty in environment modelling is its changeability and the lack of certainty or knowledge of its parameters, resulting from the geometrical complexity of structures with which the manipulator interacts, related to changing stiffness, damping and mass balance in various parts of the structure. Moreover, environment surface shape may be not known in detail, which increases system description uncertainty (Burghardt et al., 2017a; Capisani and Ferrara, 2012; Duan et al., 2018; Jafari and Ryu, 2016; Pliego-Jiménez and Arteaga-Pérez, 2015; Ravandi et al., 2018).

The paper presents the issue of manipulator position/force control in contact with an environment, taking into consideration its crucial feature, which is flexibility. The issue of position/force control itself consists of the realisation of manipulator end-effector motion on the environment surface with the simultaneous appliance of desired pressure on the surface (Gierlak, 2014; Hendzel et al., 2014). End-effector motion speed and pressure force result from technological process parameters. In the case of a deformable environment, its deformation occurs under pressure, which has a significant influence on control purpose realisation Thus, in order to improve control quality, control algorithm takes into consideration the contact surface flexibility. The paper used artificial neural networks (Gierlak, 2012; Żylski and Gierlak, 2010) to realise control compensating system non-linearity, thanks to which, it is not necessary to know the structure and the parameters of the manipulator and environment models.

2. SYSTEM DYNAMICS

Manipulator dynamics expressed via configuration coordinates have the following formula:

$$M(q)\ddot{q} + C(q,\dot{q})\dot{q} + F(\dot{q}) + G(q) + \xi(t) = u + J(q)^T\lambda\,, \tag{1}$$

where: $q \in R^n$ – the vector of generalised coordinates, $M(q) \in R^{n\times n}$ – the inertia matrix, $C(q,\dot{q})\dot{q} \in R^{n\times n}$ – the vector of centrifugal and Coriolis forces, $F(\dot{q}) \in R^n$ – the friction vector, $G(q) \in R^n$ – the gravity vector, $\xi(t) \in R^n$ – the vector of disturbances bounded by $\|\xi\| \le b$, $b > 0$, $u \in R^n$ – the control input vector, $J(q) \in R^{m\times n}$ – an analytical Jacobian matrix, $\lambda \in R^m$ – an interaction force vector expressed in the task space, n – the number of degrees of freedom of the manipulator, m – a workspace (task space) dimension.

Due to the control purpose, which is the manipulator end-effector motion on the environment surface with simultaneously influencing it with normal force, it is convenient to present manipulator dynamics in a task coordinate system related to the environmental surface. Cartesian coordinates c were selected as task coordinates, which are related to the configuration coordinates in the following way:

$$c = k(q) \in R^m , \tag{2}$$

where: $k(q)$ is the so-called kinematics function. Jacobian $J(q)$ describing the transformation of forces and speeds between the task space and the configuration spaces results from the formula:

$$J(q) = \frac{\partial c}{\partial q} = \frac{\partial k(q)}{\partial q} . \tag{3}$$

On the basis of equations (1) and (2), manipulator dynamics were described in task coordinates (Gierlak, 2018; Gierlak and Szuster, 2017)

$$A(q)\ddot{c} + H(q,\dot{q})\dot{c} + B(q,\dot{q}) + G(q,\dot{q}) + \Psi(q,t) = U + \lambda . \tag{4}$$

where specific vectors and matrices are as follows:

$$\left.\begin{array}{c} J^{-T}M(q)J^{-1} = A(q) \in R^{m\times m} \\ J^{-T}C(q,\dot{q})J^{-1} - J^{-T}M(q)J^{-1}\dot{J}J^{-1} = H(q,\dot{q}) \in R^{m\times m} \\ J^{-T}\big(F(\dot{q}) + G(q)\big) = B(q,\dot{q}) \in R^m \\ J^{-T}\xi(t) = \Psi(q,t) \in R^m \\ J^{-T}u = U \in R^m \end{array}\right\} \tag{5}$$

and the expression $J^{-T} = (J^{-1})^T = (J^T)^{-1}$. In the case of $m \neq n$, the Moore-Penrose pseudo-inverse J^+ instead of J^{-1} should be used (Barata and Hussein, 2012). Task space $\{C\}$ was divided into r-dimensional normal subspace $\{N\}$ and $(m-r)$-dimensional tangent subspace $\{T\}$: $\{C\} = \{T\} \oplus \{N\}$ (Vukobratovič et al., 2002). It leads to the decomposition of vector c into a part related to the tangent directions $c_\tau \in R^{m-r}$ and a part related to normal directions $c_n \in R^r$ so $c = [c_\tau^T \quad c_n^T]^T$. Thus, it is now convenient to determine the environment features that are different on tangent and normal directions. For normal directions, the most important feature is flexibility, which is presented by the formula:

$$K_e c_n = F_{en}, \tag{6}$$

where: $F_{en} \in R^r$ – a normal force vector, $K_e \in R^{r\times r}$ – diagonal matrix of environment stiffness, so $K_e = K_e^T > 0$. On tangent directions, manipulator end-effector motion is hindered by resisting force $F_{e\tau}$, which may be modelled or compensated for on the basis of force detector measurements. Such an approach of interaction between the manipulator and the environment allows expressing interaction forces vector as $\lambda = [F_{e\tau}^T \quad F_{en}^T]^T$.

Equation (6) was transformed into a form $c_n = P_e F_{en}$, in which $P_e = K_e^{-1} \in R^{r\times r}$ is flexibility matrix; so, $P_e = P_e^T > 0$. By adding decomposed vector c (taking into consideration $c_n = P_e F_{en}$) to equation (4), the dynamic equation of the system motion equation takes on the following form:

$$A(q)E\ddot{\theta} + H(q,\dot{q})E\dot{\theta} + B(q,\dot{q}) + \Psi(q,t) = U + \lambda, \tag{7}$$

where vector describing system state $\theta = [c_\tau^T \quad F_{en}^T]^T \in R^m$ consists of position and force variables, while matrix E has the following form:

$$E = \begin{bmatrix} I_{(m-r)\times(m-r)} & 0 \\ 0 & P_e \end{bmatrix} \in R^{m\times m}, \tag{8}$$

and presents information on environment flexibility. Description (7) with vector θ is a more natural description of dynamics due to control purposes than equation (4), since the purpose of control of the presented system is to realise motion on tangent directions and to realise forces on normal directions.

3. TRACKING CONTROL

The purpose of control is to implement the desired trajectory $\theta_d(t) \in R^m$, $\dot{\theta}_d(t)$, $\ddot{\theta}_d(t)$, which consists of the trajectory of motion in the tangent plane $c_{\tau d}(t) \in R^{m-r}$, $\dot{c}_{\tau d}(t)$, $\ddot{c}_{\tau d}(t)$ and the trajectory of force on normal directions $F_{end}(t) \in R^r$, $\dot{F}_{end}(t)$, $\ddot{F}_{end}(t)$. So, it can be noted in the following way:

$$\theta_d = \begin{bmatrix} c_{\tau d} \\ F_{end} \end{bmatrix}, \dot{\theta}_d = \begin{bmatrix} \dot{c}_{\tau d} \\ \dot{F}_{end} \end{bmatrix}, \ddot{\theta}_d = \begin{bmatrix} \ddot{c}_{\tau d} \\ \ddot{F}_{end} \end{bmatrix}. \tag{9}$$

Tracking control was defined as an issue of stabilising tracking error, defined as:

$$\tilde{\theta} = \theta_d - \theta, \tag{10}$$

that is, regarding both motion error and force error stabilisation. In accordance with the classic theory of tracking control of nonlinear systems, a filtered tracking error was defined:

$$s = \dot{\tilde{\theta}} + \Lambda\tilde{\theta}, \tag{11}$$

which is a linear combination of tracking error and its derivative. In equation (11), project matrix $\Lambda \in R^m$ occurs, which fulfils the condition $\Lambda = \Lambda^T > 0$. By adding equation (11) to formula (7), the description of the dynamics in the filtered tracking error function:

$$A(q)E\dot{s} = -H(q,\dot{q})Es + A(q)E\dot{v} + H(q,\dot{q})Ev + B(q,\dot{q}) + \Psi(q,t) - U - \lambda, \tag{12}$$

where ancillary variable $v = \dot{\theta}_d + \Lambda\tilde{\theta}$ occurs. Nonlinear part of equation (12) was marked as:

$$A(q)E\dot{v} + H(q,\dot{q})Ev + B(q,\dot{q}) = f, \tag{13}$$

where $f \in R^m$ is a function that depends both on the manipulator model and the environment. It particularly depends on the unknown manipulator parameters and unknown environment stiffness. Thus, the final form of the dynamic system motion description is:

$$A(q)E\dot{s} = -H(q,\dot{q})Es + f + \Psi(q,t) - U - \lambda. \tag{14}$$

For this system, the control consists of conventional PD regulator, control compensating for system nonlinearity $\hat{f} \in R^m$, and control compensating for the interaction forces influence λ:

$$U = K_D s + \hat{f} - \lambda - r. \tag{15}$$

In the established control, function $\hat{f}$ approximates f, and expression $K_D s$ is a form of PD control where $K_D \in R^{m\times m}$ is an amplification matric that $K_D = K_D^T > 0$, while $r \in R^m$ is a robust control. A part of equation (15) expresses forces of interaction between the manipulator and the environment in all directions. It is assumed that its value is assessable via measurement and can be put in the control signal. Assessable via measurement are also vectors of angular displacements q and angular speeds $\dot{q}$, which, knowing kinematic equations (2), allow calculating motion parameters in task coordinates c. It is necessary to establish filtered tracking error s and ancillary signal v occurring in function $\hat{f}$. In order to implement compensation of nonlinear function f, it was decomposed into two parts: one $f_\tau \in R^{(m-r)}$ for tangent directions, and the other $f_n \in R^r$ for normal directions. Neural network linear in regards to RVFL weights were used to approximate the member functions. This type of neural network is a universal approximator (Galushkin, 2007; Pao et al., 1994), which, due to relatively simple structure, is frequently used in robot control systems for nonlinearity compensation (Kumar et al., 2011). If the selected network is a network with a set layer of input weights,

DOI 10.2478/ama-2019-0003

one hidden layer, and input weights layer undergoing adaptation, then nonlinear member functions may be noted as outputs from the ideal neural networks with limited approximation errors:

$$f = \begin{bmatrix} f_\tau \\ f_n \end{bmatrix} = \begin{bmatrix} W_\tau^T \Phi_\tau(x_\tau) + \varepsilon_\tau(x_\tau) \\ W_{n1}^T \Phi_{n1}(x_{n1}) + \varepsilon_{n1}(x_{n1}) \\ \vdots \\ W_{ni}^T \Phi_{ni}(x_{ni}) + \varepsilon_{ni}(x_{ni}) \\ \vdots \\ W_{nr}^T \Phi_{nr}(x_{nr}) + \varepsilon_{nr}(x_{nr}) \end{bmatrix}, \tag{16}$$

where: x_τ, x_{ni} – network input signals vectors, W_τ, W_{ni} – ideal output weights matrices, $\Phi_\tau(.)$,$\Phi_{ni}(.)$ are neurons activation functions vectors, and ε_τ, ε_{ni} are vectors of errors of function mapping by networks that $\|\varepsilon_\tau\| \leq \varepsilon_{b\tau}$, $\|\varepsilon_{ni}\| \leq \varepsilon_{bni}$, where $\varepsilon_{b\tau} > 0$, $\varepsilon_{bni} > 0$. If neurons activation functions are selected in the form of a basic functions' group, then the network with ideal limited weights has the feature of approximation of any function defined on a compact set with a finite number of discontinuity points (Hertz et al., 1991). Since network ideal weights are unknown, function estimate (16) should be used, in form of:

$$\hat{f} = \begin{bmatrix} \hat{f}_\tau \\ \hat{f}_n \end{bmatrix} = \begin{bmatrix} \widehat{W}_\tau^T \Phi_\tau(x_\tau) \\ \widehat{W}_{n1}^T \Phi_{n1}(x_{n1}) \\ \vdots \\ \widehat{W}_{ni}^T \Phi_{ni}(x_{ni}) \\ \vdots \\ \widehat{W}_{nr}^T \Phi_{nr}(x_{nr}) \end{bmatrix}, \tag{17}$$

where $\widehat{W}_\tau$, $\widehat{W}_{ni}$ are network ideal weights estimates. As equation (16) suggests, each nonlinear function f_n was decomposed into functions f_{ni}, each of which corresponds to the normal i-th direction and is approximated by a separate neural network. This action was performed due to the possibility of proving closed system stability for network weights' estimation rule not requiring knowledge of environment elasticity.

Taking into account control rule (15), as well as equations (16) and (17) in the dynamics equation (14), the following closed system description was received:

$$A(q)Es\dot{s} = -H(q,\dot{q})Es + \Psi(q,t) - K_D s + r + \begin{bmatrix} \widetilde{W}_\tau^T \Phi_\tau(x_\tau) \\ \widetilde{W}_{n1}^T \Phi_{n1}(x_{n1}) \\ \vdots \\ \widetilde{W}_{ni}^T \Phi_{ni}(x_{ni}) \\ \vdots \\ \widetilde{W}_{nr}^T \Phi_{nr}(x_{nr}) \end{bmatrix} + \begin{bmatrix} \varepsilon_\tau(x_\tau) \\ \varepsilon_{n1}(x_{n1}) \\ \vdots \\ \varepsilon_{ni}(x_{ni}) \\ \vdots \\ \varepsilon_{nr}(x_{nr}) \end{bmatrix}, \tag{18}$$

in which the interaction forces' influence was compensated for by the control, so that vector λ no longer occurs in equation (18). Closed-loop system dynamics is activated by the assessment errors of network and weights, which are as follows:

$$\widetilde{W}_\tau = W_\tau - \widehat{W}_\tau, \widetilde{W}_{ni} = W_{ni} - \widehat{W}_{ni}. \tag{19}$$

The errors are decreased as a result of the weights estimates adaptation, which occurs continuously during system operation. Weights adaptation rules were accepted in the following form (Lewis et al., 1995; Narendra and Annaswamy, 1987; Polycarpou and Ioannu, 1991):

$$\left.\begin{aligned} \dot{\widehat{W}}_\tau &= \Gamma_\tau \Phi_\tau(x_\tau) s_\tau^T - k_\tau \|s_\tau\| \Gamma_\tau \widehat{W}_\tau \\ \dot{\widehat{W}}_{ni} &= \Gamma_{ni} \Phi_{ni}(x_{ni}) s_{ni} - k_{ni} |s_{ni}| \Gamma_{ni} \widehat{W}_{ni} \end{aligned}\right\}, \tag{20}$$

where: $\Gamma_\tau = \Gamma_\tau^T > 0$, $\Gamma_{ni} = \Gamma_{ni}^T > 0$ – adaptation amplification matrices, $k_\tau > 0$, $k_{ni} > 0$ – constant project parameters, s_τ, s_{ni} – results from the decomposition of filtered tracking error $s = [s_\tau^T \quad s_n^T]^T$, where $s_n = [s_{n1} \quad \cdots \quad s_{ni} \quad \cdots \quad s_{nr}]^T$. The second element on the right of formula (20) is responsible for 'attenuation' of weights estimates adaptation, while the 'attenuation' size is decided by the coefficients k_τ and k_{ni}. Assuming such rules of weights estimates actualisation guarantees their limitedness and protects the system from estimates 'drifting' and 'exploding', even without uniform system activation. When decomposing interruptions vector and robust control in the following way:
$\Psi(q,t) = [\Psi_\tau^T(q,t), \Psi_{n1}(q,t), \dots, \Psi_{ni}(q,t), \dots, \Psi_{nr}(q,t)]^T$ and $r = [r_\tau^T, r_{n1}, \dots, r_{ni}, \dots, r_{nr}]^T$, specific expressions of robust control were assumed as:

$$r_\tau = -\frac{K_\tau}{\|s_\tau\|} s_\tau \,, r_{ni} = -\frac{K_{ni}}{|s_{ni}|} s_{ni}, \tag{21}$$

where: $K_\tau > b_\tau \geq \|\Psi_\tau(q,t)\|$, $K_{ni} > b_{ni} \geq |\Psi_{ni}(q,t)|$.

Assumed neural networks control and weights adaptation rules guarantee the practical stability of the control system (Canudas et al., 1996). The proof of the stability is complex and was presented for a similar case by Gierlak and Szuster (2017) with regard to conditions given by Lewis et al. (1995), Narendra and Annaswamy (1987) and Polycarpou and Ioannu (1991).

4. NUMERICAL EXAMPLE

A two-link planar manipulator in contact with a flat surface was selected as an example presenting the work of control system of the manipulator in contact with a flexible environment (Fig. 1).

Two-link manipulator dynamics in articulated coordinates is described with an equation in the following form (1) of the following vectors and matrices (Gierlak and Szuster, 2017):

$$\left.\begin{aligned} \boldsymbol{M}(\boldsymbol{q}) &= \begin{bmatrix} a_1 & a_2\cos(q_2 - q_1) \\ a_2\cos(q_2 - q_1) & a_3 \end{bmatrix} \\ \boldsymbol{C}(\boldsymbol{q},\dot{\boldsymbol{q}}) &= \begin{bmatrix} 0 & -a_2\sin(q_2 - q_1)\dot{q}_2 \\ a_2\sin(q_2 - q_1)\dot{q}_1 & 0 \end{bmatrix} \\ \boldsymbol{F}(\dot{\boldsymbol{q}}) &= \begin{bmatrix} a_4\dot{q}_1 + a_6\mathrm{sgn}(\dot{q}_1) \\ a_5\dot{q}_2 + a_7\mathrm{sgn}(\dot{q}_2) \end{bmatrix} \\ \boldsymbol{G}(\boldsymbol{q}) &= \begin{bmatrix} a_8\cos(q_1) \\ a_9\cos(q_2) \end{bmatrix} \\ \boldsymbol{\xi}(t) &= \begin{bmatrix} \xi_1(t) \\ \xi_2(t) \end{bmatrix} \\ \boldsymbol{u} &= \begin{bmatrix} u_1 \\ u_2 \end{bmatrix} \\ \boldsymbol{q} &= \begin{bmatrix} q_1 \\ q_2 \end{bmatrix} \end{aligned}\right\} \tag{22}$$

Parameters characterising manipulator dynamics have the following significance:

$$\left.\begin{aligned} a_1 &= l_{c1}^2 m_1 + l_1^2 m_2 + I_1, \\ a_2 &= l_1 l_{c2} m_2, a_3 = l_{c2}^2 m_2 + I_2, \\ a_4 &= c_{v1}, a_5 = c_{v2}, a_6 = \kappa_1, a_7 = \kappa_2, \\ a_8 &= (l_{c1} m_1 + l_1 m_2) g, a_9 = l_{c2} m_2 g \end{aligned}\right\}. \tag{23}$$

where: m_i – a mass of i-th link, l_i – a length of i-th link, l_{ci} – the distance between centre of mass of i-th link and end of $i-1$ link, I_i – a mass moment of inertia of i-th link relative to its centre of mass, c_{vi} – coefficient of viscous friction in i-th kinematic pair, κ_i – moment of force of dry friction in i-th kinematic pair.

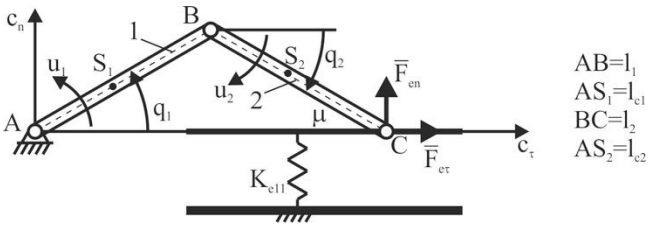

Fig. 1. The scheme of the 2-degrees-of-freedom manipulator with environment

Kinematic equation (2) describing manipulator end point position in the analysed case assume the following form:

$$\boldsymbol{c} = \begin{bmatrix} c_\tau \\ c_n \end{bmatrix} = \begin{bmatrix} l_1\cos(q_1) + l_2\cos(q_2) \\ l_1\sin(q_1) + l_2\sin(q_2) \end{bmatrix} \tag{24}$$

Knowledge of kinematics equations allows determining Jacobian $J(q)$ and recording system dynamics in the task coordinates. On the basis of the definition (3), Jacobian $J(q)$ was determined as:

$$J(q) = \begin{bmatrix} -l_1\sin(q_1) & -l_2\sin(q_2) \\ l_1\cos(q_1) & l_2\cos(q_2) \end{bmatrix}. \tag{25}$$

This enabled the presentation of robot dynamics in the form of equation (4), in which matrices and vectors have the following form:

$$A(q) = \frac{1}{\sin^2(q_2-q_1)}\begin{bmatrix} A_{11} & A_{12} \\ A_{21} & A_{22} \end{bmatrix}, \tag{26}$$

$$\left.\begin{aligned} A_{11} &= \frac{\cos^2(q_2)}{l_1^2}a_1 - \frac{2\cos(q_1)\cos(q_2)\cos(q_2-q_1)}{l_1 l_2}a_2 + \frac{\cos^2(q_1)}{l_2^2}a_3 \\ A_{12} &= A_{21} = \\ &\frac{\sin(q_2)\cos(q_2)}{l_1^2}a_1 - \frac{2\sin(q_1+q_2)\cos(q_2-q_1)}{l_1 l_2}a_2 + \frac{\sin(q_1)\cos(q_1)}{l_2^2}a_3 \\ A_{22} &= \frac{\sin^2(q_2)}{l_1^2}a_1 - \frac{2\sin(q_1)\sin(q_2)\cos(q_2-q_1)}{l_1 l_2}a_2 + \frac{\sin^2(q_1)}{l_2^2}a_3 \end{aligned}\right\} \tag{27}$$

$$H(q,\dot{q}) = \frac{1}{\sin^3(q_2-q_1)}\begin{bmatrix} H_{11} & H_{12} \\ H_{21} & H_{22} \end{bmatrix}, \tag{28}$$

$$\left.\begin{aligned} H_{11} &= \frac{g_1\cos(q_2)}{l_1^2}a_1 + \frac{g_5\cos(q_1)-g_6\cos(q_2)}{l_1 l_2}a_2 + \frac{g_2\cos(q_1)}{l_2^2}a_3 \\ H_{12} &= \frac{g_3\cos(q_2)}{l_1^2}a_1 + \frac{g_5\sin(q_1)-g_6\sin(q_2)}{l_1 l_2}a_2 + \frac{g_4\cos(q_1)}{l_2^2}a_3 \\ H_{21} &= \frac{g_1\sin(q_2)}{l_1^2}a_1 + \frac{g_7\cos(q_1)-g_8\cos(q_2)}{l_1 l_2}a_2 + \frac{g_2\sin(q_1)}{l_2^2}a_3 \\ H_{22} &= \frac{g_3\sin(q_2)}{l_1^2}a_1 + \frac{g_7\sin(q_1)-g_8\sin(q_2)}{l_1 l_2}a_2 + \frac{g_4\sin(q_1)}{l_2^2}a_3 \end{aligned}\right\} \tag{29}$$

$$\left.\begin{aligned} g_1 &= \cos(q_2)\cos(q_2-q_1)\dot{q}_1 - \cos(q_1)\dot{q}_2 \\ g_2 &= \cos(q_2)\dot{q}_1 - \cos(q_1)\cos(q_2-q_1)\dot{q}_2 \\ g_3 &= \sin(q_2)\cos(q_2-q_1)\dot{q}_1 - \sin(q_1)\dot{q}_2 \\ g_4 &= \sin(q_2)\dot{q}_1 - \sin(q_1)\cos(q_2-q_1)\dot{q}_2 \\ g_5 &= [\cos(q_2) + \cos(q_1)\cos(q_2-q_1)]\dot{q}_2 \\ g_6 &= [\cos(q_1) + \cos(q_2)\cos(q_2-q_1)]\dot{q}_1 \\ g_7 &= [\sin(q_2) + \sin(q_1)\cos(q_2-q_1)]\dot{q}_2 \\ g_8 &= [\sin(q_1) + \sin(q_2)\cos(q_2-q_1)]\dot{q}_1 \end{aligned}\right\}, \tag{30}$$

$$B(q,\dot{q}) = \begin{bmatrix} \frac{l_2\cos(q_2)[a_4\dot{q}_1 + a_6\cos(q_1)] - l_1\cos(q_1)[a_5\dot{q}_2 + a_7\cos(q_2)]}{l_1 l_2\sin(q_2-q_1)} \\ \frac{l_2\sin(q_2)[a_4\dot{q}_1 + a_6\cos(q_1)] - l_1\sin(q_1)[a_5\dot{q}_2 + a_7\cos(q_2)]}{l_1 l_2\sin(q_2-q_1)} \end{bmatrix} \tag{31}$$

$$U = \begin{bmatrix} \frac{l_2\cos(q_2)u_1 - l_1\cos(q_1)u_2(t)}{l_1 l_2\sin(q_2-q_1)} \\ \frac{l_2\sin(q_2)u_1(t) - l_1\sin(q_1)u_2(t)}{l_1 l_2\sin(q_2-q_1)} \end{bmatrix}, \tag{32}$$

$$\Psi(q,t) = \begin{bmatrix} \frac{l_2\cos(q_2)\xi_1(t) - l_1\cos(q_1)\xi_2(t)}{l_1 l_2\sin(q_2-q_1)} \\ \frac{l_2\sin(q_2)\xi_1(t) - l_1\sin(q_1)\xi_2(t)}{l_1 l_2\sin(q_2-q_1)} \end{bmatrix}. \tag{33}$$

In the analysed case, constant disturbance values were assumed as $\xi_1(t) = \xi_2(t) = \xi = const$. Forces of interaction between the manipulator and the environment are assumed as:

$$\lambda = \begin{bmatrix} F_{e\tau} \\ F_{en} \end{bmatrix} = \begin{bmatrix} \mu F_{en}\mathrm{sgn}(\dot{c}_\tau) \\ K_e c_n \end{bmatrix}. \tag{34}$$

In the analysed example, the contact surface is one-dimensional, thus, there is only one tangent direction, along which the end-effector motion can occur. The flexibility of the surface also occurs only in one normal direction. Therefore, the matrix E has a form:

$$E = \begin{bmatrix} 1 & 0 \\ 0 & P_e \end{bmatrix}, \tag{35}$$

where $P_e = K_e^{-1}$.

The control law equation (15) contains the interaction forces vector λ defined by the formula (34) and the gain matrix in the form:

$$K_D = \begin{bmatrix} K_{D\tau} & 0 \\ 0 & K_{Dn} \end{bmatrix}. \tag{36}$$

The filtered tracking error s taking into account the diagonal matrix $\Lambda = diag\{\Lambda_\tau \quad \Lambda_n\}$, has the form:

$$s = \begin{bmatrix} s_\tau \\ s_n \end{bmatrix} = \begin{bmatrix} \dot{\tilde{c}}_\tau + \Lambda_\tau\tilde{c}_\tau \\ \dot{\tilde{F}}_{en} + \Lambda_n\tilde{F}_{en} \end{bmatrix}, \tag{37}$$

where $\tilde{c}_\tau$ – the position error in the tangent direction, $\tilde{F}_{en}$ – the force error in the normal direction. The components of the robust control vector determined by equation (21) have the form:

$$r_\tau = -\frac{K_\tau}{|s_\tau|}s_\tau,\ r_n = -\frac{K_n}{|s_n|}s_n. \tag{38}$$

The most complex element of the control law (15) is the compensative control $\hat{f}$, the structure for which results from the applied neural network. Separate neural networks were used for the compensative control in the tangent and normal directions. The structure of the neural network that generates the output $\hat{f}_\tau$ is shown in Fig. 2.

The input-output dependency of the presented neural network has the form:

$$\hat{f}_\tau = \widehat{W}_\tau^T\Phi_\tau(x_\tau) = \widehat{W}_\tau^T S_\tau(V_\tau^T x_\tau) \tag{39}$$

where: $\Phi_\tau(x_\tau) = S_\tau(V_\tau^T x_\tau)$ – the output vector from the hidden layer, $S_\tau = [S_{\tau 1}, S_{\tau 2}, \dots, S_{\tau N}]^T$ – the vector of neuron activation function, $x_\tau = [x_{\tau 1}, x_{\tau 2}, \dots, x_{\tau M}]^T$ – the input vector, V_τ^T – the input weights matrix, in which the values of weights of connection of inputs with the hidden layer were grouped, $\widehat{W}_\tau^T$ – estimation of the output weight matrix, which contains the values of the weights of connections of the hidden layer with the network output $\hat{f}_\tau$. Elements of this matrix are adapted during the system operation. An analogous structure of the neural network was used to generate the compensative control $\hat{f}_n$ – in the description of this net-

DOI 10.2478/ama-2019-0003

work, the denotation n should be used instead of τ. The input vectors for both neural networks have the same form, because the nonlinearities in the tangent and normal directions depend on the same signals, thus: $x_\tau = x_n = [q_1, q_2, \dot{q}_1, \dot{q}_2, v_\tau, v_n, \dot{v}_\tau, \dot{v}_n]^T$, where v_τ and v_n are elements of the auxiliary signal $v = [v_\tau, v_n]^T$, which was introduced in equations (12) and (13). The neuron activation functions were selected as sigmoidal bipolar functions described by the equation:

$$S_{\tau i} = \frac{2}{1+\exp(-\beta z)} - 1, \tag{40}$$

where: $\beta > 0$ – the steepness factor of the function, z – the input value to the neuron.

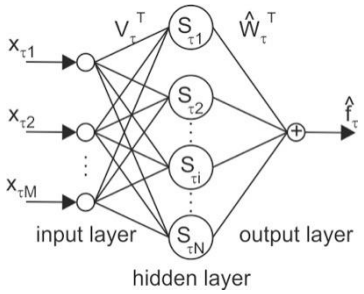

Fig. 2. Structure of neural network

The applied control law (15) leads to the description of a closed system (with feedback) in form (18), which, in the analysed example, takes the form:

$$A(q)E\dot{s} = -H(q,\dot{q})Es + \Psi(q,t) - K_D s + r + \\ + \begin{bmatrix} \widetilde{W}_\tau^T \Phi_\tau(x_\tau) \\ \widetilde{W}_n^T \Phi_n(x_n) \end{bmatrix} + \begin{bmatrix} \varepsilon_\tau(x_\tau) \\ \varepsilon_n(x_n) \end{bmatrix}. \tag{41}$$

The last two terms on the right side of the equation (41) require explanation. The terms $\widetilde{W}_\tau^T \Phi_\tau(x_\tau)$ and $\widetilde{W}_n^T \Phi_n(x_n)$ result from the inaccurate approximation of system nonlinearity by neural networks, which results from errors in the adaptation of the network weights $\widetilde{W}_\tau$ and $\widetilde{W}_n$. These adaptation errors are not known explicitly, because the ideal weights of neural networks are unknown. The last part results from the inaccuracy of approximation of nonlinear functions even by ideal neural networks that have finite mapping accuracy. This term is also not known in the open form. The last two expressions together with $\Psi(q,t)$ are understood as disturbances of the closed system and they constitute an excitation of error s.

The desired trajectory of motion was adopted in accordance with the following equation:

$$c_{\tau d} = c_{\tau d}(0) + \frac{v_{max}}{w_\tau} \sum_{i=1}^{3} ln \frac{\left(\frac{1}{e^{-w_\tau(t-t_{c1i})}+1}\right)\left(\frac{1}{e^{-w_\tau(t-t_{c4i})}+1}\right)}{\left(\frac{1}{e^{-w_\tau(t-t_{c2i})}+1}\right)\left(\frac{1}{e^{-w_\tau(t-t_{c3i})}+1}\right)} \tag{42}$$

where: $c_{\tau d}(0)$ – the initial position of the end-effector, v_{max} – the maximum velocity, w_τ – the coefficient corresponding to the velocity increase and decrease rate, $t \in (0{,}50)$ s. Function (42) and its first and second derivative in relation to time are limited.

The trajectory of system in the normal direction is the pressure force on the surface of contact, which should be continuous, limited and not negative, and should continuously have the first and second derivative in relation to time. Such conditions are met by the function:

$$F_{end} = F_{enmax} \sum_{i=1}^{3} \left[\frac{1}{1+e^{-w_n(t-t_{F1i})}} - \frac{1}{1+e^{-w_n(t-t_{F2i})}}\right] \tag{43}$$

where: F_{enmax} – the maximum pressure force, w_n – the coefficient corresponding to the force increase and decrease rate, $t \in (0{,}50)$ s.

Parameters of the robot-environment dynamic system, parameters of the control system and the desired trajectory are summarized in Tables 1–3.

In the analysed example, the contact surface is one-dimensional; thus, there is only one tangent direction, along which the end-effector motion can occur. Figure 3 presents the desired motion path, displacement on the tangent direction, and pressure force in the normal direction.

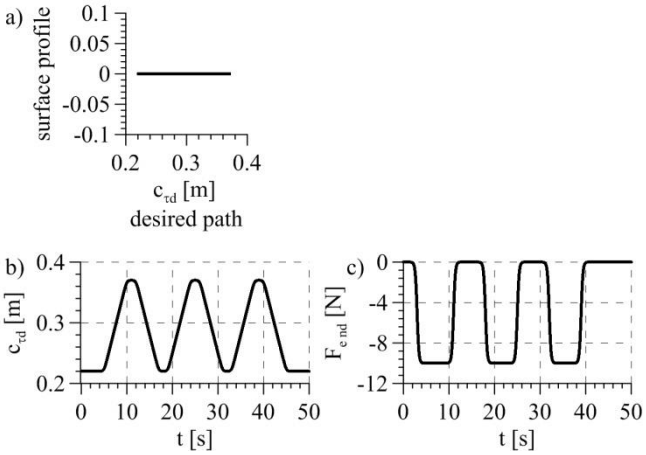

Fig. 3. Manipulator control purposes: a) motion path, b) desired displacement on the tangent direction, c) desired pressure force

Tab. 1. Parameters of robot-environment system used in numerical tests

Parameter	Unit	Value
a_1	kgm^2	0.036
a_2	kgm^2	$6 \cdot 10^{-5}$
a_3	kgm^2	0.031
a_4	Nms	0.54
a_5	Nms	0.51
a_6	Nm	0.02
a_7	Nm	0.02
a_8	Nm	0.05
a_9	Nm	0.025
l_1	m	0.22
l_2	m	0.22
K_e	N/m	1333
μ	-	0.04
ξ	Nm	0.01

The desired trajectory is planned so that during a move to the right, the manipulator end-effector exalts correct pressure, while during an end-effector return, there should be no pressure. Thus, there might be motion stages discerned: with pressure and without pressure. Fig. 4 presents the control signals generated by the specific control subsystems. The total control signal in the task space presents Fig. 4a. In accordance to equation (15), it consists of PD control (Fig. 4b), compensative control (Fig. 4c), robust control (Fig. 4d), as well as control of normal force λ_1 and control compensating for friction influence λ_2 (Fig. 4e).

Tab. 2. Parameters of control system used in numerical tests

Parameter	Unit	Value
Λ_τ	s^{-1}	3
Λ_n	s^{-1}	34.6
$K_{D\tau}$	kg/s	8
K_{Dn}	s	0.00173
k_τ	-	0.2
k_n	-	0.2
K_τ	N	0.001
K_n	N	0.01
number of neurons	-	15
Γ_τ	-	$4 \cdot I_{15x15}$
Γ_n	-	$0.0008 \cdot I_{15x15}$
$\widehat{W}_\tau(0)$	-	0
$\widehat{W}_n(0)$	-	0
$\hat{V}_\tau(0)$	-	$\mathrm{rand}\{\pm 0.5\}$
$\hat{V}_n(0)$	-	$\mathrm{rand}\{\pm 0.5\}$
β	-	2
v_{max}	m/s	0.03
w_τ	s^{-1}	5
F_{enmax}	N	-10
w_n	s^{-1}	5
$c_{\tau d}(0)$	m	0.22

Tab. 3. Parameters of desired trajectory used in numerical tests

Parameter	Unit	Value
t_{F11}	s	3
t_{F21}	s	16
t_{F12}	s	3
t_{F22}	s	28
t_{F13}	s	3
t_{F23}	s	3
t_{c11}	s	5
t_{c21}	s	10
t_{c31}	s	12
t_{c41}	s	17
t_{c12}	s	19
t_{c22}	s	24
t_{c32}	s	26
t_{c42}	s	31
t_{c13}	s	33
t_{c23}	s	38
t_{c33}	s	40
t_{c43}	s	45

PD control and compensative control pattern is typical for adapting systems, that is, PD control plays the largest role during the initial motion stage, when neural network weights estimates are unavailable and the compensative control is incorrect. Along with neural network weights estimates adaptation, the role of compensative control increases, while the role of PD control decreases. Force control is realised on the basis of the feedback loop and does not undergo adaptation. Fig. 4f presents the total control signal in the configuration space, which is a nonlinear mapping of the control signal in the task space. Due to practical reasons, knowledge of it is necessary to control the drives of the controlled object.

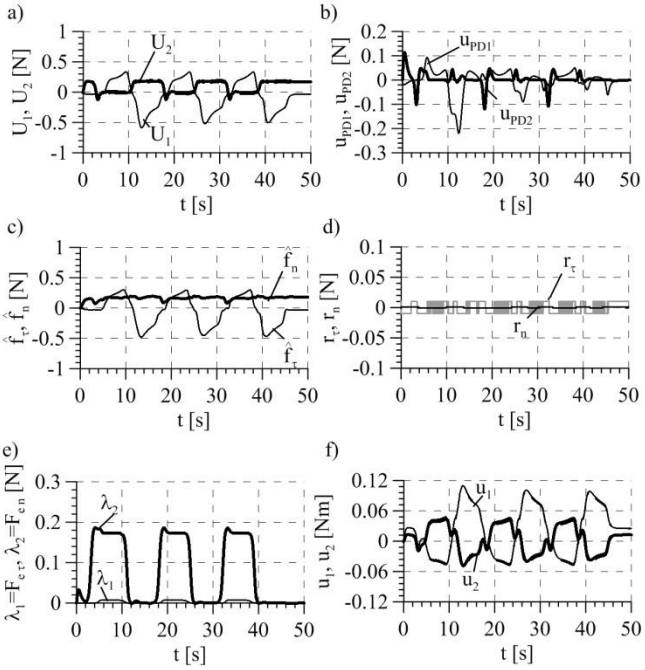

Fig. 4. Control signals: a) total control, b) PD control, c) compensative control, d) robust control, e) control of normal force λ_2 and control compensating for friction influence λ_1, f) control signal in the configuration space

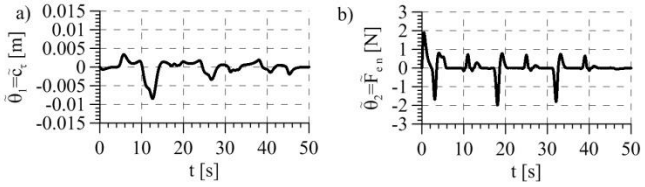

Fig. 5. Tracking errors: a) displacement on the tangent direction error, b) pressure force error

Tracking errors (Fig. 5) are typical for adapting systems, that is, the errors are the biggest during the initial control stage and then consequently they decrease, which is related to the neural network weights adaptation and increasingly better adjustment of the compensative control.

5. CONCLUSIONS

In the paper, the manipulator control algorithm is presented, which takes into account that the contact with flexible environment presented is unsusceptible to modelling imprecisions, both in terms of parameters and structure. It is possible due to the approximative features of artificial neural networks used for the compensation of system nonlinearity. Utilised system dynamics description and its control in a task space related to the environment space is very beneficial in practical applications, for which the main purpose is the realisation of the task of manipulator motion with a simultaneous pressure, utilised in process realisation.

DOI 10.2478/ama-2019-0003

REFERENCES

1. **Barata J.C.A., Hussein M.S.** (2012), The Moore–Penrose pseudoinverse: A tutorial review of the theory, *Brazilian Journal of Physics*, 42(1-2), 146–165.
2. **Birglen L., Schlicht T.** (2018), A statistical review of industrial robotic grippers, *Robotics and Computer-Integrated Manufacturing*, 49, 88–97.
3. **Burghardt A., Kurc K., Szybicki D., Muszyńska M., Nawrocki J.** (2017a), Software for the robot-operated inspection station for engine guide vanes taking into consideration the geometric variability of parts, *Tehnicki Vjesnik-Technical Gazette*, 24(2), 349–353.
4. **Burghardt A., Szybicki D., Kurc K., Muszyńska M., Mucha J.** (2017b), Experimental Study of Inconel 718 Surface Treatment by Edge Robotic Deburring with Force Control, *Strength Mater*, 49(4), 594–604.
5. **Canudas de Wit C.A., Siciliano B., Bastin G.** (Eds.) (1996), *Theory of robot control*, New York, Springer.
6. **Capisani L. M., Ferrara A.** (2012), Trajectory planning and second-order sliding mode motion/interaction control for robot manipulators in unknown environments, *IEEE Transactions on Industrial Electronics*, 59(8), 3189–3198.
7. **Denkena B., Bergmann B., Lepper T.** (2017), Design and optimization of a machining robot, *Procedia Manufacturing*, 14, 89–96.
8. **Duan J., Gan Y., Chen M., Dai X.** (2018), Adaptive variable impedance control for dynamic contact force tracking in uncertain environment, *Robotics and Autonomous Systems*, 102, 54–65.
9. **Galushkin A. I.** (2007). *Neural networks theory*, Springer Science & Business Media.
10. **Gierlak P.** (2012), Hybrid Position/Force Control of the SCORBOT-ER 4pc Manipulator with Neural Compensation of Nonlinearities, in: Rutkowski L., Korytkowski M., Scherer R., Tadeusiewicz R., Zadeh L.A., Zurada J.M. (eds) Artificial Intelligence and Soft Computing. ICAISC 2012. *Lecture Notes in Computer Science*, 7268, 433–441, Springer, Berlin, Heidelberg.
11. **Gierlak P.** (2014), Hybrid position/force control in robotised machining, *Solid State Phenomena*, 210, 192–199.
12. **Gierlak P.** (2018), Combined strategy for control of interaction force between manipulator and flexible environment, *Journal of Control Engineering and Applied Informatics*, 20(2), 64–75.
13. **Gierlak P., Szuster M.** (2017), Adaptive position/force control for robot manipulator in contact with a flexible environment, *Robotics and Autonomous Systems*, 95, 80–101.
14. **Gracia L., Solanes J.E., Muñoz-Benavent P., Miro J.V., Perez-Vidal C., Tornero J.** (2018), Adaptive Sliding Mode Control for Robotic Surface Treatment Using Force Feedback, *Mechatronics*, 52, 102–118.
15. **Hashemi S.M., Gürcüoğlu U., Werner H.** (2013), Interaction control of an industrial manipulator using LPV techniques, *Mechatronics*, 23(6), 689–699.
16. **Hendzel Z., Burghardt A., Gierlak P., Szuster M.** (2014), Conventional and fuzzy force control in robotised machining, *Solid State Phenomena*, 210, 178–185.
17. **Hertz J., Krogh A., Palmer R.G.** (1991), *Introduction to the theory of neural computation*, Boston, Addison-Wesley Longman Publishing Co.
18. **Iglesias I., Sebastián M.A., Are, J.E.** (2015), Overview of the state of robotic machining: Current situation and future potential, *Procedia engineering*, 132, 911–917.
19. **Jafari A., Ryu J.H.** (2016), Independent force and position control for cooperating manipulators handling an unknown object and interacting with an unknown environment, *Journal of the Franklin Institute*, 353(4), 857–875.
20. **Kumar N., Panwar V., Sukavanam N., Sharma S.P., Borm J.-H.** (2011), Neural network based hybrid force/position control for robot manipulators, *International Journal of Precision Engineering and Manufacturing*, 12(3), 419–426.
21. **Lewis F.L., Liu K., Yesildirek A.** (1995), Neural Net Robot Controller with Guaranteed Tracking Performance, *IEEE Transactions on Neural Networks*, 6(3), 701–715.
22. **Lotz M., Bruhm H., Czinki A.** (2014), An new force control strategy improving the force control capabilities of standard industrial robots, *Journal of Mechanics Engineering and Automation*, Vol. 4, 276–283.
23. **Mendes N., Neto P.** (2015), Indirect adaptive fuzzy control for industrial robots: a solution for contact applications, *Expert Systems with Applications*, 4 (22), 8929–8935.
24. **Narendra K., Annaswamy A.M.** (1987), A new adaptive law for robust adaptation without persistent excitation, *IEEE Transactions on Automatic Control*, 32(2), 134–145.
25. **Pao Y.-H., Park G.-H., Sobajic D.J.** (1994), Learning and generalization characteristics of the random vector functional-link net, *Neurocomputing*, 6(2), 163–180.
26. **Pliego-Jiménez J., Arteaga-Pérez M.A.** (2015), Adaptive position/force control for robot manipulators in contact with a rigid surface with uncertain parameters, *European Journal of Control*, 22, 1–12.
27. **Polycarpou M.M., Ioannu P.A.** (1991), *Identification and control using neural network models: design and stability analysis*, California, University of Southern California.
28. **Ravandi A. K., Khanmirza E., Daneshjou K.** (2018), Hybrid force/position control of robotic arms manipulating in uncertain environments based on adaptive fuzzy sliding mode control. *Applied Soft Computing*, 70, 864–874.
29. **Tian F., Lv C., Li Z., Liu G.** (2016), Modeling and control of robotic automatic polishing for curved surfaces, *CIRP Journal of Manufacturing Science and Technology*, 14, 55–64.
30. **Vukobratovič M., Ekalo Y., Rodič A.** (2002), How to Apply Hybrid Position/Force Control to Robots Interacting with Dynamic Environment, In: Bianchi G., Guinot J.-C., Rzymkowski C. (Eds.) *Romansy*, 14, 249–258, Vienna.
31. **Zhu D., Luo S., Yang L., Chen W., Yan S., Ding H.** (2015), On energetic assessment of cutting mechanisms in robot-assisted belt grinding of titanium alloys, *Tribology International*, 90, 55–59.
32. **Żylski W., Gierlak P.** (2010), Verification of Multilayer Neural-Net Controller in Manipulator Tracking Control, *Solid State Phenomena*, 164, 99–104.

sciendo

DOI 10.2478/ama-2019-0004

acta mechanica et automatica, vol.13 no.1 (2019)

NUMERICAL SOLUTION OF NATURAL CONVECTIVE HEAT TRANSFER UNDER MAGNETIC FIELD EFFECT

Serpil ŞAHİN,[*] Hüseyin DEMİR[**]

[*]Faculty of Arts and Sciences, Department of Mathematics, Amasya University, 05000, İpekköy, Amasya, Turkey
[**]Faculty of Arts and Sciences, Department of Mathematics, Ondokuz Mayıs University, 55200, Atakum, Samsun, Turkey

serpil.sahin@amasya.edu.tr, hdemir@omu.edu.tr

received 3 August 2018, revised 7 March 2019, accepted 13 March 2019

Abstract: In this study, non-Newtonian pseudoplastic fluid flow equations for 2-D steady, incompressible, the natural convective heat transfer are solved numerically by pseudo time derivative. The stability properties of natural convective heat transfer in an enclosed cavity region heated from below under magnetic field effect are investigated depending on the Rayleigh and Chandrasekhar numbers. Stability properties are studied, in particular, for the Rayleigh number from $\mathbf{10^4}$ to $\mathbf{10^6}$ and for the Chandrasekhar number 3, 5 and 10. As a result, when Rayleigh number is bigger than $\mathbf{10^6}$ and Chandrasekhar number is bigger than 10, the instability occurs in the flow domain. The results obtained for natural convective heat transfer problem are shown in the figures for Newtonian and pseudoplastic fluids. Finally, the local Nusselt number is evaluated along the bottom wall.

Key words: Natural convective heat transfer, Rayleigh number, Chandrasekhar number, pseudo time derivative, Newtonian fluids, pseudoplastic fluids

1. INTRODUCTION

The stability and thermal convection in an enclosure have been subject of theoretical research since the time of Rayleigh (1916). Although the study of internal convection flows is more complicated than external flows, there has recently been a considerable interest in convection flows within closed geometries such as squares or rectangles. Thermal convection in enclosures occurs in many industrial applications such as building insulation, solar energy, and the electrical and nuclear industries. There are, for example, applications in heat transfer across double glazing windows and in sterilization of foods. Such flows are also of interest in geophysics so that several important examples can be applied in the circulation of the atmosphere and of magma in the Earth's upper mantle. Reviews of the literature for two-dimensional free convection of rectangular enclosures have been reported by Gebhart et al. (1988) and Siginer and Valenzuela-Rendon (1994).

The vertical cavity, with two vertical walls at different temperatures, is probably the most studied configuration due to its simplicity and importance. In a horizontal cavity, with heating from below, we have thermal instability. The other important phenomena in both cases are the buoyancy term involved in the flow equation. In thermal convection, the fluid density is no longer constant and depends on temperature in buoyancy term. Therefore, in such a region, the temperature of the cold wall T_0 is used as a reference to give the buoyancy term as $\rho\beta(T - T_0)$, where β is the constant coefficient of thermal expansion, ρ is the density of the fluid and T is the temperature (Tennehil et al., 1997).

Although many fluids encountered in various industries exhibit non-Newtonian behaviour, there are very few studies reported in the literature for thermal convection problems. Two surveys by Shenoy (1988) and Gebhart et al. (1988) mention only two studies on natural convection in enclosures.

Newtonian free convection has been extensively studied by Batchelor (1956), Elder (1965), Wilkes and Churchill (1966) and De Vahl Davis (1983). Emery et al. (1971) experimentally determined a correlation for the case of one wall at a constant temperature and a condition of constant heat flux at the other vertical wall for several pseudoplastic power law fluids.

Numerical methods are frequently used for two dimensional steady incompressible Newtonian flow problems. Due to the simplicity of cavity geometry, numerical methods can be applied very easily and effectively to this type of flow problems and results are very satisfactory.

For such studies, Benjamin and Denny (1979) have used a method that is relaxed by means of ADI methods using a non-uniform iteration parameter. Full converged solutions at Reynolds number up to 10^4 with three different grid mesh sizes (maximum being 101×101) are generated in order to resolve basic questions on the nature of the flow and to explore convergence properties of the method.

Schereiber and Keller (1983) have introduced efficient and reliable numerical techniques of high-order accuracy for solving problems of steady viscous incompressible flow in the plane with these techniques, they obtain accurate solutions for the driven cavity. The numerical methods combine an efficient linear system solver and an adaptive Newton-like method for nonlinear systems. They have obtained solutions at Reynolds number 10000 on a 180×180.

Hou et al. (1995) have used Lattice Boltzmann Method for the simulation of the cavity flow. They have used 256×256 grid points and presented solutions for Reynolds number $\mathrm{Re} \leq 7500$.

Khader (2016) is devoted to introduce a numerical simulation with a theoretical study for the flow of a Newtonian fluid over an impermeable stretching sheet, which is embedded in a porous medium with a power law surface velocity and variable thickness in the presence of thermal radiation.

DOI 10.2478/ama-2019-0004

Liao and Zhu (1996) have introduced a higher order stream function-vorticity boundary element method (BEM) formulation for the solution of Navier-Stokes equations. With this, they have presented solutions up to $\mathrm{Re} = 10000$ with a grid mesh of 257×257.

Ghia et al. (1982) have applied a multi-grid strategy to the coupled strongly implicit method developed by Rubin and Khosla (1981). They have presented solutions for Reynolds number as high as $\mathrm{Re} = 10000$ with meshes consisting of as many as 257×257 grid points.

Erturk et al. (2005) have introduced an effective numerical method for driven cavity flow by using stream function and vorticity formulation. Using a regular grid size of 601×601, they have solved the Navier-Stokes equations for $\mathrm{Re} \leq 21000$.

In the past decades, various numerical approaches have been used to solve magnetohydrodynamics (MHD) flows. A mixed finite element method has been discussed by Gunzburger et al. (1991). In Hasler et al. (2004), a weighted regularization approach has been applied to incompressible MHD system. Salah et al. (2001) have presented a Galerkin least-square method. Siddheswar et al. (2011) have introduced the higher order Rayleigh-Ritz (HORR) method, which is used to obtain the eigenvalue of the problem. Rudraiah et al. (1995) and Venkatachalappa et al. (2011) have used ADI (Alternating Direction Implicit) and SLOR (Successive Line Over Relaxation) method. Additionally, Amber and O'Donovan (2017) have presented two-dimensional simulations of natural convection driven by the absorption of nonuniform concentrated solar radiation in a molten binary salt-filled enclosure inclined at $0 \leq \varphi \leq 60$.

Recently, three classical iterative algorithms (Stokes iterative method, Newton iterative Method and Oseen iterative method) of solving 2D/3D Navier Stokes equations have been considered by He and Li (2009), Xu and He (2013).

Motivated by Erturk et al. (2005), this article is mainly focused on numerical solutions of natural convective heat transfer in an enclosed cavity heated from below.

2. NUMERICAL METHOD

The following figures schematically represent the flow in an enclosed cavity region heated from below under a magnetic field effect.

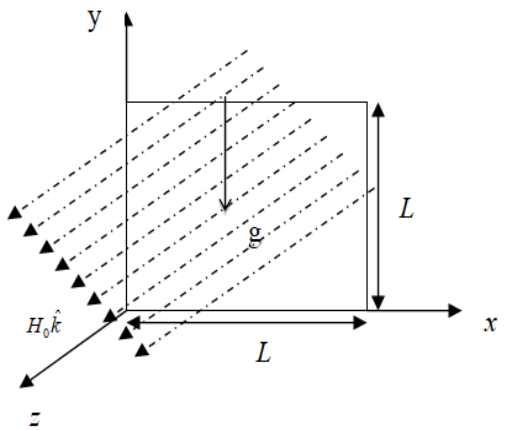

Fig. 1. Physical configuration and description of boundary condition

In Fig. 1, L is the characteristic length, g is the gravitational acceleration, H_0 is the applied magnetic field and $\hat{\mathrm{k}}$ is a unit vector in the increasing direction of the space variable z.

We use the stream function (ψ), vorticity (ω) and temperature (T) formulation of the steady-state incompressible pseudo-plastic viscous fluid equations in the following form:

$$u\frac{\partial\omega}{\partial x} + v\frac{\partial\omega}{\partial y} = \frac{1}{\mathrm{Re}\eta(q)}\left\{\frac{\partial}{\partial x}\left(\eta^2(q)\frac{\partial\omega}{\partial x}\right) + \frac{\partial}{\partial y}\left(\eta^2(q)\frac{\partial\omega}{\partial y}\right)\right\} + \frac{1}{\mathrm{Re}}\left\{-4\frac{\partial^2\psi}{\partial x\,\partial y}\frac{\partial^2\eta(q)}{\partial x\,\partial y} - \left(\frac{\partial^2\psi}{\partial y^2} - \frac{\partial^2\psi}{\partial x^2}\right)\left(\frac{\partial^2\eta(q)}{\partial y^2} - \frac{\partial^2\eta(q)}{\partial x^2}\right) + \frac{Gr}{\mathrm{Re}}\frac{\partial T}{\partial x} - Q\omega\right\} \quad (1)$$

$$\frac{\partial^2\psi}{\partial x^2} + \frac{\partial^2\psi}{\partial y^2} = -\omega \quad (2)$$

$$u\frac{\partial T}{\partial x} + v\frac{\partial T}{\partial y} = \frac{1}{\mathrm{PrRe}}\nabla^2 T \quad (3)$$

$$u = \frac{\partial\psi}{\partial y}, v = -\frac{\partial\psi}{\partial x} \quad (4)$$

where, $\mathrm{Re} = \frac{\rho \mathrm{VL}}{\eta(0)}$ is the Reynolds number, $\mathrm{Gr} = \frac{\mathrm{g}\beta(\mathrm{T}_1 - \mathrm{T}_0)\mathrm{L}^3}{\upsilon^2}$ is the Grashof number, $\mathrm{Pr} = \frac{c\eta(0)}{\mathrm{k}}$ is the Prandtl number, $Q = \frac{\mu_m^2 \sigma \mathrm{H}_0^2 \mathrm{L}}{u\rho}$ is the Chandrasekhar number, q is the shear rate, $\eta(q)$ is the viscosity, x and y are the Cartesian coordinates, μ_m is the magnetic permeability, σ is the surface tension gradient, u is the velocity component in the x-axis direction and ρ is the density. Also, the Rayleigh number can be written as the product of the Grashof number, which describes the relationship between buoyancy and viscosity within a fluid, and the Prandtl number, which describes the relationship between momentum diffusivity and thermal diffusivity, that is, $\mathrm{Ra} = \mathrm{Gr}.\mathrm{Pr}$. Finally, the Cross model is used in this work for the modelling of the viscosity function and this has the following form:

$$\eta(q) = \eta(\infty) + \frac{(\eta(0) - \eta(\infty))}{1 + (\lambda q)^{1-n}}.$$

In this Cross Model, $\eta(\infty)$ represents the infinite shear viscosity for very large deformation rates and $\eta(0)$ represents the zero shear rate viscosity for very small rates of shear. Assuming $n = 0.5, \lambda = 1, \eta(0) = 1$ and $0 \leq \eta(\infty) \leq 1$, we obtain shear-thinning or the so-called pseudoplastic behaviour.

The first order pseudo time derivatives are now introduced so that the equations (1), (2) and (3) take the following form:

$$\frac{\partial\omega}{\partial t} = -\frac{\partial\psi}{\partial y}\frac{\partial\omega}{\partial x} + \frac{\partial\psi}{\partial x}\frac{\partial\omega}{\partial y} + \frac{1}{\mathrm{Re}\eta(q)}\left\{\frac{\partial}{\partial x}\left(\eta^2(q)\frac{\partial\omega}{\partial x}\right) + \frac{\partial}{\partial y}\left(\eta^2(q)\frac{\partial\omega}{\partial y}\right)\right\} + \frac{1}{\mathrm{Re}}\left\{-4\frac{\partial^2\psi}{\partial x\,\partial y}\frac{\partial^2\eta(q)}{\partial x\,\partial y} - \left(\frac{\partial^2\psi}{\partial y^2} - \frac{\partial^2\psi}{\partial x^2}\right)\left(\frac{\partial^2\eta(q)}{\partial y^2} - \frac{\partial^2\eta(q)}{\partial x^2}\right) + \frac{Gr}{\mathrm{Re}}\frac{\partial T}{\partial x} - Q\omega\right\} \quad (5)$$

$$\frac{\partial\psi}{\partial t} = \frac{\partial^2\psi}{\partial x^2} + \frac{\partial^2\psi}{\partial y^2} + \omega \quad (6)$$

$$\frac{\partial T}{\partial t} = -\frac{\partial\psi}{\partial y}\frac{\partial T}{\partial x} + \frac{\partial\psi}{\partial x}\frac{\partial T}{\partial y} + \frac{1}{\mathrm{PrRe}}\nabla^2 T \quad (7)$$

Using forward difference approximation for the time derivatives in equations (5), (6) and (7), we obtain the following equations (Smith, 1978):

$$\left(1-\frac{\Delta t}{\mathrm{Re}}\eta^n\frac{\partial^2}{\partial x^2}+\Delta t\left(\frac{\partial\psi}{\partial y}\right)^n\frac{\partial}{\partial x}-2\frac{\Delta t}{\mathrm{Re}}\left(\frac{\partial\eta}{\partial x}\right)^n\frac{\partial}{\partial x}\right)$$
$$\times\left(1-\frac{\Delta t}{\mathrm{Re}}\eta^n\frac{\partial^2}{\partial y^2}-\Delta t\left(\frac{\partial\psi}{\partial x}\right)^n\frac{\partial}{\partial y}-2\frac{\Delta t}{\mathrm{Re}}\left(\frac{\partial\eta}{\partial y}\right)^n\frac{\partial}{\partial y}\right)\omega^{n+1}$$
$$=\omega^n+\frac{\Delta t}{\mathrm{Re}}\left\{-4\left(\frac{\partial^2\psi}{\partial x\,\partial y}\right)^n\left(\frac{\partial^2\eta}{\partial x\,\partial y}\right)^n-\left[\left(\frac{\partial^2\psi}{\partial y^2}\right)^n-\left(\frac{\partial^2\psi}{\partial x^2}\right)^n\right]\right. \quad (8)$$
$$\left.\times\left[\left(\frac{\partial^2\eta}{\partial y^2}\right)^n-\left(\frac{\partial^2\eta}{\partial x^2}\right)^n\right]+\frac{Gr}{\mathrm{Re}}\left(\frac{\partial T}{\partial x}\right)^n-Q\omega^n\right\}$$

$$\left(1-\Delta t\frac{\partial^2}{\partial x^2}\right)\left(1-\Delta t\frac{\partial^2}{\partial y^2}\right)\psi^{n+1}=\psi^n+\Delta t\omega^n \quad (9)$$

$$\left(1-\frac{\Delta t}{\mathrm{PrRe}}\frac{\partial^2}{\partial x^2}+\Delta t\left(\frac{\partial\psi}{\partial y}\right)^n\frac{\partial}{\partial x}\right)\left(1-\frac{\Delta t}{\mathrm{PrRe}}\frac{\partial^2}{\partial y^2}\right.$$
$$\left.-\Delta t\left(\frac{\partial\psi}{\partial x}\right)^n\frac{\partial}{\partial y}\right)T^{n+1}=T^n \quad (10)$$

In the event of reaching a steady state, we have:

$$\psi^{n+1}=\psi^n\,, \quad (11)$$

$$\omega^{n+1}=\omega^n\,, \quad (12)$$

and

$$T^{n+1}=T^n\,. \quad (13)$$

Using this result in the right hand side of equations (8), (9) and (10), we may write:

$$\left(1-\frac{\Delta t}{\mathrm{Re}}\eta^n\frac{\partial^2}{\partial x^2}+\Delta t\left(\frac{\partial\psi}{\partial y}\right)^n\frac{\partial}{\partial x}-2\frac{\Delta t}{\mathrm{Re}}\left(\frac{\partial\eta}{\partial x}\right)^n\frac{\partial}{\partial x}\right)$$
$$\times\left(1-\frac{\Delta t}{\mathrm{Re}}\eta^n\frac{\partial^2}{\partial y^2}-\Delta t\left(\frac{\partial\psi}{\partial x}\right)^n\frac{\partial}{\partial y}-2\frac{\Delta t}{\mathrm{Re}}\left(\frac{\partial\eta}{\partial y}\right)^n\frac{\partial}{\partial y}\right)\omega^{n+1}$$
$$=\omega^n+\frac{\Delta t}{\mathrm{Re}}\left\{-4\left(\frac{\partial^2\psi}{\partial x\,\partial y}\right)^n\left(\frac{\partial^2\eta}{\partial x\,\partial y}\right)^n-\left[\left(\frac{\partial^2\psi}{\partial y^2}\right)^n-\left(\frac{\partial^2\psi}{\partial x^2}\right)^n\right]\right.$$
$$\left.\times\left[\left(\frac{\partial^2\eta}{\partial y^2}\right)^n-\left(\frac{\partial^2\eta}{\partial x^2}\right)^n\right]+\frac{Gr}{\mathrm{Re}}\left(\frac{\partial T}{\partial x}\right)^n-Q\omega^n\right\}+\left(\frac{\Delta t}{\mathrm{Re}}\eta^n\frac{\partial^2}{\partial x^2}\right. \quad (14)$$
$$-\Delta t\left(\frac{\partial\psi}{\partial y}\right)^n\frac{\partial}{\partial x}+2\frac{\Delta t}{\mathrm{Re}}\left(\frac{\partial\eta}{\partial x}\right)^n\frac{\partial}{\partial x}\Big)\times\left(\frac{\Delta t}{\mathrm{Re}}\eta^n\frac{\partial^2}{\partial y^2}\right.$$
$$\left.+\Delta t\left(\frac{\partial\psi}{\partial x}\right)^n\frac{\partial}{\partial y}+2\frac{\Delta t}{\mathrm{Re}}\left(\frac{\partial\eta}{\partial y}\right)^n\frac{\partial}{\partial y}\right)\omega^n$$

$$\left(1-\Delta t\frac{\partial^2}{\partial x^2}\right)\left(1-\Delta t\frac{\partial^2}{\partial y^2}\right)\psi^{n+1}=\psi^n+\Delta t\omega^n$$
$$+\left(\Delta t\frac{\partial^2}{\partial x^2}\right)\left(\Delta t\frac{\partial^2}{\partial y^2}\right)\psi^n \quad (15)$$

$$\left(1-\frac{\Delta t}{\mathrm{PrRe}}\frac{\partial^2}{\partial x^2}+\Delta t\left(\frac{\partial\psi}{\partial y}\right)^n\frac{\partial}{\partial x}\right)\left(1-\frac{\Delta t}{\mathrm{PrRe}}\frac{\partial^2}{\partial y^2}\right.$$
$$\left.-\Delta t\left(\frac{\partial\psi}{\partial x}\right)^n\frac{\partial}{\partial y}\right)T^{n+1}=T^n+\left(\frac{\Delta t}{\mathrm{PrRe}}\frac{\partial^2}{\partial x^2}\right. \quad (16)$$
$$\left.-\Delta t\left(\frac{\partial\psi}{\partial y}\right)^n\frac{\partial}{\partial x}\right)\times\left(\frac{\Delta t}{\mathrm{PrRe}}\frac{\partial^2}{\partial y^2}+\Delta t\left(\frac{\partial\psi}{\partial x}\right)^n\frac{\partial}{\partial y}\right)T^n$$

The solution method for the equations (14), (15) and (16) involves a two-level updating. First, the stream function equation is solved. For equation (15), the variable f is introduced such that:

$$\left(1-\Delta t\frac{\partial^2}{\partial y^2}\right)\psi^{n+1}=f\,, \quad (17)$$

and:

$$\left(1-\Delta t\frac{\partial^2}{\partial x^2}\right)f=\psi^n+\Delta t\omega^n+\left(\Delta t\frac{\partial^2}{\partial x^2}\right)\left(\Delta t\frac{\partial^2}{\partial y^2}\right)\psi^n. \quad (18)$$

In equation (18), f is the only unknown and is first solved at each grid point. Following this, the stream function variable(ψ) is advanced into the new time level using equation (17). Next, the vorticity and energy equations are solved in a similar fashion.

The local Nusselt number (*Nu*) has been evaluated along the bottom wall with the expression:

$$Nu=\frac{\partial T}{\partial y}\Big|_{\;y=0}$$

where, T is the dimensionless temperature.

3. RESULTS AND DISCUSSION

We use the symmetry for , ψ and T at spurious points outside the boundaries. On the boundaries, the values of vorticity are chosen from the nine-point compact finite difference.

Left Boundary Right Boundary

$$\psi_{-1,j}=\psi_{1,j}\,,\psi_{0,j}=0\;\psi_{N+1,j}=\psi_{N-1,j}\,,\psi_{N,j}=0$$
$$u=v=0\,,\frac{\partial T}{\partial x}=0\quad u=v=0\,,\frac{\partial T}{\partial x}=0$$
$$\omega_{0,j}=-\left(\frac{\partial^2\psi}{\partial x^2}\right)_{0,j}\quad \omega_{N,j}=-\left(\frac{\partial^2\psi}{\partial x^2}\right)_{N,j}$$

Bottom Boundary Top Boundary

$$\psi_{i,-1}=\psi_{i,1}\,,\psi_{i,0}=0\;\psi_{i,N+1}=\psi_{i,N-1}\,,\psi_{i,N}=0$$
$$u=v=0\,,T=T_0\quad u=v=0\,,T=T_1$$
$$\omega_{i,0}=-\left(\frac{\partial^2\psi}{\partial y^2}\right)_{i,0}\quad \omega_{i,N}=-\left(\frac{\partial^2\psi}{\partial y^2}\right)_{i,N}$$

We use the same algorithm with Erturk et al. (2001), but our convergence criterion is different. The convergence criterion that was used was based on the relative-error criterion (Demir, 2005):

$$\max\left\{\frac{\left|\psi^{n+1}-\psi^n\right|}{1+\left|\psi^n\right|}\right\}<10^{-6}\,,\forall n\,,$$
$$\max\left\{\frac{\left|\omega^{n+1}-\omega^n\right|}{1+\left|\omega^n\right|}\right\}<10^{-6}\,,\forall n\,,$$
$$\max\left\{\frac{\left|T^{n+1}-T^n\right|}{1+\left|T^n\right|}\right\}<10^{-10}\,,\forall n\,.$$

Tab. 1 tabulates the maximum stream function value, the vorticity value at the centre of the primary vortex and also the centre location of the primary vortex for Newtonian fluid at $\mathrm{Re}=1000$ along with similar results found in the literature are compared. In Tab. 1, among the most significant results, Erturk et al. (2005) have solved the cavity flow on three different grid meshes ($401\times401\,,513\times513\,,601\times601$) for $\mathrm{Re}=1000$.

Looking back to Tab. 1, for $\mathrm{Re}=1000$, our results are in very good agreement with the results of Schreiber and Keller (1983), Hou et al. (1995) and Erturk et al. (2005). From all these

DOI 10.2478/ama-2019-0004

comparisons, we can conclude that even for $\mathrm{Re} = 1000$, higher order approximations together with the use of fine grids are necessary for accuracy.

Stream and temperature lines corresponding to $\mathrm{Q} = 0$ and $\mathrm{Q} = 5, \mathrm{Ra} = 10^4, \mathrm{Ra} = 10^5$ and $\mathrm{Ra} = 10^6$ are given for Newtonian, pseudoplastic fluids and pseudoplastic fluids under the magnetic field effect in the following figures, respectively. Also, all the figures are presented in xy plane.

Tab. 1. Comparison of the properties of the primary vortex; the maximum stream function value, the vorticity value and the location of the centre, for Newtonian fluid at $\mathrm{Re} = 1000$

Reference	Grid	ψ	ω	x	y
Erturk et al. (2005)	401×401	0.118585	2.062761	0.5300	0.5650
	513×513	0.118722	2.064765	0.5313	0.5645
	601×601	0.118781	2.065530	0.5300	0.5650
Schreiber and Keller (1983)	121×121	0.11492	2.0112	-	-
	141×141	0.11603	2.0268	0.52857	0.56429
Ghia et al. (1982)	129×129	0.117929	2.04968	0.5313	0.5625
Hou et al. (1995)	256×256	0.1178	2.0760	0.5333	0.5647
Liao et al. (1996)	129×129	0.1160	2.0234	0.5313	0.5625
Benjamin et al. (1979)	101×101	0.1175	2.044	-	-
Present	128×128	0.115952	2.02482	0.5313	0.5625
	256×256	0.118182	2.05677	0.5313	0.5664
	401×401	0.118626	2.06322	0.5312	0.5661

(a) $128 \times 128, Ra = 10^4, Q = 0$ **(b)** $128 \times 128, Ra = 10^4, Q = 0$ **(c)** $128 \times 128, Ra = 10^4, Q = 5$

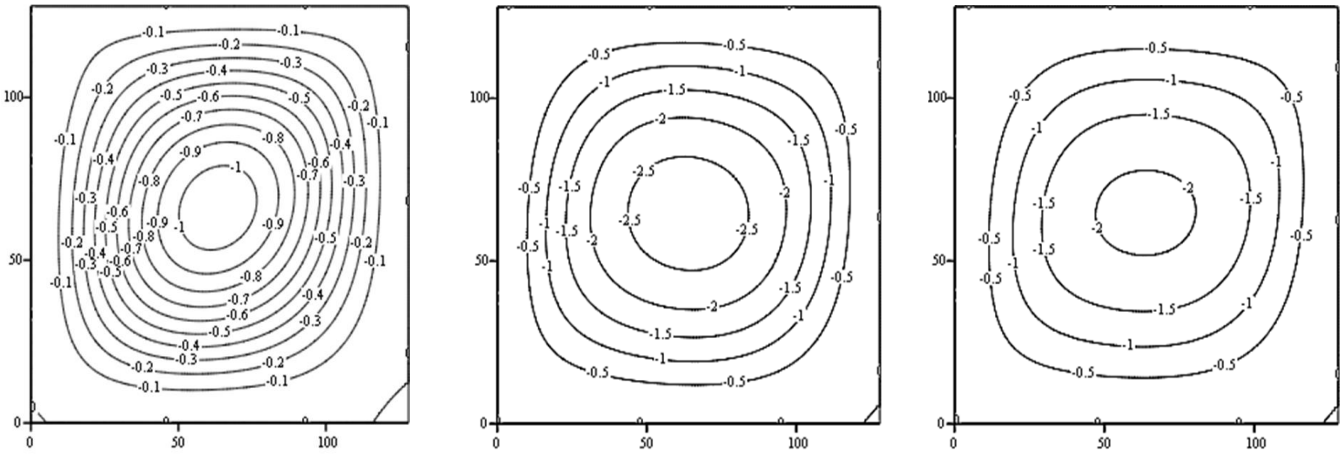

Fig. 2. Streamline contours for (a) Newtonian, (b) pseudoplastic fluids and (c) pseudoplastic fluids under the magnetic field effect at $Ra = 10^4$, respectively

(a) $128 \times 128, Ra = 10^4, Q = 0$ **(b)** $128 \times 128, Ra = 10^4, Q = 0$ **(c)** $128 \times 128, Ra = 10^4, Q = 5$

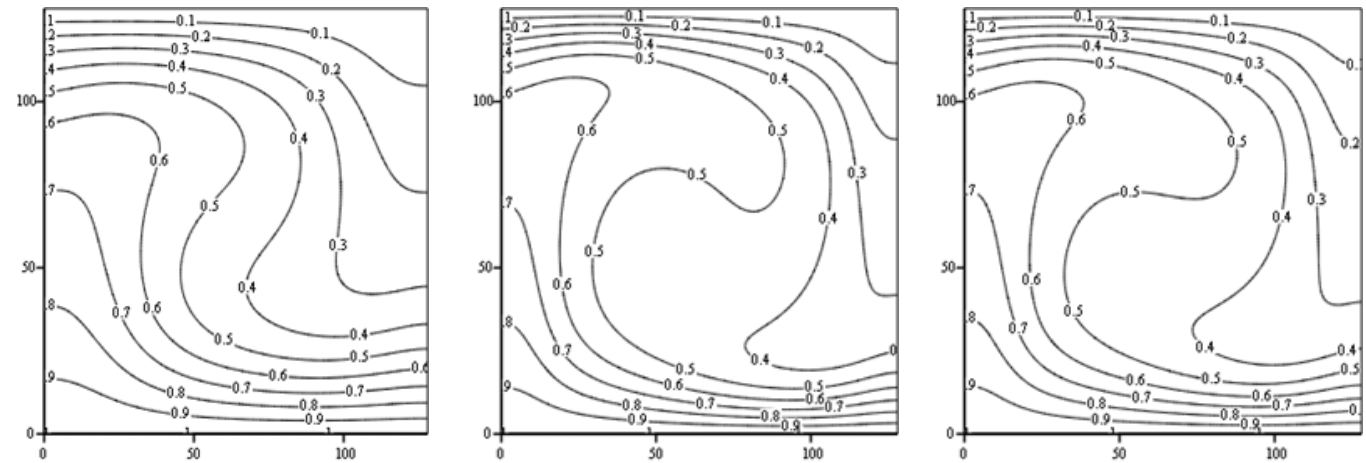

Fig. 3. Temperature contours for (a) Newtonian, (b) pseudoplastic fluids and (c) pseudoplastic fluids under the magnetic field effect at $Ra = 10^4$, respectively

(a) $128 \times 128, Ra = 10^5, Q = 0$ **(b)** $128 \times 128, Ra = 10^5, Q = 0$ **(c)** $128 \times 128, Ra = 10^5, Q = 5$

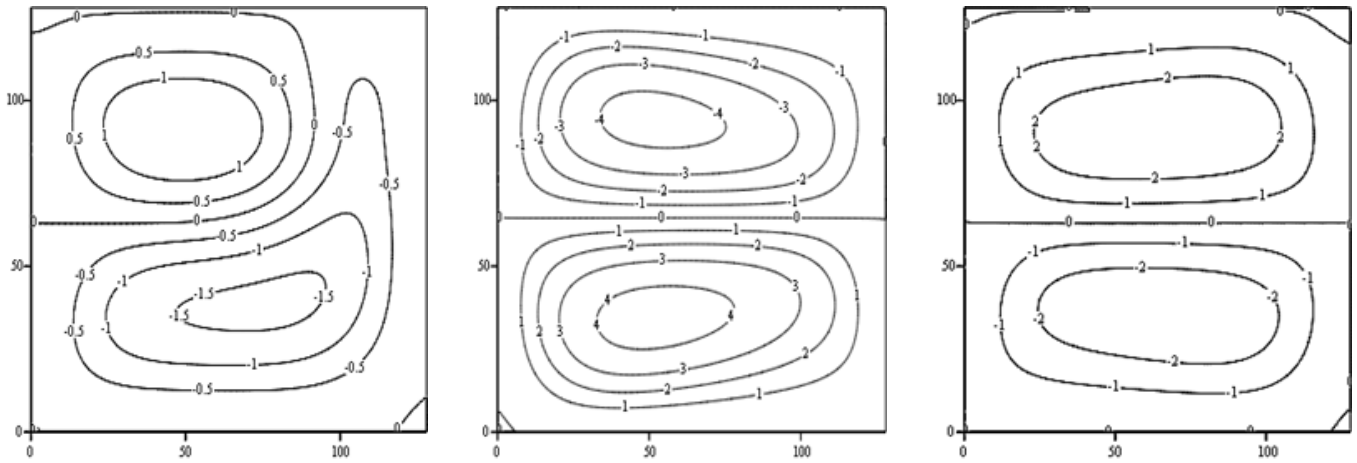

Fig. 4. Streamline contours for (a) Newtonian, (b) pseudoplastic fluids and (c) pseudoplastic fluids under the magnetic field effect at $Ra = 10^5$, respectively

(a) $128 \times 128, Ra = 10^5, Q = 0$ **(b)** $128 \times 128, Ra = 10^5, Q = 0$ **(c)** $128 \times 128, Ra = 10^5, Q = 5$

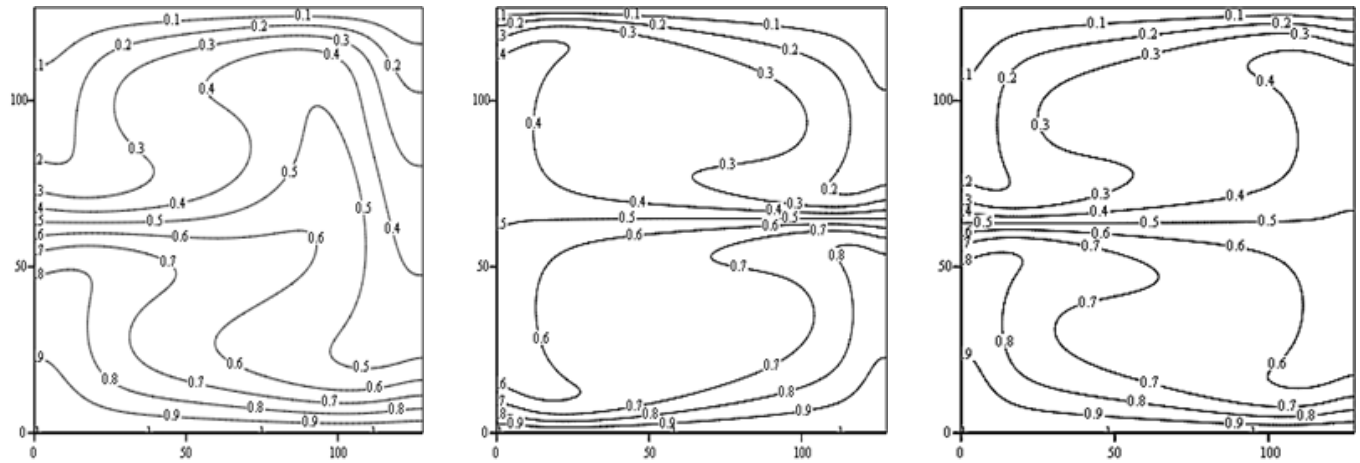

Fig. 5. Temperature contours for (a) Newtonian, (b) pseudoplastic fluids and (c) pseudoplastic fluids under the magnetic field effect at $Ra = 10^5$, respectively

(a) $128 \times 128, Ra = 10^6, Q = 0$ **(b)** $128 \times 128, Ra = 10^6, Q = 0$ **(c)** $128 \times 128, Ra = 10^6, Q = 5$

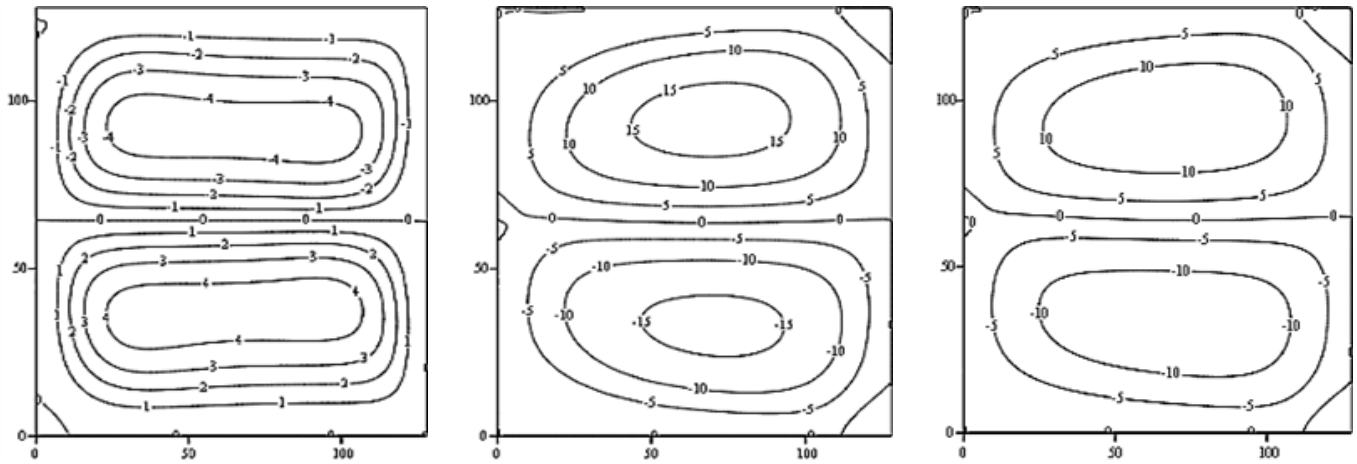

Fig. 6. Streamline contours for (a) Newtonian, (b) pseudoplastic fluids and (c) pseudoplastic fluids under the magnetic field effect at $Ra = 10^6$, respectively

DOI 10.2478/ama-2019-0004

(a) $128 \times 128, Ra = 10^6, Q = 0$ **(b)** $128 \times 128, Ra = 10^6, Q = 0$ **(c)** $128 \times 128, Ra = 10^6, Q = 5$

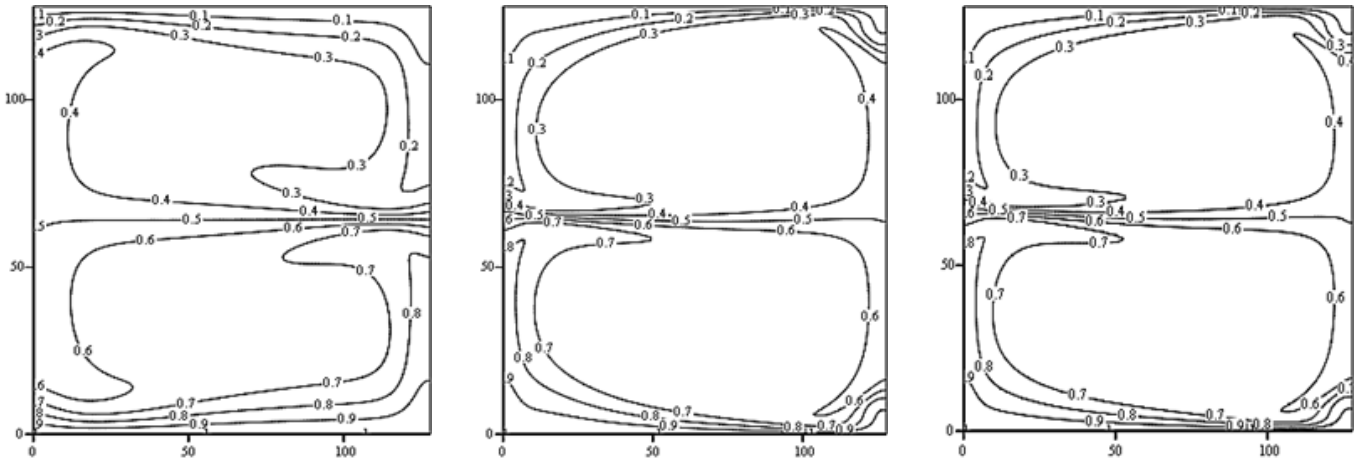

Fig. 7. Temperature contours for (a) Newtonian, (b) pseudoplastic fluids and (c) pseudoplastic fluids under the magnetic field effect at $Ra = 10^6$, respectively

For all fluids considered, as shown in Fig. 2, it has found one cell filled whole cavity at $Ra = 10^4$. The corresponding temperature profiles are shown in Fig. 3. For Newtonian, pseudoplastic fluids without any magnetic field effect and pseudoplastic fluids under the magnetic field effect, warm fluid rises near the left wall with the colder fluid falling near the opposite wall. As shown in Fig. 4, the Newtonian fluid solution consists of two counter rotating cells and they are not symmetric; one vortex dominates the other vortex, whereas for pseudoplastic fluid without any magnetic field effect and pseudoplastic fluids under the magnetic field effect, we have two mirror image counter rotating the cells. Fig. 5 indicates that it is almost symmetric horizontally and warm fluid rises near the bottom while colder fluid is located near the top wall. As shown in Fig. 6, for Newtonian, pseudoplastic fluids without any magnetic field effect and pseudoplastic fluids under the magnetic field effect, streamline contours have two mirror image counter rotating cells. And finally in Fig. 7, temperature distribution is dense only near the wall and temperature contours are symmetric. Consequently, when *Ra* increases, streamline and temperature contours consist of two counter rotating cells, which are symmetric. As shown in all the figures, for pseudoplastic fluids, under the magnetic field effect, the intensity of the streamlines is decreased.

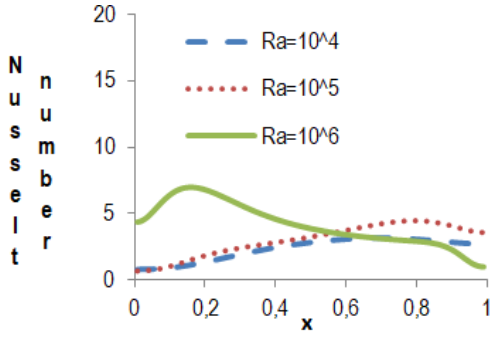

Fig. 8. Effect of local Nusselt number for Newtonian fluids

Fig. 8, 9 and 10 are respectively the plots of the local Nusselt number (Nu) evaluated along the bottom wall for Newtonian, pseudoplastic fluids without any magnetic field effect and pseudoplastic fluids under the magnetic field effect. As shown in Fig. 8, for $Ra = 10^4$ and $Ra = 10^5$, the local Nusselt number has high values on the right wall, but it has low values for $Ra = 10^6$ on the same wall. In Fig. 9, for $Ra = 10^4$, the local Nusselt number has increased, but for $Ra = 10^5$, it has decreased, and on the right wall, there is almost no convective heat transfer. For $Ra = 10^6$, the local Nusselt number has reached up to a maximum level, and on the right and left walls, there is low convective heat transfer. Finally, in Fig. 10, the local Nusselt number results under the magnetic field effect are similar to the results obtained for Newtonian fluids without any magnetic field effect. As seen in Fig. 10, the magnetic field has made some effects for only $Ra = 10^6$.

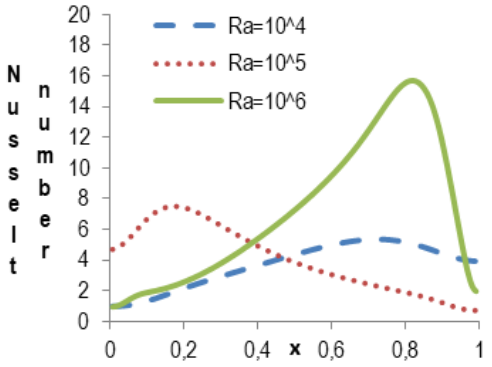

Fig. 9. Effect of local Nusselt number for pseudoplastic fluids without any magnetic field effect

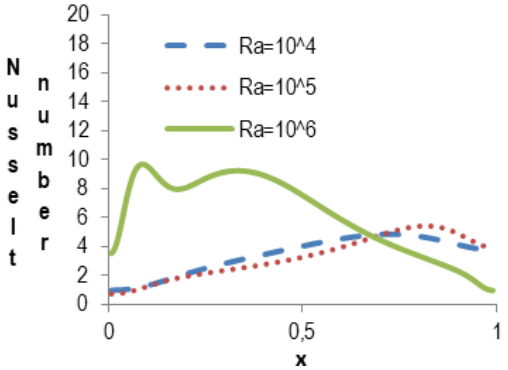

Fig. 10. Effect of local Nusselt number for pseudoplastic fluids under the magnetic field effect

4. CONCLUSIONS

This paper mainly consisted of the computer simulation and the analysis of the streamline and temperature structures of 2D steady-state, incompressible fluid flow in an enclosed cavity region heated from below under the magnetic field effect. For Rayleigh number up to $Ra = 10^6$ and Chandrasekhar number up to 10, the results have been presented and documented for the first time. The flow equations in stream function, vorticity and temperature formulation for pseudoplastic fluids were solved computationally using the numerical method described. In this numerical approach, the stream function, vorticity and energy equations were solved separately by using pseudo time derivative. For each equation, the numerical formulation required the solution of two tridiagonal systems, which allowed the use of large grid meshes easily and we used a fine grid mesh of 128×128. The method proved to be very effective on flow problems that required high accuracy on very fine grid meshes (Ertruk and Corke, 2001; Ertruk et al., 2004).

Our computations showed that fine grid mesh was necessary in order to obtain a steady solution, and when Ra and Q increased, streamline and temperature contours consisted of two counter rotating cells, which were symmetric. As a result, we obtained that when Rayleigh number is bigger than 10^6 and Chandrasekhar number is bigger than 10, instability occurs in the flow domain.

REFERENCES

1. **Amber I., O'Donovan T. S.** (2017), A numerical simulation of heat transfer in an enclosure with a nonlinear heat source, *Numerical Heat Transfer, Part A: Applications*, 71(11), 1081–1093.
2. **Batchelor G. K.** (1956), Steady laminar flow with closed streamlines at large Reynolds number, *J. Fluid Mech.,* 1, 177–190.
3. **Benjamin A. S., Denny V. E.** (1979), On the convergence of numerical solutions for 2-D flows in a cavity at large Re, *J. Comp. Physics*, 33, 340–358.
4. **De Vahl Davis G.** (1983), Natural convection of air in a square cavity: A bench mark numerical solution, *Int. J. for Num. Meth. in Fluids*, 3, 249–264.
5. **Demir H.** (2005), Numerical modeling of viscoelastic cavity driven flow using finite difference simulations, *Appl. Math. and Comp*., 166, 64–83.
6. **Elder J. W.** (1965), Laminar free convection in a vertical slot, *J. Fluid Mech*., 23, 77–98.
7. **Emery A., Chi H., Dale J.** (1971), Free convection through vertical plane layers of non-Newtonian power law fluids, *ASME J. Heat Transfer*, 93, 164–171.
8. **Erturk E., Corke T. C.** (2001), Boundary layer leading-edge receptivity to sound at incidence angles, *Journal of Fluid Mechanics*, 444, 383–407.
9. **Erturk E., Corke T. C., Gökçöl C.** (2005), Numerical solutions of 2-D steady incompressible driven cavity flow at high Reynolds numbers, *J. Numer. Meth. Fluids*, 48, 747–774.
10. **Erturk E., Haddad O. M., Corke T. C.** (2004), Laminar incompressible flow past parabolic bodies at angles of attack, *AIAA Journal*, 42, 2254–2265.
11. **Gebhart B., Jaluria Y., Mahajan R. L., Sammakia B.** (1988), Buoyancy induced flows and transport, *Washington: Hemisphere.*
12. **Ghia U., Ghia K. N., Shin C. T.** (1982), High-Re solutions for incompressible flow using the Navier-Stokes equations and a multigrid method, *J. Comp. Physics*, 48, 387–411.
13. **Gunzburger M. D., Meir A. J., Peterson J. S.** (1991), On the existence, uniqueness and finite element approximation of solutions of the equations of stationary, incompressible magnetohydro-dynamics, *Math. Comput*., 56, 523–563.
14. **Hasler U., Schneebeli A., Schötzau D.** (2004), Mixed finite element approximation of incompressible MHD problems based on weighted regularization, *Appl. Numer. Math*., 51, 19–45.
15. **He Y. N., Li, J.** (2009), Convergence of three iterative methods based on the finite element discretization for the stationary Navier-Stokes equations, *Comput. Methods Appl. Mech. Engrg.,* 198, 1351–1359.
16. **Hou S., Zou Q., Chen S., Doolen G., Cogley A.C.** (1995), Simulation of cavity flow by the Lattice Boltzmann method, *J. Comp. Physics*, 118, 329–347.
17. **Khader M. M.** (2016), Shifted Legendre Collocation method for the flow and heat transfer due to a stretching sheet embedded in a porous medium with variable thickness, variable thermal conductivity and thermal radiation, *Mediterr. J. Math*., 13, 2319–2336.
18. **Liao S. J., Zhu J. M.** (1996), A short note on higher-order stream function-vorticity formulation of 2-D steady state Navier-Stokes equations*, Int. J. Numer. Methods Fluids*, 22, 1–9.
19. **Rayleigh R.** (1916), On convection currents in a horizontal layer of fluid, when the higher temperature is on the underside, *Phil. Mag., Ser.6*, 32, 529–546.
20. **Rubin S. G., Khosla P. K**. (1981), N-S calculations with a coupled strongly implicit method, *Computers and Fluids,* 9, 163–180.
21. **Rudraiah N., Barron R. M., Venkatachalappa M., Subbaraya C. K.** (1995), Effect of a magnetic field on free convection in a rectangular enclosure*, Int. J. Engng Sci.,* 33, 1075–1084.
22. **Salah N. B., Soulaimani A., Habashi W. G.** (2001), A finite element method for magnetohydrodynamics, *Comput. Methods Appl. Mech. Engrg.,* 190, 5867–5892.
23. **Schreiber R., Keller H. B.** (1983), Driven cavity flows by efficient numerical techniques, *J. Comp. Physics*, 49, 310–333.
24. **Shenoy A. V.** (1988), *Natural convection heat transfer to viscoelastic fluids*, Houston: Gulf.
25. **Siddheshwar P. G., Ramachandramurthy V., Uma D.** (2011), Rayleigh-Benard and Marangoni magnetoconvection in Newtonian liquid with thermorheological effects, *Int. J. Engng Sci.,* 49, 1078–1094.
26. **Siginer D. A., Valenzuela-Rendon A.** (1994), Natural convection of viscoelastic liquids, *Proc. ASME Fluids Engineering Division Summer Meeting, Symposium, ASME FED*, 179, 31–41.
27. **Smith G. D.** (1978), *Numerical solution of partial differential equations by finite difference methods,* Oxford University Pres.
28. **Tennehill J. C., Anderson D. A., Pletcher R. H.** (1997), *Computational fluid mechanics and heat transfer*, Taylor& Francis.
29. **Venkatachalappa M., Younghae D., Sankar M.** (2011), Effect of magnetic field on the heat and mass transfer in a vertical annulus, *Int. J. Engng Sci.,* 49, 262–278.
30. **Wilkes J. O., Churehill S. W.** (1966), The finite-difference computation of natural convection in a rectangular enclosure, *AICHEJ,* 12, 161–166.
31. **Xu H., He Y. N.** (2013), Some iterative finite element methods for steady Navier-Stokes equations with different viscosities, *J. Comput. Phys.*, 232, 136–152.

DOI 10.2478/ama-2019-0005

STATIC ELECTROMECHANICAL CHARACTERISTICS OF PIEZOELECTRIC CONVERTERS WITH VARIOUS THICKNESS AND LENGTH OF PIEZOELECTRIC LAYERS

Grzegorz MIECZKOWSKI*

*Faculty of Mechanical Engineering, Białystok University of Technology, ul. Wiejska 45C, 15-351 Białystok, Poland

g.mieczkowski@pb.edu.pl

received 10 July 2018, revised 10 March 2019, accepted 15 March 2019

Abstract: The paper presents the analysis of electromechanical characteristics of piezoelectric converters subjected to an electric field and mechanical load. The analyses were performed based on a method consisting implementation of special segments responsible for electrical boundary conditions to a homogeneous beam. Constitutive equations were developed, allowing one to obtain static electromechanical characteristics for piezoelectric actuators with freely defined boundary conditions and geometry. Moreover, based on constitutive equations obtained, a particular solution for cantilever transducer subjected to concentrated force has been developed. The resulting analytical solution was compared with the data available in the literature, and the developed FEM solution. Furthermore, the influence of factors such as relative length, thickness and location of particular piezoelectric layers on electromechanical characteristics of the transducer was defined.

Key words: Piezoelectric bender, constitutive equations, deflection, electromechanical characteristics

1. INTRODUCTION

Today piezoelectric transducers are applied in many different industries (Tzou, 1999; Przybyłowicz, 1999; Liu et al., 2014, Szpica et al., 2018). They are used as measuring and controlling elements in, more or less complex, systems for working process execution. Design of a transducer depends on its manufacturing method and intended use. Normally, they are made of one or more piezoelectric layers (with electrodes placed on their entire length) and a non-piezoelectric component. Their working principle is based on the conversion of electric energy to mechanical, or vice versa (Busch-Vishniac, 1999). Electromechanical characteristics – relation between deflection of a transducer and applied electrical and mechanical loads, is defined based on constitutive equations. These equations bound together geometrical properties, material properties and physical parameters, such as force, displacement and electric field. Developing and solving of such simultaneous equations, in case of piezoelectric benders, is very difficult. Material and geometrical heterogeneity of the global structure of bender and diverse boundary conditions force the use of some reductions.

Electromechanical characteristics of piezoelectric transducers were dealt with by many scientists. Smits et al. (1991), by using energetic methods, formed and solved physical equations for a transducer made of two layers of even length (piezoelectric bimorph). Then Wang and Cross (1999) extended and solved the issue of a triple segment, while Xiang and Shi (2008) – a multilayer one. In papers (Park and Moon, 2005; Dunsch and Breguet, 2008; Rahmoune and Osmont, 2010; Raeisifard et al., 2014, Mieczkowski, 2016, Nguyen et al., 2018), results of piezoelectric bimorph testing were given, wherein their design featured piezoelectric layer of length other than that of a non-piezoelectric component. The paper (Mieczkowski, 2017) analysed static and dynamic characteristics of a three-layer actuator, made of a non-piezoelectric component and two piezoelectric layers of the same length and thickness. Durability and utility features of piezoelectric transducer were analysed in paper (Mieczkowski, 2018).

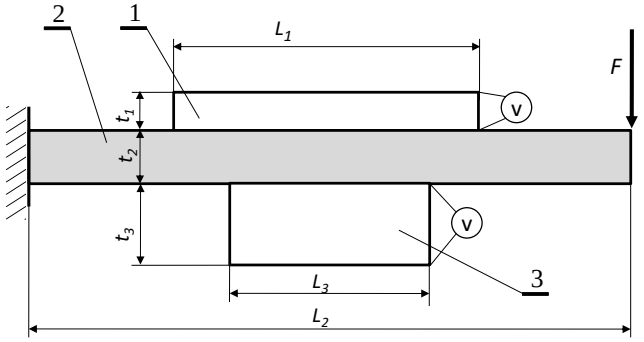

Fig. 1. Three-layer piezoelectric converter; 1,3 – piezoelectric elements, 2 – beam

The paper presents tests performed in a way similar to those given in the paper (Mieczkowski, 2017), extending them by a possibility to include, within constitutive equations, the diversity of thickness and length of particular piezoelectric layers (Fig. 1).

The other objective of researching was to determine the influence of relative thickness, length and location of particular piezoelectric layers on electromechanical characteristics of transducers. Therefore, based on the constitutive equations defined, a particular solution for cantilever transducer (subjected to concentrated force) was developed and necessary analyses were made allowing one to determine the influence of the above parameters on its electromechanical characteristics.

DOI 10.2478/ama-2019-0005

2. CONSTITUTIVE EQUATIONS

2.1. Basic assumptions

To define constitutive equations, the method (described in detail in papers [Mieczkowski, 2016; Mieczkowski, 2017]), which allows for implementation to a homogeneous beam two types of modules, hereinafter referred to as PBS (piezoelectric bimorph segment) and PTS (piezoelectric triple segment) was used. This allows for including in electromechanical characteristics of the segment a local change in stiffness and strain, which are caused by the transverse piezoelectric effect (Curie et al., 1880). In order to reduce the mathematical model, the following assumptions were made:

a) bending of the element takes place according to the Euler's hypothesis, and radii of curvature of the deflected components are identical
b) in connection plane of piezoelectric and non-piezoelectric components, there is no intermediate layer (the presence of adhesive layers and electrodes on the bottom and top surface of the piezoelectric material is omitted), and no sliding occurs,
c) in piezoelectric layers, transverse piezoelectric effect 1–3 takes place, causing pure bending.

2.2. General equation for strain of piezoelectric triple segment

Fragment of three-layer piezoelectric converter, as given in Fig. 2, shall now be examined. In the structure of the transducer, two piezoelectric components (of different thickness and length) and a non-piezoelectric element can be distinguished. Moment *M(x)* is induced by mechanical operating load. Its value and distribution is also dependant on boundary conditions related to the mounting of the converter. In the bender, also electrical load M_{ei} will occur, caused by piezoelectric effect (present in piezoelectric components).

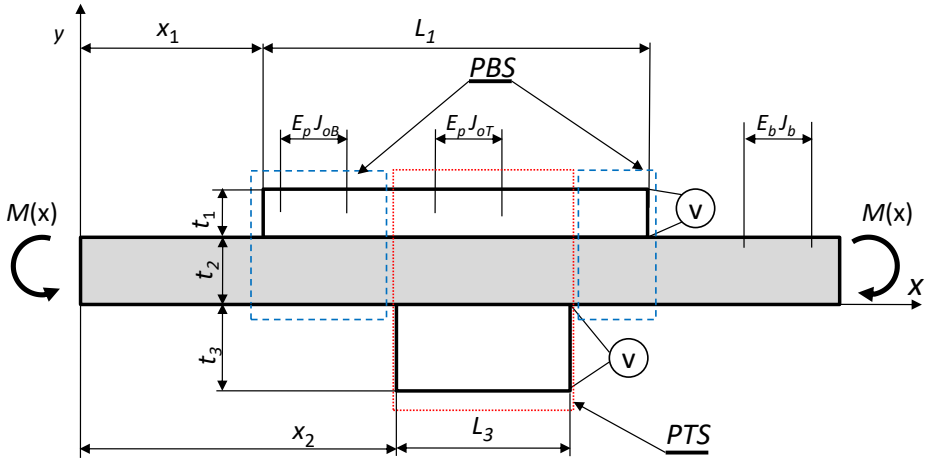

Fig. 2. Fragment of three-layer piezoelectric converter

In the analysed structure, subjected to bending, it is possible to determine the five characteristic ranges, related to a change in load and stiffness. Within the $x_1<x<x_2$ and $x_2+L_3<x<x_1+L_1$ ranges, there is a piezoelectric bimorph segment *PBS* (generating electric moment M_{eB}) with flexural stiffness E_pJ_{oB}. Between the *PBS* segments (the $x_2<x<x_2+L_3$ segment), there is piezoelectric triple segment *PTS*, which generates electric moment M_{eT} and has flexural stiffness E_pJ_{oT}. The other two ranges are within the homogeneous beam with stiffness E_bJ_b.

Taking into account the above structural variability and load conditions, general differential equation for strain of bender can be noted as follows:

$$\frac{\partial^2 y}{\partial x^2} = M_{eB}\,\gamma_B \begin{pmatrix}(H[x-x_1]-H[x-x_2])+\\ +(H[x-(x_2+L_3)]-H[x-(x_1+L_1)])\end{pmatrix} + \\ +M_{eT}\,\gamma_T(H[x-x_2]-H[x-(x_2+L_3)]) + M(x)/\mathrm{E_bJ_b} \quad (1)$$

where: $H[x-x_i]$ – Heaviside function,
$\gamma_B = \frac{E_bJ_b(M_{eB}+M(x))-E_pJ_{oB}M(x)}{E_bJ_bE_pJ_{oB}M_{eB}}\gamma_T = \frac{E_bJ_b(M_{eT}+M(x))-E_pJ_{oT}M(x)}{E_bJ_bE_pJ_{oT}M_{eT}}$ – factors including change in stiffness with applied formal notation of the Heaviside function, E_p, E_b – Young's modules of piezoelectric and non-piezoelectric element, J_b, J_{oB}, J_{oT} – moments of inertia (described hereinafter).

As the determining of the mechanical moment $M(x)$ in general does not pose any problems, determining electric load Mei, generated by piezoelectric segments, is very burdensome and requires solving the two-dimensional problem of bending the multilayer structure, while taking piezoelectric effect into account.

2.3. Electric load M_{ei} generated by piezoelectric segments

2.3.1. Piezoelectric triple segment *PTS*

Three-layer structure of piezoelectric triple segment *PTS* (Fig. 3), with constant width *b*, made of two piezoelectric components (1) and (3) and a non-piezoelectric element (2), shall now be investigated.

The *PTS* is not subjected to any mechanical load, and longitudinal forces N_i and bending moments M_i occurring on individual layers are the result of the applied voltage V. Based on the equilibrium equation of forces condition, the following can be noted:

$$N_1 + N_2 + N_3 = 0. \quad (2)$$

The sum of moments in relation to interface must be zero, therefore:

$$M_1 + M_2 + M_3 - \frac{N_2t_2}{2} - N_3\left(t_2+\frac{t_3}{2}\right) + \frac{N_1t_1}{2} = 0. \quad (3)$$

According to the adopted Euler's hypothesis, bending moments can be notified as follows:

$$\begin{cases} M_1 = \frac{E_p J_{p1}}{\rho} \\ M_2 = \frac{E_b J_b}{\rho} \\ M_3 = \frac{E_p J_{p3}}{\rho} \end{cases}. \quad (4)$$

Substituting relations (4) to (3) and providing simple mathematical transformations resulted in the following:

$$\frac{1}{\rho} = \frac{(N_2+2N_3)t_2 - N_1 t_1 + N_3 t_3}{2(E_b J_b + E_p J_{p1} + E_p J_{p3})}. \quad (5)$$

Including the relation between radius of curvature ρ and deflection $w(x)$:

$$\frac{1}{\rho} = \frac{\partial^2 w}{\partial x^2}, \quad (6)$$

differential equation for bending of converter can be notified as follows:

$$\frac{\partial^2 w}{\partial x^2} = \frac{(N_2+2N_3)t_2 - N_1 t_1 + N_3 t_3}{2(E_b J_b + E_p J_{p1} + E_p J_{p3})} \quad (7)$$

Constitutive equations for lower and upper converter layers, including the piezoelectric effect in layers 1 and 3 gave the following:

$$\begin{cases} \frac{\partial u_{x1}}{\partial x} = \frac{N_1}{E_p A_{p1}} - d_{31}\left(\frac{-V}{t_1}\right) \\ \frac{\partial u_{x2}}{\partial x} = \frac{N_2}{E_b A_b} \\ \frac{\partial u_{x3}}{\partial x} = \frac{N_3}{E_p A_{p3}} + d_{31}\left(\frac{-V}{t_3}\right) \end{cases}, \quad (8)$$

where: A_b, A_{p1}, A_{p3} – layers cross sectional areas, d_{31} – piezoelectric constant.

Following the displacement continuity condition (Fig. 3), it was found that:

$$\begin{cases} u_{x1} - u_{x2} - \frac{\partial w}{\partial x}\left(\frac{t_1}{2} + \frac{t_2}{2}\right) = 0 \\ u_{x1} - u_{x3} - \frac{\partial w}{\partial x}\left(\frac{t_1}{2} + \frac{t_3}{2} + t_2\right) = 0 \end{cases}. \quad (9)$$

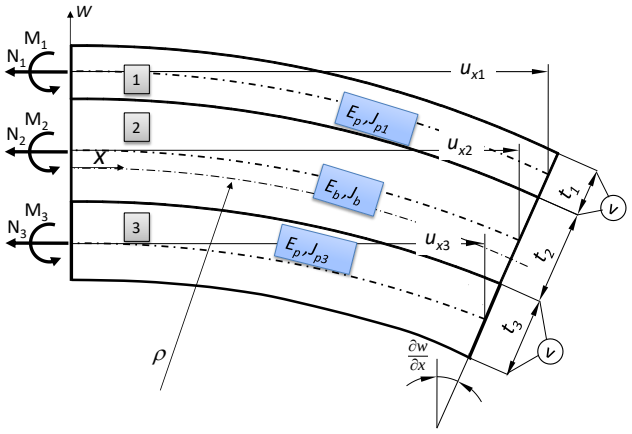

Fig. 3. Distribution of forces and conditions for strain of piezoelectric triple segment *PTS*

Solving of differential equations (7) and (8), with the following boundary conditions:

$$\begin{cases} \frac{\partial w}{\partial x}(0) = 0, w(0) = 0 \\ u_{x1}(0) = 0, u_{x2}(0) = 0, u_{x3}(0) = 0 \end{cases}, \quad (10)$$

and by applying relation (9), longitudinal force N_i can be determined:

$$\begin{cases} N_1 = -\frac{bd_{31}E_p V(\alpha_3 + E_b E_p t_2(t_1^3 + t_2^2(4t_1 - 2t_3) + 3t_1^2 t_3 - 2t_3^3 + 3t_2(t_1 - t_3)(t_1 + 2t_3)))}{\alpha_1 + \alpha_2} \\ N_2 = -\frac{-3bd_{31}E_b E_p^2 V t_2(t_1 - t_3)(t_2 + t_1 + t_3)(2t_2 + t_1 + t_3)}{\alpha_1 + \alpha_2} \\ N_3 = \frac{bd_{31}E_p V(\alpha_3 + E_b E_p t_2(-2t_1(t_2^2 + 3t_2 t_1 + t_1^2) + t_2(4t_2 + 3t_1)t_3 + 3(t_2 + t_1)t_3^2 + t_1^3))}{\alpha_1 + \alpha_2} \end{cases} \quad (11)$$

where: $\alpha_1 = E_b^2 t_2^4 - 2E_b E_p t_2(t_1^3 + t_3^3 + t_2^2(t_1 + t_3) + 3t_2(t_1^2 + t_3^2))$, $\alpha_2 = E_p^2(t_1^4 - 2t_1^3 t_3 + t_3^4 - 6t_1^2 t_3(2t_2 + t_3) - 2t_1 t_3(6t_2^2 + 6t_2 t_3 + t_3^2)$, $\alpha_3 = E_b^2 t_2^4 + E_p^2(t_1^4 + t_1^3 t_3 + t_1 t_3^3 + t_3^4)$.

The differential equation for bending of *PTS*, in the M_{eT} moment function, can be notified as follows:

$$\frac{\partial^2 w}{\partial x^2} = \frac{-M_{eT}(1 + \frac{t_2}{t_1 + t_3})}{E_p J_{oT}}. \quad (12)$$

Basing on the comparison of relations (7) and (12), it is possible to determine the bending moment M_{eT}, which is the result of the piezoelectric effect:

$$M_{eT} = \frac{E_p J_{oT}(t_1 + t_3)(N_1 t_1 - N_2 t_2 - 2N_3 t_2 - N_3 t_3)}{2(E_b J_b + E_p J_{p1} + E_p J_{p3})(t_1 + t_2 + t_3)}. \quad (13)$$

The required moment, taking relation (11) into account, can be noted as follows:

$$M_{eT} = d_{31} E_p^2 V \theta, \quad (14)$$

where:

$$\theta = \frac{-b\, J_{oT}(t_1 + t_3)(t_1 + 2t_2 + t_3)\left(E_b t_2 + E_p(t_1 + t_3)\right)\left(E_b t_2^3 + E_p(t_1^3 + t_3^3)\right)}{2(E_b J_b + E_p J_{p1} + E_p J_{p3})(t_1 + t_2 + t_3)(\alpha_1 + \alpha_2)}.$$

Moments of inertia for particular layers are, respectively:

$$J_b = \frac{bt_2^3}{12}, J_{p1} = \frac{bt_1^3}{12}, J_{p3} = \frac{bt_3^3}{12}. \quad (15)$$

The averaging value of the moment of inertia JoT (16) – calculated in relation to the neutral layer – was determined in the same way as in the paper (Mieczkowski, 2016), using the method of transformation of the cross sectional area (Fertis, 1996).

$$J_{oT} = \frac{b(\alpha_1 + \alpha_2 + \alpha_4)}{12E_p(E_b t_2 + E_p(t_1 + t_3))},$$
$$\alpha_4 = 6E_p(E_p t_1 t_3(t_1 + 2t_2 + t_3)^2 + E_b t_2(t_1^3 + 2t_1^2 t_2 + t_1 t_2^2 + t_3(t_2 + t_3)^2)) \quad (16)$$

2.3.2. Piezoelectric bimorph segment *PBS*

Solution for the issue of piezoelectric bimorph segment is provided in the paper (Mieczkowski, 2016). Below are the relations describing electric load (17) generated by the *PBS* and the averaging value of the moment of inertia (18).

$$M_{eB} = d_{31}{E_p}^2 V\beta, \tag{17}$$

$$J_{oB} = \frac{b\beta_2}{12E_p(E_b t_2 + E_p t_1)}, \tag{18}$$

where: $\beta = \frac{6E_b J_{oB} t_2(t_2+t_1)}{\beta_2}, \beta_2 = {E_b}^2 t_2^4 + {E_p}^2 t_2^4 + 2E_b E_p t_2 t_1(2t_2^2 + 3t_2 t_1 + t_1^2)$.

2.4. Electromechanical characteristics of cantilever transducer subjected to concentrated force *F*

This part of the paper is concerned with the application of the proposed method, based on implementing the *PBS* and *PTS* segments to a homogeneous beam so as to determine the analytical relations describing the deflection of the transducer with fixed geometry and known boundary conditions.

In the transducer, as shown on Fig. 4, the left side is fixed-mounted, and the right can move freely. The operational load results from the external force *F* and electric moments M_{ei} generated by the applied voltage V. Based on the conditions for equilibrium of forces and moments, values for the reaction in mounting were established, and are as follows: $R_y = \mathrm{F}, R_x = 0, M_F = FL$.

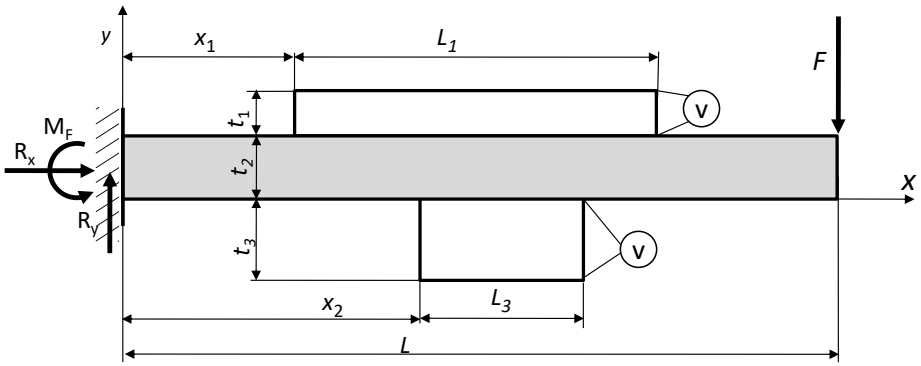

Fig. 4. Cantilever transducer with *PBS* and *PTS* segments

Therefore, mechanical moment *M*(*x*) takes the following form:

$$M(x) = -M_F + R_y x = -FL + Fx. \tag{19}$$

Substituting relations (14), (17) and (19) to the general solution, described by the formula (1), upon double integration, gives a relation that describes deflection of the analysed bender (20):

$$y(x) = \frac{1}{6E_b E_p J_b J_{oB} J_{oT}}(A_1 v + B_1 F), \tag{20}$$

where:

$$A_1 = 3E_b d_{31} E_p^2 J_b + \{\beta J_{oT} H[x-x_1](x-x_1)^2 - (\beta J_{oT} - \theta J_{oB})(H[x-x_2](x-x_2)^2 + x(L_3+x_2)^2) + H[x-L_3-x_2](L_3-x+x_2)^2 - \beta J_{oT} H[x-L_1-x_1](L_1-x+x_1)^2\},$$

$$B_1 = J_{oT}(E_p J_{oB} - E_b J_b)(H[x-x_1](x-x_1)^2(3L-x-2x_1) - H[x-x_1-L_1](3L-2L_1-x-2x_1)(L_1-x+x_1)^2) + E_p J_{oB} J_{oT} x^2(x-3L) + (J_{oB} - J_{oT}) E_b J_b \begin{pmatrix} -H[x-x_2](x-x_2)^2(3L-x-2x_2) + (2(L_3+x_2)-3L)(L_3+x_2)^2 x \\ +H[x-x_2-L_3](3L-2L_3-x-2x_2)(L_3-x+x_2)^2 \end{pmatrix}.$$

Integration constants are determined on the basis of the following boundary conditions:

$$\frac{\partial y}{\partial x}(0) = 0, y(0) = 0. \tag{21}$$

It is worth noting that, in the obtained solution (20), assumption of even length ($L_1 = L_3$) and thickness ($t_1 = t_3$) of both piezoelectric layers, results in obtaining the identical solution as the one presented in the paper (Mieczkowski, 2017). In order to determine the electromechanical behaviour of the converter, most frequently, the FEM-based analyses are carried out (Rahmoune and Osmont, 2010, Szpica, 2015, 2018, Borawski, 2015, 2018). Therefore, in order to validate the method developed, a transducer with the following geometry – $L_1 \neq L_3$, $t_1 \neq t_3$ – was modelled following the *FEM* method with the use of the ANSYS application (Mieczkowski, 2016; Documentation for ANSYS, 2010). In the calculations, the following material data were assumed:

- Young's modulus: E_p = 2.0'10^9, E_b = 4.0'10^9, N/m^2
- Poisson's ratio: υ_p = 0.29, υ_b = 0.33
- Piezoelectric strain coefficients: d_{31} = 2.2'10^{-11} C/N, d_{32} = 0.3'10^{-11} C/N, d_{33} = -3.0'10^{-11}C/N
- Relative permittivity at constant stress: $(\varepsilon_{33})^T$ = 12

The difference between analytical and numerical solutions was approx. 1% for electrical load and 3% for mechanical load. The comparison of both solutions is graphically shown in Fig. 5.

The obtained particular solution (20) allowed one to determine the influence of mutual geometric relations of particular components of the bender on its functional characteristics. Two types of converters were analysed:

1. converter with piezoelectric components of different length – $L_1 \neq L_3$ (whereas the upper piezoelectric layer is of the same length as beam element – $L_1 = L$)
2. two piezoelectric layers of the same length – $L_1 = L_3$, $x_1 = x_2$

DOI 10.2478/ama-2019-0005

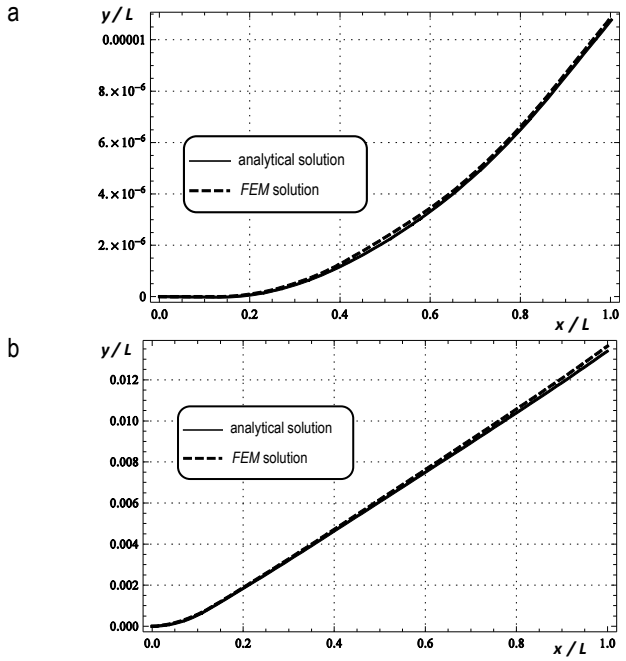

Fig. 5. Deflection of the cantilever converter for x_1 = 0, x_2 = 2/3L, t_1 = 2 mm, t_2 = 1 mm, t_3 = 6 mm, L = 60 mm: a) subjected only to an electrical voltage, V = 100 V, F = 0; b) subjected only to a force, V = 0, F = -10N

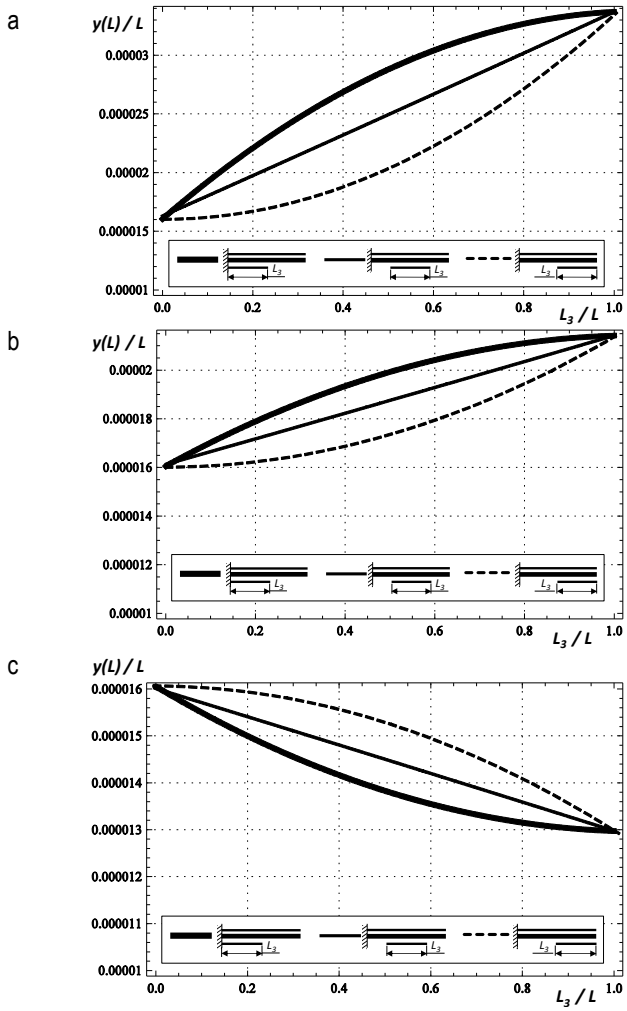

Fig. 6. Influence of location and length of the piezoelectric element on the deflection of the transducer under electric load (v = 100 V, F = 0) only; a) t_1/t_3 = 2, b) t_1/t_3 = 1, c) t_1/t_3 = 0.5

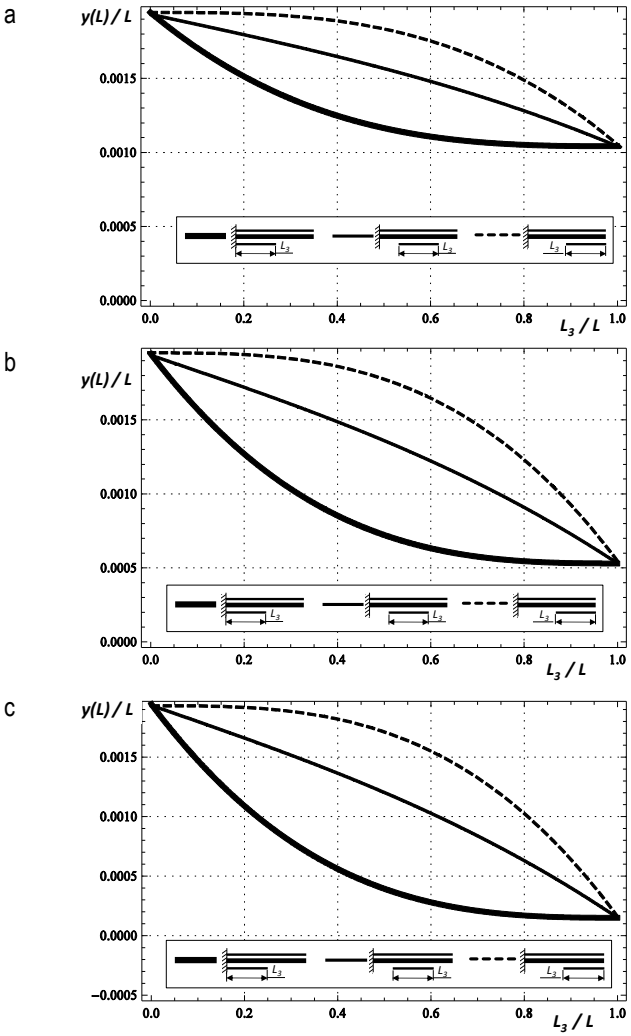

Fig. 7. Influence of location and length of the piezoelectric element on the deflection of the transducer under mechanical load (F = -10 N, V = 0) only; a) t_1/t_3 = 2, b) t_1/t_3 = 1, c) t_1/t_3 = 0.5

For both variants, the influence of the above parameters on the deflection of the right end of the transducer was analysed:

- relative thickness of particular piezoelectric elements t_1/t_3
- relative length of components $L_{1,3}/L$
- locations of piezoelectric components (*PTS* segment: at the left of the converter -x_2 = 0, in the middle - $x_2 + L_3/2 = L/2$, at the right - $x_2 + L_3 = L$)

In the analysis performed, the following material and geometric data were included: E_p = 2.0'10^9 N/m^2, E_b = 4.0'10^9 N/m^2, d_{31} = 2.2'10^{-11} C/N, L = *60* mm, t_2 = 1 mm.

The below figures show a graphical representation of the results of tests carried out for the converter with different length of piezoelectric components, subjected to electric moment (Fig. 6) and mechanical load (Fig. 7).

Based on the obtained results (Fig. 6), it can be claimed that when subjecting the element to electric moment only, displacement of the right end of the transducer:

- is increased with the increase in relative thickness of the layers t_1/t_3
- is increased with the increase in relative length L_3/L in case of $t_1/t_3 \geq 1$

- is decreased with the increase in relative length L_3/L in case of $t_1/t_3 < 1$
- has the highest value, when the piezoelectric segment is located at the left in case of $t_1/t_3 \geq 1$
- has higher values ($L_3 \neq 0$, $L_3 \neq L$), when the piezoelectric segment is located at the right in case of $t_1/t_3 < 1$

As expected, when applying mechanical load only (Fig. 7), the increase in relative thickness of layers t_1/t_3 causes the increase in the deflection of the transducer. The biggest displacement is achieved, when the piezoelectric segment is located at the right of the transducer. Noticeable also is the decrease in displacement value along with the increase in the L_3/L parameter value.

The results of analyses for the transducer with piezoelectric layers of the same length ($L_1 = L_3$, $x_1 = x_2$), are given in Fig. 8. Due to the fact that when applying mechanical load, the influence of the considered factors (relative thickness, length and location of piezoelectric layers) on electromechanical characteristics was identical as in the case of the converter with different lengths of piezoelectric components, the results obtained only for electric load are given.

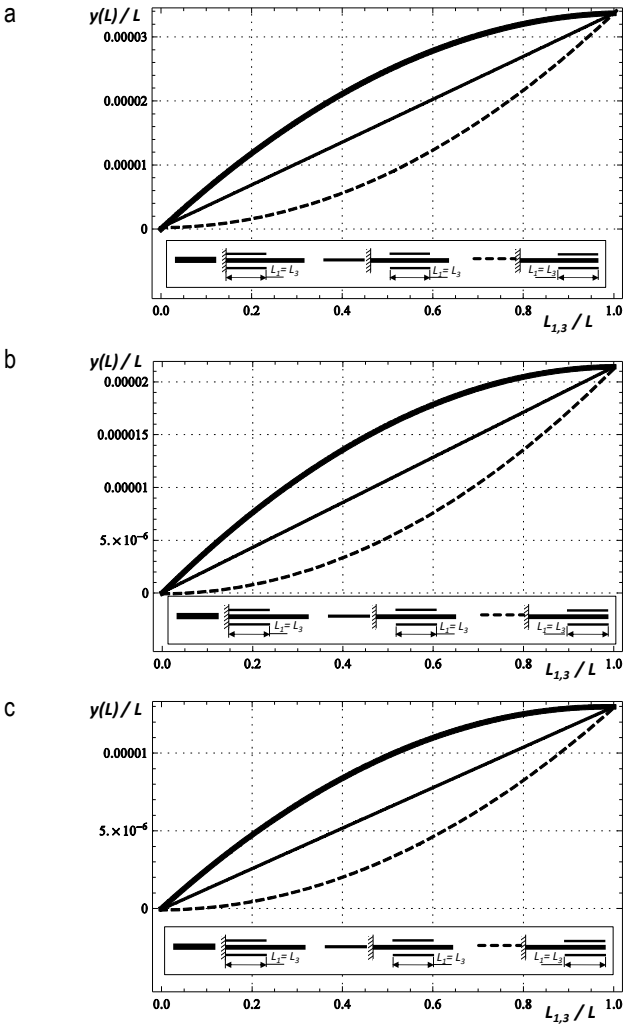

Fig. 8. Influence of location and length of the piezoelectric element on the deflection of the transducer – with the same length of piezoelectric components – under electric load (v = 100 V, F = 0) only; a) $t_1/t_3 = 2$, b) $t_1/t_3 = 1$, c) $t_1/t_3 = 0.5$

Analysing the obtained results, as given in Fig. 8, it can be claimed that displacement of the right end of the transducer increases with the increase in relative thickness (t_1/t_3) and length ($L_{1,3}/L$) of piezoelectric layers. The highest values of relocation are obtained when piezoelectric segment is located at the left.

3. CONCLUSIONS

Based on the testing performed, it can be noted that:

- the obtained solution for cantilever transducer, assuming the same length and thickness of piezoelectric layers, is compatible with the solution provided in paper (Mieczkowski, 2017)
- analytical solutions conform to the results obtained from the *FEM* (for electric load, the difference is about 1%, and for mechanical load – 3%)

As for the electromechanical characteristics of the cantilever transducer, it was found that the following factors have significant influence on the conditions of strain of the transducer:

- relative thickness of particular piezoelectric elements t_1/t_3
- relative length of components $L_{1,3}/L$
- locations of piezoelectric components

For transducer with different length of piezoelectric layers, displacement of the end of the transducer is increased with the increase in relative thickness of the layers t_1/t_3. Increase in relative length L_3/L results in:

a) when applying electric load:
   - increase in displacement $y(L)$, if $t_1/t_3 \geq 1$
   - decrease in displacement $y(L)$, if $t_1/t_3 < 1$
b) when applying mechanical load:
   - decrease in displacement

The biggest relocation ($L_3 \neq 0$, $L_3 \neq L$) is achieved when piezoelectric segment is located:

a) when applying electric load:
   - at the left in case of $t_1/t_3 \geq 1$
   - at the right in case of $t_1/t_3 < 1$
b) when applying mechanical load:
   - at the right of the transducer

Analysing the issue of the transducer with uniform length of piezoelectric layers, it was found that:

a) for applying mechanical load, the influence of the considered factors on electromechanical characteristics was identical to the case of the transducer with different lengths of piezoelectric components
b) when applying electric load (induced by the voltage V):
   - deflection of the right end of the transducer is increased with the increase in relative thickness (t_1/t_3) and length ($L_{1,3}/L$) of piezoelectric layers
   - the highest values of displacement are achieved in the case when piezoelectric segment is located at the left

It is therefore concluded that the utility features of the piezoelectric transducers are significantly influenced by their geometrical properties. The increase in thickness and length of piezoelectric layers increases the flexural stiffness and the generated moment M. The increase in stiffness results in a decrease in converter deflection. However, the increase in the moment increases its deflection. Therefore, by choosing the location, thickness and length of the piezoelectric components properly, a compromise solution can be obtained, ensuring the greatest deflection of the

transducer. Analytical solutions describing deformations of piezoelectric transducers may be helpful in this.

REFERENCES

1. **Borawski A.** (2015), Modification of a fourth generation LPG installation improving the power supply to a spark ignition engine, *Eksploatacja i Niezawodnosc* (*Maintenance and Reliability*), 17(1), 1–6.
2. **Borawski A. (**2018), Simulation study of the process of friction in the working elements of a car braking system at different degrees of wear, *Acta Mechanica et Automatica*,12(3), 221–226.
3. **Busch-Vishniac I.J.** (1999), *Electromechanical Sensors and Actuators*, Springer-Verlag.
4. **Curie P.J., Curie J.** (1880), *Crystal Physics-Development by Pressure 0/ Polar Electricity in Hemihedral Crystals with Inclined Faces*, Acad. Sci.(Paris) C. R. Hebd. Seances, 91, 294 (in French).
5. **Documentation for ANSYS, Coupled-Field Analysis Guide** (2010).
6. **Dunsch R., Breguet J.M. (**2006), Unified mechanical approach to piezoelectric bender modelling, *Sens. Actu.* 134, 2, 436–446.
7. **Fertis D.G.** (1996), *Advanced Mechanics of Structures*, Marcel Dekker, New York.
8. **Liu X., Wang X., Zhao H., Du Y.** (2014), Myocardial cell pattern on piezoelectric nanofiber mats for energy harvesting, J. *Phys: Conf. Ser*. 557, 1–5.
9. **Mieczkowski G.** (2016), Electromechanical characteristics of piezoelectric converters with freely defined boundary conditions and geometry, *Mechanika*, 22(4), 265–272.
10. **Mieczkowski G.** (2017), The constituent equations of piezoelectric cantilevered three-layer actuators with various external loads and geometry, *Journal of Theoretical and Applied Mechanics*, 55(1), 69–86.
11. **Mieczkowski G.** (2018), Optimization and Prediction of Durability and Utility Features of Three-Layer Piezoelectric Transducers, *Mechanika*, 24(3), 335–342.
12. **Nguyeni V-T., Kumar P., Leong J.Y.C.** (2018), Finite Element Modelling and Simulations of Piezoelectric Actuators Responses with Uncertainty Quantification, *Computation,* 6(4), 1–20.
13. **Park J.K., Moon W.K.** (2005), Constitutive relations for piezoelectric benders under various boundary conditions, *Sens. Actuat. A*, 117, 159–167.
14. **Przybyłowicz P.M.** (1999), Application of piezoelectric elements to semi-adaptive dynamic eleminator of torsional vibration, *Journal of Theoretical and Applied Mechanics*, 37, 2, 319-334.
15. **Puławski G., Szpica D.** (2015), The modelling of operation of the compression ignition engine powered with diesel fuel with LPG admixture, *Mechanika*, 21(6), 501-506.
16. **Raeisifard H. Bahrami M.N. Yousefi-Koma A., Fard H. R.** (2014), Static characterization and pull-in voltage of a micro-switch under both electrostatic and piezoelectric excitations, *European Journal of Mechanics A/Solids*, 44, 116-124.
17. **Rahmoune M., Osmont D.** (2010), Classic finite elements for simulation of piezoelectric smart structures, *Mechanika*, 86(6), 50-57.
18. **Smits J.G., Dalke S.I., Cooney T.K.** (1991), The constituent equations of piezoelectric bimorphs, *Sensors and Actuators A*, 28, 41–61.
19. **Ştefănescu D. M.** (2011), Piezoelectric Force Transducers (PZFTs), *Handbook of Force Transducers*, 109-130.
20. **Szpica D.** (2018), Modeling of the operation of a Dual Mass Flywheel (DMF) for different engine-related distortions, *Mathematical and Computer Modelling of Dynamical Systems*, 24(6), 643-660.
21. **Szpica D., Borawski A., Mieczkowski G.** (2018), New Concept of Low-Pressure Gas-Phase Injector, *Proceedings of the 23nd International Scientific Conference*, 173-176.
22. **Tzou H.S.** (1999), *Piezoelectric Shells: Distributed Sensing and Control of Continua*, Kluwer Academic Publishers, Dordrecht.
23. **Wang Q., Cross L.E**. (1999), Constitutive equations of symmetrical triple-layer piezoelectric benders, *IEEE Trans. Ultrason. Ferroelec.Freq. Contr.*, 46, 1343–1351.
24. **Xiang H.J., Shi Z.F**. (2008), Static analysis for multi-layered piezoelectric cantilevers, *International Journal Of Solids And Structures*, 45(1), 113-128.

Studies were carried out within work no. S/WM/1/18 and funded from under development of science by Ministry of Science and Higher Education.

sciendo

DOI 10.2478/ama-2019-0006

acta mechanica et automatica, vol.13 no.1 (2019)

DESIGN OF THE VIBROSTABILISATION STAND FOR REDUCING RESIDUAL STRESSES IN DISCS USED IN THE CONSTRUCTION OF MULTI-PLATE CLUTCHES AND BRAKES

Jerzy JAROSZEWICZ*, Krzysztof ŁUKASZEWICZ*, Vladimir ANTONYUK**

*Faculty of Engineering Management, Bialystok University of Technology, ul. Ojca Tarasiuka 2, 16-001 Kleosin, Poland
**Joint Institute of Mechanical Engineering of the NAS of Belarus, 12 Akademicheskaya Street, 220072, Minsk, Republic of Belarus

j.jaroszewicz@pb.edu.pl, k.lukaszewicz@pb.edu.pl, vladi@tut.by

received 17 March 2018, revised 12 March 2019, accepted 18 March 2019

Abstract: Heavy-duty, oil-cooled brake discs (MMOTs) are often used in heavy-duty brake systems manufactured by companies such as Caterpilar, Clark, Komatsu and Liebherr. These discs are usually made of special steels, and in most cases, the flatness of the working surfaces should not exceed 0.15–0.30 mm. Although the technological processes of friction disc production include several stages of heat treatment and grinding, the required accuracy is not achieved in some cases. In addition, the remaining residual stresses lead to the deformation of the discs during their lifetime. In production practice, three methods are used to reduce residual stresses: thermo-fixing, dynamic stabilisation and vibratory stabilisation consisting in bringing discs to transverse resonance vibrations and maintaining resonance until significant stress reduction. The article proposes a method of stabilising the discs using the resonance phenomenon at the first few frequencies. In this article, Cauchy's function method and characteristic series method are used to develop solution value problem for clamped circular plates with discrete inclusions as concentrated masses and springs. Calculation methods for quick estimation of the own frequency of discs with additional ring mass enabling the use of low power vibration inductors are presented. The use of a special membrane and a pneumatic cushion in the construction of the stand allows to induce vibrations of higher frequencies.

Key words: Heavy Vehicles, Friction Discs, Multi-Disc Brake, Vibratory Stabilisation

1. INTRODUCTION

Brake and clutch discs have the form of thin rings sensitive to permanent deformations arising as a result of mechanical treatment and, above all, thermal treatment. In order to exclude undesirable phenomena resulting from the surface-heat treatment, various technological measures are applied, which, in most cases, consist in subjecting the elements to static loads. However, these treatments do not completely eliminate internal stresses and thus do not guarantee a stable element geometry for a longer period.

Residual stress is a stress existing and balancing within the material after cessation of interactions causing its formation. They arise practically with all technological processes of heat treatment, mechanical treatment, pressure treatment and many other types of machining. The causes of residual stress are diverse (heterogeneity of plastic deformation, non-uniformity of the temperature field and phase transformations). In real polycrystalline material, internal stresses can be divided into three types (Rossini et al., 2012; Salvati and Korsunsky, 2017):

- stresses type 1 – they balance themselves within the whole structure of a part (if such an element is cut into pieces, its parts will not match because of their deformation after the release of stresses);
- stresses type 2 (intercrystalline or interphase stresses) – they balance within the polycrystal, also known as structural stresses;
- stresses type 3 – arise inside the crystal, for example, around dislocations within crystals.

Regardless of the type of occurring stresses, their action always causes elastic deformation of the crystal lattice. It can be noticed that internal stresses play a significant role in the process of deformation and initiation of microdamage (Almer et al., 2000; Meng et al., 2017; Mughrabi, 2013; Pedrosa et al., 2011; Sangid, 2013). It is believed that the direct cause of internal stresses in the polycrystalline body is the geometric incompatibility of the deformation caused by the anisotropy of the mechanical properties of individual crystals. In polycrystalline materials, this generates a heterogeneous state of plastic deformation. Plastic deformation running at finite speed causes an increase in the microdamage of the structure. Material, because of the distortion of the crystal lattice, becomes structurally unstable. Return to a more permanent state proceeds spontaneously. Internal stresses and distortion of the crystal lattice are interdependent. It is believed that in metallic materials, internal stresses are the result of elastic deformation of the crystal lattice. If favourable conditions occur, elastic defects of the structure relax and internal stresses disappear (Adamczyk, 1993; Wesołowski, 1981), relaxation of elastic defects of the structure causes a decrease in deformation strengthening and, in many cases, leads to irreversible deformation (Salvati and Korsunsky, 2017). At present, there are many experimental methods for determining residual stresses, classification of which can be found, for example, in Ghasri-Khouzani (2017), Hałas (2010), Khan and Gangele (2016), Schajer (2013), and Vourna et al. (2015). This work presents a proposal for methods to improve the geometrical parameters of brake friction discs, in particular flatness deviations by using a cyclic load with variable amplitude, thermo-fixing and vibration stabilisation, complementing the technological process of disc manufacture. The basis of first these methods is a proven theory (Antonyuk, 2004; Antonyuk et al.,

2016) that cyclic loading of elements, carried out under specific conditions, affects the stabilisation of mechanical properties and the effect of relaxation of residual stresses.

The aim of this work is to design the stand for effective reduction of residual stress, using the vibration method, in clutch discs and brakes of multi-plate heavy-duty vehicles.

2. BRAKE DISCS TECHNOLOGICAL PROCESS

In brake systems of modern heavy-duty vehicles used in open-cast mines, oil-cooled multi-disc brakes (MMOT) are applied with an outside diameter of up to 960 mm. Table1 presents some parameters of friction discs of manufacturers of selected heavy goods vehicles (HGVs).

Table 1. Parameters of friction discs with inner toothed rims in wet multi-disc brakes

Manufacturers	Model	External diameter of disc, D (mm)	Internal diameter of disc, d (mm)
Bielaz	75570	885	652
Caterpillar	CAT 785	870	660
Clark	LCB 36200	625.6	480
Komatsu	HD 1600	960	660
Rockwell	5-38856	565	425

Figure 1 shows an exemplary longitudinal section of a wet multi-disc brake used, inter alia, in Bielaz 75570 rigid dump truck. Schematic markings of damage observed during operation are given as follows: *A*, signs of spline deformation; *B*, damage during disassembly because of jamming; *C*, loss of shape stability; *D*, surface wear, annular grooves and indentations.

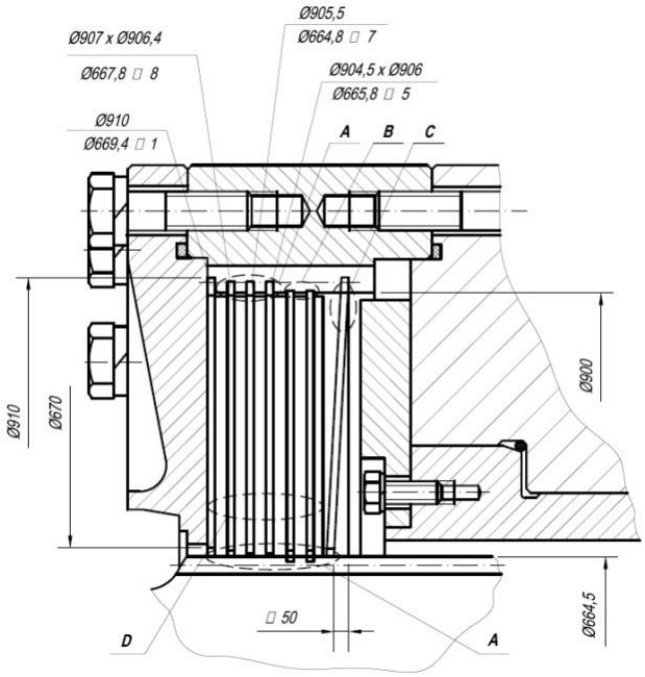

Fig. 1. Exemplary longitudinal section of a wet multi-disc brake in Bielaz 75570 rigid dump truck

The basic technological requirement for such discs is to obtain a minimal value of geometrical deviation of flatness of working surfaces. The technological process of making friction brake discs includes cutting of half-ring blanks, straightening, hardening with high tempering, rough grinding of working surfaces, cutting of gear rims, tempering with resistance up to 8 hours with package cooling and finishing grinding. Unfortunately, after the aforementioned operations, it is often not possible to maintain a proper flatness deviation of the working surfaces. The analysis of foreign technologies in the production of discs shows that specialist companies such as Miba and Hoerbiger are capable of manufacturing discs with a diameter of not more than 600 mm and with an accuracy of flatness deviation of 0.4 mm (Antonyuk, 2004).

A typical technological process for disc manufacturing consists of the following steps (Antonyuk et al., 2017):

- cutting from sheets using press or oxygen-laser cutting;
- thermal straightening using a press and an electrofusion furnace in packages of 80–120 units at 650°C within 6 h, with the subsequent cooling of the package in the air;
- turning of working surfaces;
- high-frequency induction hardening to 30–36 Rockwell hardness or hardening and tempering, which is carried out by heating the freely hanging discs in an electric furnace of up to 850°C for 2 h with subsequent cooling in oil, high tempering is carried out in packages of 70 pieces while heating in the furnace to 575°C for 4–5 h with the final cooling in the air;
- initial grinding of working surfaces using a surface grinder;
- turning of external and internal diameter;
- cutting teeth or external/internal splines using a gear hobber;
- thermal resistance in a 40–50 package at 450°C for 5 h, followed by cooling in air;
- finish grinding of working surfaces;
- manual straightening on the plate;
- degaussing.

Despite the use of a large-range technological process, often the required flat surface tolerance is not achieved in the finished product.

Figure 2 presents a graph showing the percentage share of elements with the assumed tolerance at individual stages of production.

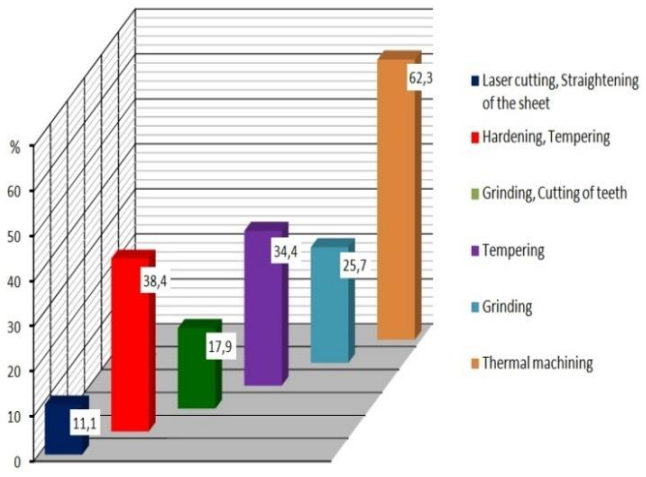

Fig. 2. Percentage share of elements with the assumed tolerance at individual stages of production of discs for BELAZ 7555B

On the basis of the analysis of the impact of individual operations on the deviation of the disc made of 30HGSA steel, with ø507 mm toothed rim, ø449 mm inner hole, 4 mm thickness and final of 269–321 Brinell hardness, the following conclusions were made:

- a significant deviation from the flatness appears at the beginning of the technological process in the operation of cutting out of the blank;
- after hardening and high tempering, internal stresses arise, which cause significant elastic deformation of the discs.

As a result of the presented operations, the sum of the mean strain and the deviation from the plane is not in the acceptable range. In order to remove non-flatness, a number of vibration and thermal methods can be used, but the most effective method has turned out to be the cyclic deformation using the appropriate tooling (Antonyuk et al., 2016).

3. PROPOSED METHODS FOR REDUCING RESIDUAL STRESSES

It can be concluded that the problem of reducing the level of residual stresses is very difficult. When exerting external loads in the process of machining or operation, residual stresses, adding up to stresses from external forces, may exceed the elastic limit, leading to uneven plastic deformation, warping, twisting and so on. Moreover, a significant reduction in counteracting the loss of the element's stability may also occur. The technological cycle of making a part with low stiffness includes many operations: straightening; thermal machining, often repeated multiple times; and machining. Each of these operations contributes its residual stresses, which cause deformations of parts both at the production stage and during their operation. Whilst straightening of non-heat treated rigid elements, such as some shafts, is relatively easy, straightening the flaccid discs is a problem.

3.1. Dynamic stabilisation

One of the most effective methods of reducing residual stresses, confirmed in manufacturing practice is the dynamic stabilisation involving bilateral bending of the disc at a specific amplitude and number of cycles (Antonyuk, 2004). In order to achieve the appropriate stabilisation effects, it is necessary to properly control the process by taking into account material properties, including the size of the cyclic deformation hysteresis loop. For the dynamic stabilisation realisation, it is needed to create elastoplastic deformations and stresses that lead to the occurrence of a loop of a hysteresis in the details' material.

The researches of materials' properties in this zone mark the positive influence of cyclic loading on the decrease in residual pressure and material hardening (Chukkan et al., 2018, Kwofie, 2011, Wang et al., 2017).

The dynamic stabilisation operation can be carried out in a special station, the principle of which is described in the works (Antonyuk, 2004). Figure 3 shows the schematic diagram of the station constructed for the needs of the Bielaz Mining Trucks manufacturer in Minsk, Belarus.

The dynamic stabilisation of friction discs consists in placing a work piece between radially bearing-supported conical upper rollers and similar lower rollers. The upper rollers are able to move vertically and load the disc with a specific transverse force. The disc is rotated through the lower rollers, which are driven by radially spaced electric motors. As a result, bilateral bending of the discs is obtained with a specific transverse force and deflection.

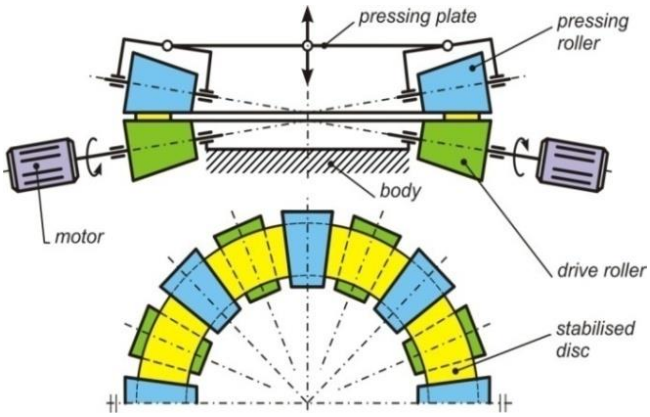

Fig. 3. Schematic diagram of the station for the dynamic stabilisation of friction discs

3.2. Thermal machining (thermo-fixing)

Common methods of reducing residual stresses include various types of heat treatment: tempering, low temperature annealing and natural ageing. The basic mechanism for changing the residual stresses is their relaxation, which proceeds more intensively at raised temperature (Zijlstra et al., 2016). In heat treatment, aimed at reducing residual stresses, the product may, however, undergo 'bending' deformations. A large change in the temperature in the product with residual stresses not only can change the dimensions and shape of the product, but also the product may undergo destruction, especially tensile stresses are dangerous in this case (Świć, 2009). Residual stresses often reduce the strength of products at variable and cyclic loads and affect the wear at sliding friction or rolling friction.

The following have been noticed during the heat treatment process:

- residual stresses are not eliminated completely, which is conditioned by the temperature of tempering, the time of heating, the material and the mass of the product;
- during heating and then cooling, the semi-finished product changes its shape and dimensions;
- tempering is a labour-intensive operation that reduces the process efficiency.

There have been attempts to solve the problem of residual stresses in heat treatment – for example, by introducing a new operation, thermal stabilisation – using special process control systems (Świć, 2009).

The thermo-fixing method, in reference to flat elements such as a plate or a disc, is used in production practice in such a way that the details are placed in a press with a heated die in packets (e.g. 10 pieces each). After a certain time, the packets are cooled slowly under load.

3.3. Vibratory stabilisation

In vibratory machining, yet another processes used in this case, vibration energy penetrates into the metal and, as a result, into the polycrystalline material and crystal displacement takes

place, which is accompanied by a change in the distribution of stresses (Vardanjani et al., 2016). It has been pointed out (Khan and Gangele, 2016; Świć, 2009) that oscillations should occur at a resonant frequency or close to it. The vibration method is suitable for lowering the level of residual stresses obtained by plastic deformation methods in semi-finished products and those generated during mechanical machining.

Another interesting method from a practical point of view involves short-term, swing deformation of a given element. This method is characterised by low energy consumption, simplicity and economy.

Vibration annealing can be applied at any stage of the technological process, for example, during roughing or before finishing, mainly eliminating stresses caused by plastic working of the semi-finished product (Adamski, 2015).

The vibrostabilisation method is used for a wide variety of structural components, including friction discs for brakes and clutches. In the work by Gupalov and Zakuraev (2011), the construction of the stand for the stabilisation of geometrical parameters and the algorithm for controlling the process of lowering the values of flatness deviations of friction discs are presented. Figure 4 shows a diagram of the stand for straightening the discs. The process of disc straightening consists of two stages. Stage 1 includes measurements of the disc and identification of the areas with the highest convexity value. Then a suitable force is applied in these places. During stage 2, vibrations in the frequency range of 50–150% of the disc's own frequency are applied to the static load.

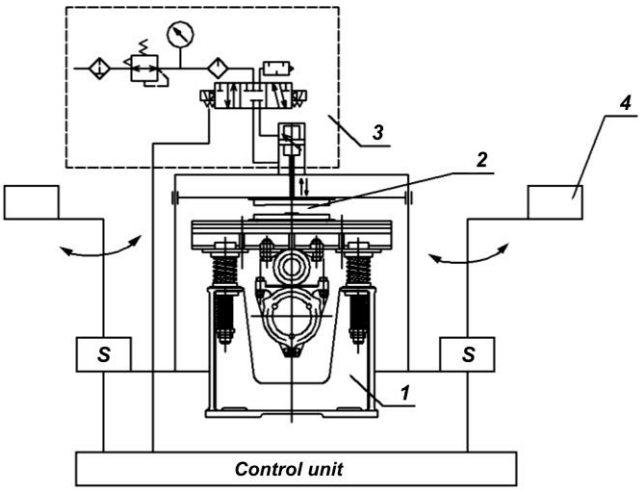

Fig. 4. Schematic diagram of the station for vibrostabilisation of discs (Gupalov and Zakuraev, 2011): 1, vibration inducer and support bracket; 2, work zone; 3, pneumatic system with an actuator; 4, load-relief system; S, damping element

Experiments carried out at the stand (Fig. 4) showed the highest reduction of flatness deviation with a disc deflection of 2–3 mm, a frequency of 50 Hz, a vibration amplitude of 0.32 mm and an exposure time of 3 min. The study by Gupalov (2013) presents a number of research results using this method, including measurements of microhardness of disc material. Gupalov proved that the vibratory stabilisation technology being introduced at machine-building enterprises will improve the quality and reliability of machinery as a whole.

The distinguishing feature of the method presented in the works by Gupalov and Zakuraev (2011) and Gupalov (2013) is the fact that preliminary measurements of the values and type of flatness deviations allow to impact directly on the curved areas of the disc and to create conditions for relaxation of residual stresses with a minimum level of input energy.

4. A CONCEPTUAL DESIGN OF A STAND FOR VIBRATORY STABILISATION OF DISCS

The method of vibratory stabilisation, presented in this article, is an original proposition of the author and bears the hallmark of innovation in this field. Often, the considerations in the literature are limited to the vibration stabilisation of shafts, welded structures and cast structures. What can be observed is the lack of sufficient data on the brake discs. The presented method requires experimental verification. The friction disc has the shape of a ring with a spline notched on the outer circumference and a smooth hole in its centre. It is proposed to stabilise the full disc with a ring load attached to the surface on the radius of the inner hole. Placing an additional load of about 10% load of the plate is used to reduce the natural frequency and efficiently resonance to bring the target material into accelerated ageing and obtain a flatness deviation of <0.2 mm.

Schemes of the proposed solution for the stand and measurement systems are given in Figs. 5 and 6.

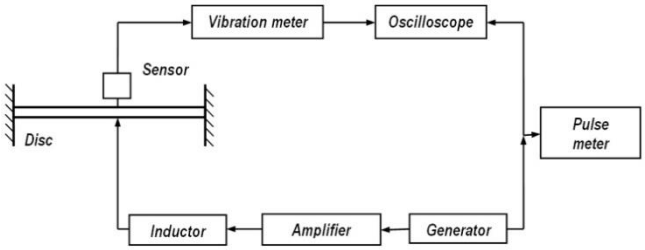

Fig. 5. Schematic drawing of a stand for vibratory stabilisation of discs by resonance

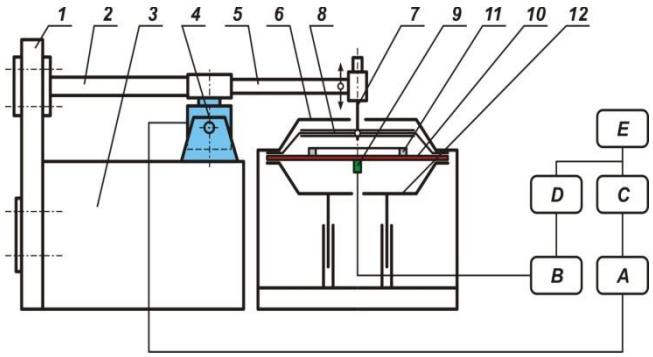

Fig. 6. Schematic diagram of a device for reducing residual stress in discs by vibration: 1, support bracket; 2, beam; 3, body; 4, vibration inducer; 5, slide bar; 6, upper lid; 7, dowel pin; 8, membrane; 9, vibration sensor; 10, disc; 11, additional load; 12, moving table; A, amplifier; B, load amplifier; C, vibration generator; D, oscilloscope; E, control unit

The disc (10) subjected to vibratory stabilisation is placed on the scissor lift table (12). Then the table (12) travels upwards, for example, using a screw mechanism or hydraulic actuators, pressing the disc to the top cover (6). As a result, the rigid edge clamping is obtained. There is a flexible membrane (8) between the top

cover (6) and the plate, thanks to the vibrations of the plate initiated by the movement of air enclosed in airtight space between the plate and the membrane. The movement of the membrane is caused by a pin (7) connected to the moving arm (5).

The vibration excitation system consists of control system E, generator C, amplifier A and vibration inducer (4). The active part of the vibration inducer is connected to the beam 2, whose end is rigidly attached to the support bracket 1. The beam is made of a steel tube. The vibrations of the electromagnetic actuator initiate the flexural vibrations of the beam 2. At the end of the beam, a sliding arm (5) is fixed in the form of a tube made of an aluminium alloy, which is connected to the dowel pin (7) of the membrane (8). In this way, the vibrations of the beam are transferred to the membrane. The vibrations of the disc (10) are processed by the sensor (9) and the charge amplifier B into an electrical signal that is then fed into the oscilloscope D. The oscilloscope is simultaneously fed with the voltage from the generator C. Because the frequencies of both runs are same, the oscilloscope screen displays an ellipse. Changing the frequency of the generator causes a change in the frequency of forced oscillations of the inductor–disc system. At the moment of equating the frequency of forced vibrations with the natural frequency of the plate, a resonance phenomenon arises. It is manifested by a rapid increase in the vibration amplitude of the plate. Then the largest amplitude is observed on the oscilloscope screen. By slowly changing the frequency of the generator in the resonance zone, the phase shift between the applied force and the vibrating beam changes. At resonance, the shift is 90º, which is equivalent to the vertical position of ellipse on the oscilloscope screen. Thus, when going through resonance, the 'rotation' of the ellipse occurs. After accurately capturing the resonance moment, the plate's natural frequency is read using the graphic interface of the control system E. For the discussed system, the search for these frequencies takes place by manually tuning the frequency of the generator to the disc's natural frequencies.

It is proposed to use an inductor model S062 with the frequency range of up to 200 Hz and an amplitude of 1 mm. Magnetic vibration inducers dramatically reduce the impact force as the excitation frequency increases above 200 Hz (Uhl and Panuszka, 1983), as inductive resistance increases. Therefore, in Sections 5 and 6, an analytical and numerical method is proposed for choosing the size of the additional secondary ring, taking into account its radius.

5. ANALYTICAL DETERMINATION OF NATURAL FREQUENCY IN BRAKE DISCS

In order to precisely determine the frequency of generated pulses and selection of the vibration inducer, analytical calculations of the natural frequency were carried out depending on the size of the disc, its fixing and the radius of the additional mass. Figure 7 presents disc models used for further calculations.

Study of the boundary problem of axisymmetric vibrations of the disc with discrete intercalations, whose distribution depends on the radial variable, is about solving the boundary problem described by equation (1) (Jaroszewicz and Zoryj, 2005):

$$L_0[u] + r\chi u - \sum_{i=1}^{k} \alpha_i\, u(r_i)\delta(r - r_i) = 0\,, \qquad (1)$$

$$0 < r_1 < r_2 < \cdots < r_k < R.$$

Differential operator in equation (1) is in the following form:

$$L_0[u] = u^{IV} + \frac{2}{r}u^{III} - \frac{1}{r^2}(1 + 2n^2)u^{II} + \frac{1}{r^3}(1 + 2n^2)u^{I} - \\ - \frac{1}{r^4}(1 + 2n^2)u\,, \qquad (2)$$

where $u = u(r)$ is the bending amplitude, $\delta(r)$ is the Dirac delta function, $\alpha_i = \frac{1}{D}(m_i\omega^2 - c_i)$ and $\chi = \frac{1}{D}(\varrho h\omega^2 - b\omega - \kappa^2)$.

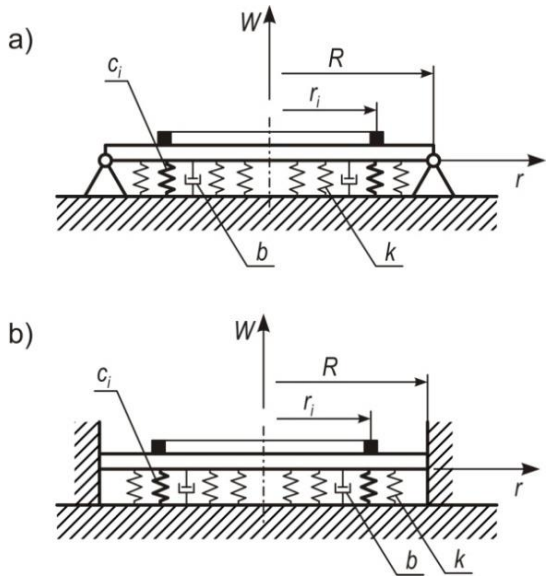

Fig. 7. Discs used in the analysis: (a) a disc pivotally supported at the edge and (b) a disc clamped at the edge

In equation (1) and expression (2) and in Fig. 7, the following parameters of intercalations in the form of point mass m_i and elastic supports with rigidity c_i are distributed on radii r_i: D is the cylindrical rigidity, ω is the frequency parameter, ϱh is the volumetric mass density, χ is the elastic foundation coefficient and n is the mode of vibrations.

Cylindrical stiffness of the disc can be defined using the following formula:

$$D = \frac{Eh^3}{12(1 - \nu^2)}.$$

In this article, two types of fixing the edges of the disc are considered: clamped and freely supported on the edge (Fig. 7):

$$u(R) = 0, u'(R) = 0, \qquad (3)$$

$$u(R) = 0, u''(R) + \nu R^{-1}u' = 0. \qquad (4)$$

Assuming that a massless disc is homogeneous, its edge is clamped and focusing on axisymmetric oscillations, the solution of the auxiliary problem limited in zero (equation 1) is in the following form (Roberson, 1951):

$$u(r) = c_0 + c_1 r^2 - F_j K_0(r, r_j)\Theta(r - r_j), \qquad (5)$$

where c_0, c_1 are constants of integration, $K_0(r, r_j)$ is the basic function of operator $L_0[u]$ where $\alpha = r_j$ and $\Theta(r)$ is the Heaviside function.

The value of F_j characterises a flex real forces concentrated on a circle with radius $r_j (r_j \geq r_i)$. From equation (5), we obtain

$$u'(r) = c_1 r - F_j K'_o(r, r_j)\theta(r - r_j). \quad (6)$$

By substituting equations (5) and (6) into condition (3), integration constants c_o, c_1 were determined, and on the basis of equation (6), impact coefficients β_{ij} were determined:

$$\beta_{ij} = u_j(r_i) = \frac{1}{2R}\left[\left(R^2 - r_j^2\right)K'_{Ri} - 2RK_{Ri}\right]. \quad (7)$$

In the case of $i = j = 1$ in equation (7), the natural frequency ω of a mass less plate carrying point mass M on a circle with a radius $r = r_1$ was determined:

$$\frac{\omega^2}{D} = \frac{1}{\tilde{\varrho}\beta_{11}}\ M = 2\pi r_1 \tilde{\varrho}, \quad (8)$$

where $\tilde{\varrho}$ is the linear density of mass rib and D is the cylindrical stiffness.
Impact coefficient β_{11} will eventually take the form of

$$\beta_{11} = \frac{r_1}{2R}\left(\frac{1}{4}R^3 - \frac{1}{4}\frac{r_1^4}{R} - r_1^2 R \ln\frac{R}{r_1}\right). \quad (9)$$

By analogy, vibration frequencies corresponding to the first non-axisymmetric form can be determined. In the case of a freely supported plate, by taking into account the boundary conditions (4), the transformation should be carried out in the same way and finally obtained in the following form:

$$\beta_{11} = \frac{r_1}{2(1+\nu)}\left[\frac{3}{4}R^2 - r_1^2\left(1 - \ln\frac{R}{r_1}\right) + \nu\frac{1}{4}R^2 - r_1 \ln\frac{R}{r_1}\right]. \quad (10)$$

On the basis of equations (9) and (10), considering equation (8) and pointing r_1 to 0, we get a much simpler pattern for the square of the basic frequency for cases when the mass M significantly exceeds the unladen weight of the plate and is focused at the centre of symmetry $(r = 0)$ (Jaroszewicz and Zoryj, 2005):

$$\omega^2 = \frac{16\pi D}{MR^2},\ \omega^2 = \frac{16\pi D(1+\nu)}{MR^2(3+\nu)} \quad (11)$$

On the basis of equation (8), basic frequencies ω can be calculated by introducing frequency parameter $\gamma(x)$, which becomes dependant on the relation $x = \frac{r_1}{R}$. On the basis of equations (9) and (10), the following can be expressed:

$$\omega = \gamma(x)\frac{1}{R^2}\sqrt{\frac{D}{\varrho h}}. \quad (12)$$

For a clamped disc,

$$[\gamma(x)]^2 = \frac{16\pi}{1 - x^4 + 4x^2 \ln x}. \quad (13)$$

For a freely supported disc,

$$[\gamma(x)]^2 = \frac{16\pi(1+\nu)}{[3 - x^2(1 + \ln x) + \nu + 4x^2 \ln x]}. \quad (14)$$

Fig. 8 shows a graph of waveform in the frequency parameter depending on the radius of distribution of the additional mass and the method of supporting the disc.

To calculate the frequency in rad/s, formulas (12), (13) and (14) should be used, in which the following data are adopted: R = 0.45 m, h = 0.003 m and D = 620 Nm. The ring mass is distributed over a radius of r_1 = 0.3 m. Its value is 10% of the disc's own weight, with m_1 = 0.94 kg. Assuming r_1 and m_1, the cross-sectional dimensions of the ring are determined and the natural frequencies are calculated:

- for clamped disc – ω = 60 rad/s,
- for freely supported disc – ω = 35.4 rad/s.

Bernstein–Kieropian tables can be used to calculate the higher frequencies of discs (Bernstein and Kieropian, 1960).

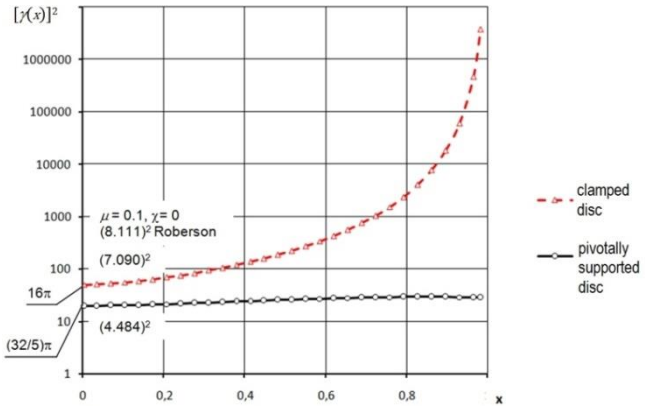

Fig. 8. The dependence of the basic frequency parameter γ on the radius of distribution of the additional mass $x = \frac{r_1}{R}$ for the clamped disc and the pivotally supported disc

The inductor proposed in this work fully meets the demand. The use of higher additional weight m_1 results in a reduction of its own frequency. The frequency parameter values $\gamma(x)$ can also be read from the graph presented in Fig. 8.

6. RESULTS OF ANALYTICAL AND NUMERICAL CALCULATIONS

For comparison purpose, calculations of natural frequency of discs were made using the analytical relationships presented in Section 5 and the finite element method (FEM). The Autodesk Inventor software package equipped with the NASTRAN module was used. The comparison concerned only the first value of natural frequency of discs, with an additional mass (m_a) determined analytically using the relations (11) and (12) and discs without additional mass. The focus was on calculations of modal analysis with linear material behaviour. Calculations are conducted for five vehicle discs mentioned in Table 1. The dimensions of discs, material constants and boundary conditions were adopted as in analytical studies. Owing to the uncomplicated shape of the disc, the problem was modelled as spatial, adopting a standard grid using parabolic tetrahedral elements. Table 2 presents information on the parameters of the generated grid for the target disc.

Table 2. Mesh parameters

Type mesh	Parabolic tetrahedral
Maximum element growth rate	1.5
Refinement ratio	0.2
Minimum/maximum triangle angle	20/30°
Upper Jacobian ratio bound	16 points
Size	12 mm
Tolerance	0.0356 mm
Quality	High

The results of analytical and numerical calculations are presented in Table 3. The calculation of the percentage difference of results for individual types of discs and calculation methods was made according to formula (15):

$$\Delta s = \left|\frac{\omega^{\mathrm{ANL}} - \omega^{\mathrm{FEM}}}{\omega^{\mathrm{ANL}}}\right| \cdot 100\% , \quad (15)$$

where, ω^{ANL} is the natural frequency determined analytically and ω^{FEM} is the natural frequency determined by FEM.

Table 3. Results of the comparison for a disc clamped at its outer radius

Vehicle model	75570		CAT 785		LCB 36200		HD 1600		5-38856	
r_1/R	0.74		0.76		0.76		0.67		0.75	
First natural frequency of a disc	ω^{ANL}	ω^{FEM}	ω^{ANL}	ω^{FEM}	ω^{ANL}	ω^{FEM}	ω^{ANL}	ω^{FEM}	ω^{ANL}	ω^{FEM}
	(rad/s)									
Without additional load $\mu=m_d/M=0$	249.4	244.4	258.1	253.2	499.2	489.7	211.9	207.7	611.9	600.1
Δs (%)	2.0		1.9		1.9		2.0		1.9	
With additional load $\mu=m_d/M=0,1$	830.3	398.9	975.2	341.6	1,966.1	828.9	555.8	312.9	2202.7	822.1
Δs (%)	51.9		64.9		57.8		43.7		62.7	

7. DISCUSSION OF RESEARCH RESULTS

Figure 7 and Table 3 show that the analytical frequency calculations obtained by the simplified Cauchy function without taking into account the weight of the plate and additional load lead to small differences (2%) in relation to numerical calculations and very significant differences (43–65%) with additional load distributed over radius *x*. The reason for this is the omission of the weight of the disc in the analytical method. The numerical model includes, in addition to load, an additional load–rib with stiffness – discrete inclusion into continuous stiffness. Consideration of stiffness and load–rib in analytical terms is very difficult. In addition, attention should be paid to the fact that the ring load spread over radius *x* increases the frequency (according to the graph in Fig. 7) as opposed to Roberson's calculations (Roberson, 1951), where the point load (Table 4) placed at the centre of the disc's symmetry reduces it.

Table 4. Base frequency parameter γ in relation to additional load μ

μ	0	0.05	0.1
γ	10.214	9.012	8.111

The proposed analytical methods using the Cauchy function and FEM obtain results convergent to the experiment described in Section 9.5 of a monograph by Jaroszewicz and Zoryj (2005).

8. CONCLUSION

The engineering method of selection and calculation of loading modes is developed for purposeful use of dynamic stabilisation. The introduced technique has been probe tested and implemented for developing the technological concept and for creation of installation with digital programme control for dynamic stabilisation of frictional brake discs of dump trucks.

The method of selection and calculation of control charts can be used for the dynamic stabilisation realisation in order to increase the accuracy and working capacity of details of clutch plate type, frictional discs, crankshafts, torque rods, pipes, sleeves and some other non-rigid details.

The device proposed at this work is characterised by the use of a pneumatic cushion, thanks to the possibility of inducing vibrations of higher rows.

Vibratory stabilisation is a more universal method than dynamic stabilisation; it can be applied to various objects, often with a complicated shape. In order to correctly perform the vibratory stabilisation process, it is advisable to carry out preliminary analytical or numerical calculations of the basic frequency estimation of the object.

REFERENCES

1. **Adamczyk J.** (1993), *Theoretical metallurgy. Plastic deformation, strengthening and cracking*, 3, Publisher of the Silesian University of Technology, Gliwice (in Polish).
2. **Adamski W.** (2015), Impact of Modern Manufacturing Technologies at Aircraft Design, *Mechanik*, nr 12, 1-5 (in Polish).
3. **Almer J.D., Cohen J.B., Moran B.** (2000), The effects of residual macrostresses and microstresses on fatigue crack initiation, *Materials Science and Engineering*, A284, 268-279.
4. **Antonyuk V.** (2004), *Dynamic stabilisation of geometrical parametres of details with alternating*, UP "Technoprint" Minsk.
5. **Antonyuk V., Jaroszewicz J., Radziszewski L., Dragun Ł.** (2016), Theoretical stress analysis-based improvement of friction clutch disc manufacturing process, *Czasopismo Techniczne. Mechanika,* Politechnika Krakowska, 113(4-M), 73-79.
6. **Antonyuk V., Sandomirskij S., Jaroszewicz J.** (2017), Testing the possibility of estimation of residual stress based on gradient of magnetic field, *Przegląd Mechaniczny*, 2, 9-13 (in Polish).
7. **Bernstein, S.A., Kieropian, K.K.** (1960), *Calculation of frequency of bar systems by means of spectral function*, Goststrojtechizdat, 281, Moscow (in Russian).

8. **Chukkan J.R, Wu G., Fitzpatrick M.E., Eren E., Zhang X., Kelleher J.** (2018), Residual stress redistribution during elastic shake down in welded plates, *MATEC Web of Conferences*, *FATIGUE 2018*, 165, 21004, 1–6.
9. **Ghasri-Khouzani M., Pengb H., Roggec R., Attardod R., Ostiguyd P., Neidige J., Billof R., Hoelzleg D., Shankara M.R.** (2017), Experimental measurement of residual stress and distortion in additively manufactured stainless steel components with various dimensions, *Materials Science & Engineering*, A707, 689–700.
10. **Gupalov B.A.** (2013), Technology and equipment for friction disk vibratory dressing, *Wiestnik IrGTU*, 9(80), 57-63 (in Russian).
11. **Gupalov B.A.**, **Zakuraev W.W**. (2011), Kinetics of geometric parameters changes of friction discs during vibratory processing, *Wiestnik Nauki Sibri*, 1(1), 682-685 (in Russian).
12. **Hałas W.** (2010), *Study of the influence of residual stresses on the accuracy of shaft production*. *Dissertation,* Publisher of the Lublin University of Technology, Lublin (in Polish).
13. **Jaroszewicz J., Zoryj L.** (2005), Methods for analyzing axisymmetric oscillations of circular plates using the Cauchy influence function method, *Rozprawy Naukowe Politechniki Białostockiej*, 124, Białystok.
14. **Khan N., Gangele A.** (2016), Residual Stress Measurement Techniques: A Review, *International Journal of Research in Engineering and Applied Sciences*, 6(4), 151-157.
15. **Kwofie S.** (2011), Description and simulation of cyclic stress-strain response during residual stress relaxation under cyclic load, *Procedia Engineering*, 10, 293–298.
16. **Meng L., Atli M., He N.** (2017), Measurement of equivalent residual stresses generated by milling andcorresponding deformation prediction, *Precision Engineering*, 50, 160-170.
17. **Mughrabi H.** (2013), Microstructural fatigue mechanisms: Cyclic slip irreversibility, crack initiation, non-linear elastic damage analysis, *International Journal of Fatigue,* 57, 2–8.
18. **Pedrosa P.D., Rebello J.M.A., Fonseca M.P.C.** (2011), Residual stress state behaviour under fatigue loading in duplex stainless steel, *The Journal of Strain Analysis for Engineering Design*, 46(4), 298–303.
19. **Roberson R.E.** (1951), Vibrations of clamped circular plate carring concentrated mass, Journal Applied Mechanics, 18, 4, 349-352.
20. **Rossini N.S., Dassisti M., Benyounis K.Y., Olabi A.G.** (2012), Methods of measuring residual stresses in components, *Materials and Design*, 35, 572–588.
21. **Salvati E., Korsunsky A.M.** (2017), An analysis of macro- and micro-scale residual stresses of Type I, II and III using FIB-DIC micro-ring-core milling and crystal plasticity FE modelling. *International Journal of Plasticity*, 98, 123-138.
22. **Sangid M.D.** (2013), The physics of fatigue crack initiation, *International Journal of Fatigue*, 57, 58–72.
23. **Schajer G.S.** (2013), *Practical residual stress measurement methods*, John Wiley & Sons Ltd., London.
24. **Świć A.** (2009), *The technology of processing shafts with low stiffness*, Publisher of the Lublin University of Technology Lublin (in Polish).
25. **Uhl T., Panuszka R.** (1983), Determination of resonant frequencies of continuous mechanical systems on the example of a beam and an oscillating plate*, Archiwum Budowy Maszyn*, 1-2, 111-123 (in Polish).
26. **Vardanjani M.J., Ghayour M., Homami R.M.** (2016), Analysis of the vibrational stress relief for reducing the residual stresses caused by machining, *Experimental Techniques*, 40(2), 705–713.
27. **Vourna P., Ktena A., Tsakiridis P.E., Hristoforou E.** (2015), A novel approach of accurately evaluating residual stress and microstructure of welded electrical steels, *NDT & E International*, 71, 33–42.
28. **Wang Q., Liu X., Yan Z., Dong Z., Yan D.** (2017), On the mechanism of residual stresses relaxation in welded joints under cyclic loading, *International Journal of Fatigue*, 105, 43–59.
29. **Wesołowski K.** (1981), *Metallurgy and heat treatment*, WNT, Warsaw (in Polish).
30. **Zijlstra G., Groen M., Post J., Ocelík V., De Hosson J.Th.M.** (2016), On the role of the residual stress state in product manufacturing, *Materials & Design*, 105, 375–380.

The research was conducted within S/WZ/1/2015 project and was financed from Ministry of Science and Higher Education funds.

sciendo

DOI 10.2478/ama-2019-0007

acta mechanica et automatica, vol.13 no.1 (2019)

EXPERIMENTAL INVESTIGATIONS OF ELIMINATION THE STICK-SLIP PHENOMENON IN THE PRESENCE OF LONGITUDINAL TANGENTIAL VIBRATION

Mariusz LEUS*, Marta ABRAHAMOWICZ*

*Department of Mechanical Engineering and Mechatronics, West Pomeranian University of Technology in Szczecin
al. Piastów 19, 70-310 Szczecin, Poland

mariusz.leus@zut.edu.pl; marta.abrahamowicz@zut.edu.pl

received 2 January 2019, revised 13 March 2019, accepted 20 March 2019

Abstract: The article presents a scheme and description of the test stand as well as selected experimental results of the influence of longitudinal tangential vibrations on the stick-slip phenomenon. The tests were carried out at a constant forced vibration frequency f = 2000 Hz, as a function of the amplitude of the vibration velocity v_a. The position of the sliding body and the drive force necessary to make the body slip and maintain this motion were measured. The measurements were made in two successive stages. In the first stage, when the substrate on which the sliding occurred was stationary. In the second one, the substrate is in a vibrating motion in the direction parallel to the slip. The conducted experimental analyses have shown that longitudinal tangential vibrations can contribute to the reduction or even complete elimination of the stick-slip phenomenon.

Key words: stick-slip phenomenon, drive force, longitudinal tangential vibrations

1. INTRODUCTION

Uncontrolled stepwise movements of the sliding body, known as the stick-slip phenomenon, which can occur in the sliding motion as a result of the friction force, are an undesirable phenomenon and hinder proper operation of the machines. The main cause of their formation is attributed to high difference between static and kinetic friction coefficients (Abdo et al., 2010; Abdo and Zaier, 2012; Canudas de Wit et al., 1995; Mfoumou et al., 2019; Mokhtar et al., 1998; Neubauer et al., 2005), increase in static friction force during standstill, low slip velocity, or low stiffness of the friction pair system (Ozaki and Hashiguchi, 2010).

This unstable movement is repeated at short intervals, more or less regularly, until the slip velocity of the sliding body does not exceed the so-called critical velocity. Above this speed, only motion of the body appears, which is deprived of undesirable jumps. Therefore, the amplitude and frequency of the stick-slip motion depend mainly on the sliding velocity. The mass of the sliding element and the stiffness of the system also play an important role (Grudziński and Warda, 1993).

The stick-slip motion is a phenomenon that occurs both in everyday life and in technology. The effect of this phenomenon is the sound of a bow on the strings of a violin, the squeaking sound of hinged doors, the squeak of tram wheels on a turn and the squeak of chalk on the board (Abdo et al., 2010; Kligerman and Varenberg, 2014; Popp and Rudolph, 2004). The stick-slip phenomenon may also cause disturbances in the movement of moving assemblies of machine tools, positioning devices, measuring instruments or manipulators (Mfoumou et al., 2019; Rymuza, 1992). This has a negative effect on the positioning accuracy of the components, as their position is determined by the amplitude of longitudinal vibrations – the amplitude of jump of the sliding element. The stick-slip vibrations are also common in the drilling operations in the oil and gas industry. They drastically decrease the rate of penetration (Qiu et al., 2018; F. Aarsnes et al., 2018), cause premature tool failures and adversely affect the borehole quality (Tang et al., 2015, 2017), which significantly increases drilling costs (Zhu et al., 2014).

The stick-slip motion contributes to faster wear of the friction pair's components. Therefore, these vibrations may be acceptable, provided that their amplitude is sufficiently small (Popp and Rudolph, 2004). However, it is desirable to completely eliminate or at least reduce the intensity of amplitude of these vibrations. There are several ways to eliminate the stick-slip phenomenon, which include selection of optimal materials and surface roughness of friction pair elements (Kligerman and Verenberg, 2014; Kröger et al., 2008), application of lubrication (Zuleeg, 2015), reduction of normal pressure at the contact (Kröger et al., 2008), replacement of sliding contact with rolling contact (Rymuza, 1992) and introduction of forced external vibrations into the area of contact, which cause a reduction of the time of standstill of the sliding body (Abdo et al., 2009, 2010; Abdo and Zaier, 2012; Neubauer et al., 2005; Popov et al., 2010; Popp and Rudolph, 2003, 2004; Teidelt et al., 2012).

In the works available in the literature, in which the issue of the influence of vibrations on the stick-slip phenomenon was discussed, the main attention has so far been focused on the use of normal vibrations to eliminate this phenomenon. In these works, two ways of introducing vibrations into the contact area were presented. Abdo et al. (2009, 2010) and Abdo and Zaier (2012) carried out the experimental tests of stick-slip phenomenon on the especially constructed pin-on-disc machine, which gives the possibility to generate vertical vibrations of revolving disk. The obtained results show that the level of stick-slip amplitude reduction depends on factors such as the type of friction pair material, amplitude and frequency of excited vibrations and relative humidity. The authors of the above-mentioned work observed that with the

increase in amplitude of excited vibration, the amplitude of stick-slip motion significantly decreased. Neubauer et al. (2005) and Popp and Rudolph (2003, 2004) described the possibility of stick-slip reduction through the active control of vibration with the use of oscillating normal force. The tests carried out by them confirmed that after active control, the stick-slip motion disappeared.

In the recent years, works in which the results of experimental research indicate the possibility of using tangential vibrations to reduce the stick-slip movement have also appeared (Popov et al., 2010; Teidelt et al., 2012).

This article presents a test stand and selected results of experimental tests of the application of tangential vibrations of the substrate on which the slip movement is performed to the elimination of the stick-slip phenomenon. Experimental tests were carried out as a function of the amplitude of vibration velocity v_a at their determined frequency f and determined drive velocity v_d. The direction of tangential vibrations of the substrate was assumed to be in line with the direction of sliding of the body. The tests were performed for the steel–steel contact.

2. DESCRIPTION OF THE STICK-SLIP PHENOMENON

The physical model of a sliding pair with kinematic inducement for the analysis of the stick-slip phenomenon is shown in Fig. 1. The model consists of a body ***A*** of mass m sliding on a substrate ***B*** by means of a drive providing a constant velocity v_d. The sliding body is connected with the drive by means of a spring with a stiffness of k_d.

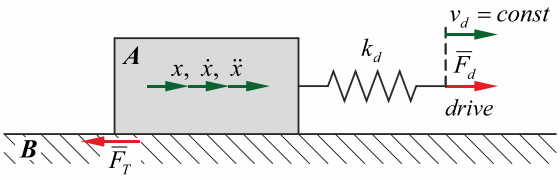

Fig. 1. Physical model of the sliding pair

The equation of the motion of the sliding body ***A*** along the axis of the assumed direction of sliding in accordance with the direction of the drive is in the following form:

$$m\ddot{x} = F_d - F_T, \tag{1}$$

where m is the mass of the sliding body, $\ddot{x}$ is the its acceleration, F_d is the drive force and F_T is the friction force.

The drive force can be determined from the following dependence:

$$F_d = k_d(s_d - x), \tag{2}$$

where

$$s_d = v_d \cdot t. \tag{3}$$

The k_d value is the drive stiffness, s_d is the drive displacement, x is the position of the sliding body, v_d is the drive speed and t is the time.

The characteristics representing the course of the stick-slip phenomenon in the form of rest periods of body ***A*** (stick – t_s) and slip-jump (slip – t_r), corresponding to the model of the slide pair shown in Fig. 1 are schematically presented in Fig. 2.

In the time interval from t = 0 (the moment when the drive starts to move at v_d = const) to $t = t_{s1}$, body ***A*** is at rest, because the drive force F_d is lower than the force of static friction $F_{T0} = \mu mg$, where μ is the friction coefficient and g is the gravitational acceleration. After reaching the time t_{s1}, the drive force F_d starts to exceed the friction force F_{T0} and the slip movement of the body ***A*** starts with high acceleration $\ddot{x}$ and its slip speed $\dot{x}$ exceeds the value of the drive speed setpoint v_d. After half of the duration of motion t_{r1} has elapsed, the value of the drive force F_d decreases below the value of the friction force F_T and the braking of the sliding body begins, which after reaching the time t_{r1} stops and remains at rest during the period t_{s2}. After this time, the movement of the sliding body is repeated cyclically. In real systems, the effect is a jumping movement of the sliding element, the so-called stick-slip phenomenon.

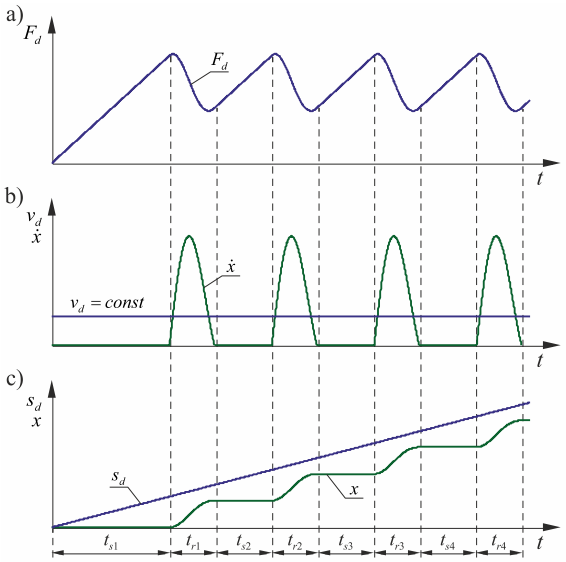

Fig. 2. Characteristics of the stick-slip phenomenon. Time courses of: (a) drive force F_d, (b) drive velocity v_d and velocity of the sliding body $\dot{x}$ and (c) drive displacement s_d and position x of the sliding body

3. THE TEST STAND

The experimental test of the stick-slip phenomenon in the presence of longitudinal tangential vibrations was carried out on a test stand designed and constructed to determine the quantitative changes in friction forces in the sliding movement caused by the introduction of tangential vibrations into the contact area of the sliding pair. A detailed description of this stand is presented in the works (Leus and Gutowski, 2011; Gutowski and Leus, 2012, 2015). To determine the impact of vibrations on the stick-slip motion, this stand is equipped with an additional system to measure the position of the body and drive and a mechanism to change the stiffness of the drive system. Mechanical part of the test stand prepared for testing is presented in Fig. 3, whereas Fig. 4 shows the block diagram of the elaborated stand.

The basic element of this stand is a sliding pair consisting of a sliding upper sample and a fixed sample placed on the roller guides of the base. As the upper sample is moved, the lower sample can be set in a vibrating motion in accordance with the direction of movement. Vibration is induced by a piezoelectric inductor powered by the PIEZOMECHANIC RCV 1000/3 amplifier. The sliding motion of the upper sample is achieved by a drive system consisting of an EPX40 linear guide equipped with a

DOI 10.2478/ama-2019-0007

propeller, a step-motor with a gear and a driver. This system also includes a ring dynamometer and a unit with a certain stiffness to transmit the drive force. Replacement of the spring in this assembly allows to change the stiffness of the drive system k_d (Fig. 5). The motor operation is controlled by the SMC64v2 controller. The change in velocity v_d is obtained by changing the frequency f_{gen} of impulses fed from the rectangular waveform generator to this controller. In addition, the upper sample may be loaded in the normal direction with an additional external force F_z centrally applied to the sample by means of a band loaded with a lever with weights.

During the test, several values, such as the drive force F_d, the external force F_z, the acceleration $\ddot{x}$ and the displacement x of the upper sample, the acceleration $\ddot{u}$ of the lower sample, the drive displacement s and the drive speed v_d, are measured simultaneously. The value of the drive force F_d and the external force F_z are measured with ring dynamometers, whereas the measurement of the distance x travelled by the sliding body and the distance s travelled by the drive is performed with WA-L inductive displacement transducers placed in the sliding axis. Signals from ring dynamometers and displacement transducers are transmitted to the HBM MGA II amplifier equipped with ME10 and ME50 measuring modules. The acceleration of the upper and lower samples is measured by PCB acceleration sensors, which send signals to the PCB 481A load amplifier. To measure the drive speed v_d, an MOK50 encoder was used, whose rotary axis was connected to the lead screw of the linear guide.

All measured signals are transferred to a measurement computer equipped with a DS1104 measurement card and ControlDesk software from dSPACE. This system provides continuous control and recording of the measured values and enables the control of the vibration inductor amplifier and the step-motor controller.

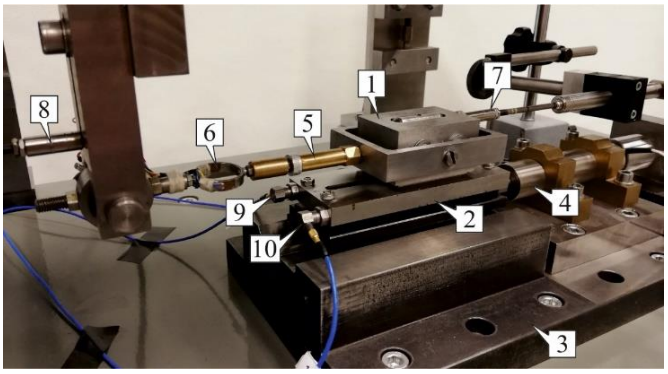

Fig. 3. Photo of mechanical part of test stand: 1, upper sample; 2, lower sample; 3, base; 4, vibration exciter; 5, stiffness adjustment system k_d; 6, ring dynamometer; 7 and 8, WA-L displacement transducers; 9 and 10, accelerometers

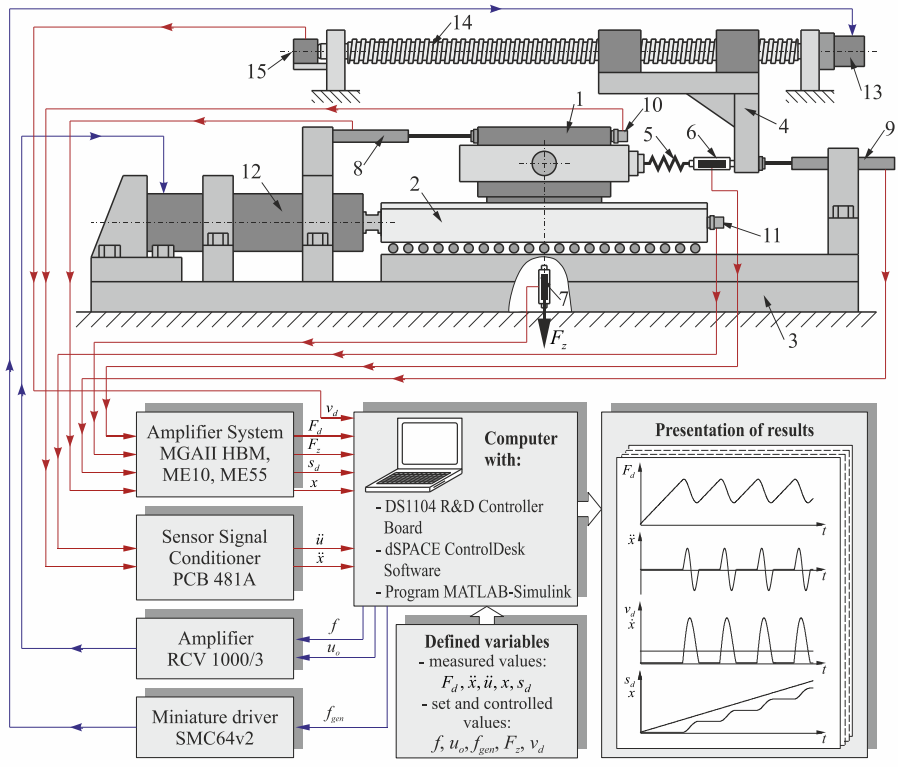

Fig. 4. Diagram of the test stand together with the measurement and recording system: 1, upper sample; 2, lower sample; 3, base; 4, driver; 5, stiffness adjustment system k_d; 6 and 7, ring dynamometers; 8 and 9, WA-L displacement transducers; 10 and 11, accelerometers; 12, vibration exciter; 13, step-motor with a gear; 14, linear guide; 15, encoder

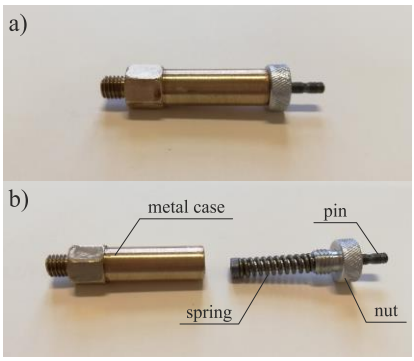

Fig. 5. Drive stiffness k_d change system: (a) general view and (b) detailed view

4. EXPERIMENTAL INVESTIGATIONS AND THEIR OUTCOMES

The aim of the experimental tests presented in this article was to investigate the possibility of using forced longitudinal tangential vibrations introduced into the contact area to eliminate the stick-slip phenomenon. In this study, the quantitative changes the drive force F_d and the position of the moved body x in two consecutive stages of motion were determined. In each variant, the movement of the upper body was carried out without forced vibrations in the first stage and with forced vibrations of the lower body in the second stage.

The tests were carried out for steel–steel contacts with a harmonic excitation at a constant frequency f = 2000 Hz. The variable parameter was the amplitude v_a of vibration velocity, being a function of amplitude u_o and frequency f of vibrations. The change in value v_a was obtained by changing the amplitude u_o of these vibrations. The mass of the sliding body ***A*** amounted to m = 0.5 kg, and the additional external load in the normal direction amounted to F_z = 100 N. The values of drive speed v_d and stiffness k_d were selected in such a way that the stick-slip phenomenon occurred during the movement of the upper body. They amounted to v_d = 0.4 mm/s and k_d = 20227 N/m, respectively.

Figures 6 and 7 illustrate the courses of the drive force F_d, position x of the sliding body and displacement s_d of the drive. Figure 6 shows the waveforms of these values in the range when the amplitude v_a of the vibration velocity was lower than the drive velocity v_d. The values of this amplitude were assumed at four different levels and amounted to v_{a1} = 0.1 mm/s, v_{a2} = 0.15 mm/s, v_{a3} = 0.25 mm/s and v_{a4} = 0.3 mm/s. From the presented graphs, it can be seen that for the adopted test parameters (v_d, k_d, F_z, f), the induction of longitudinal tangential vibrations of the substrate on which the sliding movement took place caused a significant reduction of the stick-slip phenomenon in the form of a reduction in the amplitude of drive force jumps, thus a reduction in the amplitude of the jumps of the sliding body. With increasing amplitude v_a of the vibration velocity, the elimination degree of the stick-slip phenomenon is increased.

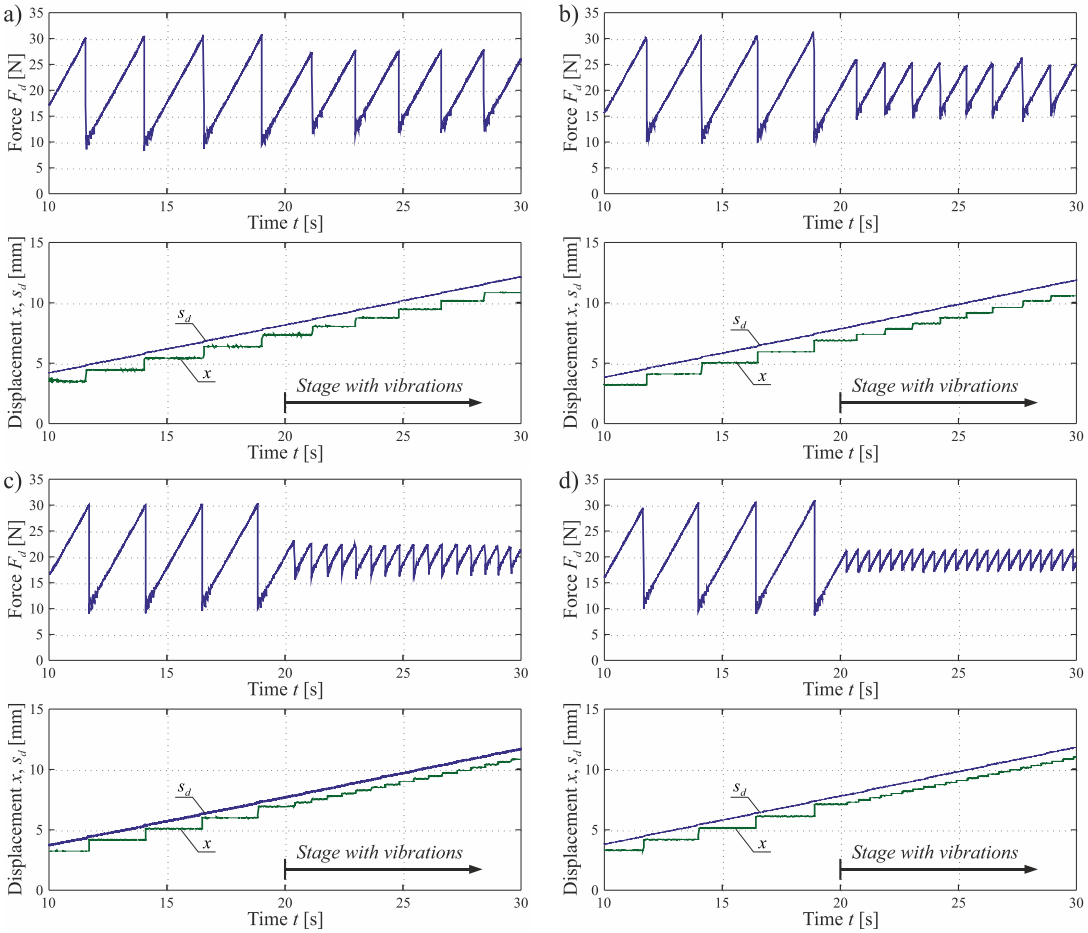

Fig. 6. Experimentally determined waveforms of drive force F_d, displacement of the sliding body x and drive displacement s_d for: (a) v_a = 0.1 mm/s, (b) v_a = 0.15 mm/s, (c) v_a = 0.25 mm/s and (d) v_a = 0.3 mm/s; f = 2000 Hz, v_d = 0.4 mm/s.

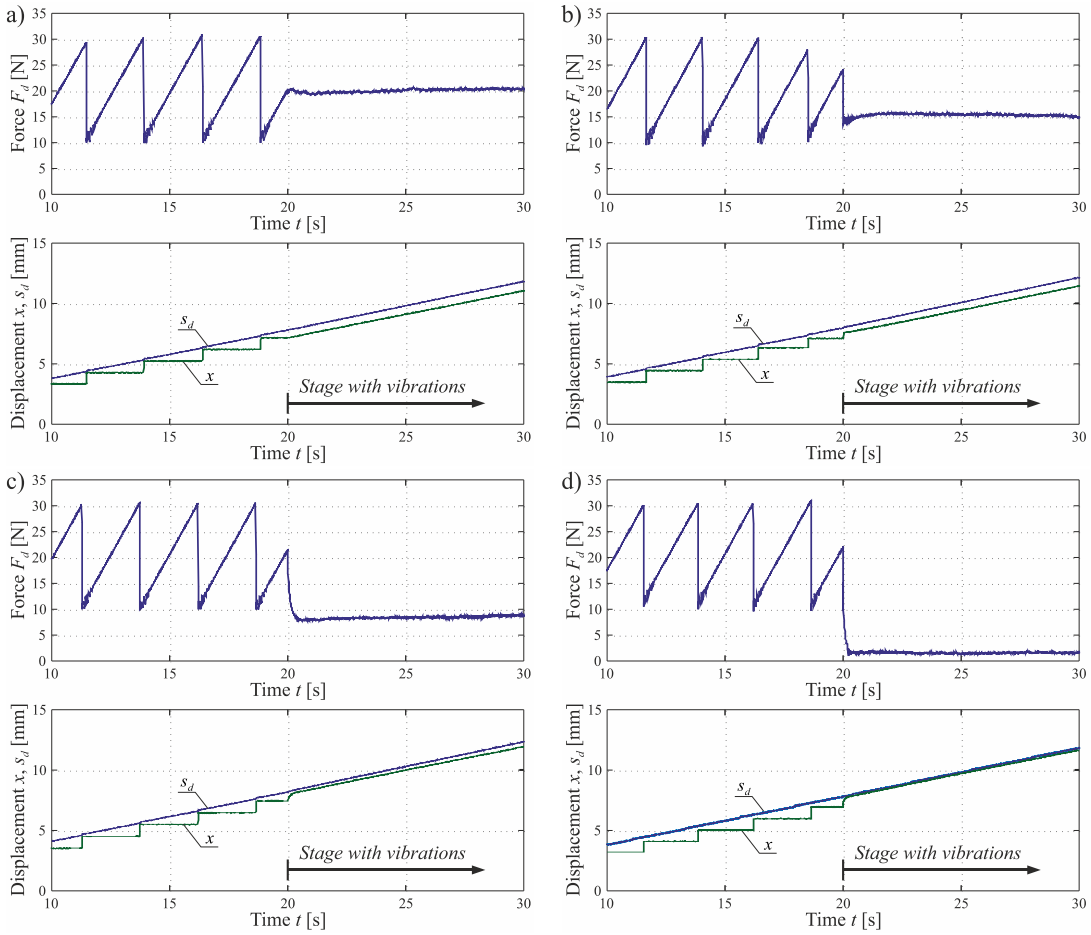

Fig. 7. Experimentally determined waveforms of drive force F_d, displacement of the sliding body x and drive displacement s_d for: (a) v_a = 0.4 mm/s, (b) v_a = 0.8 mm/s, (c) v_a = 2 mm/s and (d) v_a = 6 mm/s; f = 2000 Hz, v_d = 0.4 mm/s

In the second variant, presented in Fig. 7, the amplitude v_a of the vibration velocity was equal to (Fig. 7a) and higher (Fig. 7b,c,d) than the drive velocity v_d. Also, in this case, the tests were performed for four selected v_a values amounting to 0.4, 0.8, 2, and 6 mm/s. From the presented waveforms of the drive force F_d and the position x of the sliding body, it can be seen that, in this variant of tests, the stick-slip phenomenon has been completely eliminated.

In addition, in three cases (Fig. 7b,c,d) where v_a was higher than the drive speed v_d, the induction of tangential vibrations also caused a significant reduction in the drive force necessary to make the body move in a sliding motion and to maintain this movement. This relationship is also confirmed by the results of experimental research by Leus and Gutowski (2011) and Gutowski and Leus (2012) and by other authors (Gao et al., 2016; Kapelke and Seemann, 2018; Littman et al., 2001a, 2001b; Qu et al., 2016; Wang et al., 2016, 2017).The level of reduction of the drive force, as well as the degree of stick-slip elimination, clearly depends on the amplitude v_a of the velocity of the forced vibrations of the substrate and is higher if its value in relation to the speed of sliding is higher.

Abdo and Zaier (2012) reported that a significant impact on the reduction of stick-slip movement has displacement of the sliding specimen in the normal direction to the slip plane, which temporarily reduces the normal pressure at the contact. However, this problem was not analysed in this article according to the main topic because its explanation requires more extensive experimental tests of the possibility of creating normal vibration in sliding motion by the introduction of tangential vibration into the contact zone.

5. SUMMARY

The test stand presented in this article allows to conduct a wide range of experimental studies on the influence of longitudinal tangential vibrations on the stick-slip phenomenon occurring in sliding motion. The change of test variant is connected with the possibility to change the drive speed v_d, the frequency f and amplitude u_o of the forced vibrations, the external load F_z and the stiffness of the drive k_d. The results of the tests presented in this article are only a selected fragment of one of the possible variants of the test.

The conducted experimental analyses have shown that longitudinal tangential vibrations of the substrate on which the slip movement is performed may contribute to the reduction or even complete elimination of the stick-slip phenomenon. The decisive parameter for partial or total elimination of this phenomenon is the value of amplitude of the velocity of vibrations in relation to the nominal speed of movement of the bodies in contact.

For values of v_d, k_d, F_z and f, assumed in this stage of experimental research, in the range where the amplitude of the vibration velocity is lower than the drive velocity, only a gradual reduction of the stick-slip phenomenon occurs. As the v_a value increases, the jump length of the sliding body decreases. If the amplitude of the vibration velocity is equal to or higher than the drive velocity, the

stick-slip phenomenon is completely eliminated. An additional, observable effect in the range for v_a higher than v_d is the reduction of the drive force, where the higher the value of v_a *is*, the greater is the reduction of this force.

REFERENCES

1. **Abdo J., Tahat M., Abouelsoud A.** (2009), The effect of excitation frequencies on stick-slip amplitude, *3rd International Conference on Integrity, Reliability and Failure*, Porto/Portugal, 319-320.
2. **Abdo J., Tahat M., Abouelsoud A., Danish M.** (2010), The effect of frequency of vibration and humidity on the stick-slip amplitude, *International Journal of Mechanics and Materials in Design*, 6(1), 45-51.
3. **Abdo J., Zaier R.** (2012), A novel pin-on-disk machine for stick-slip measurements, *Materials and Manufacturing Processes*, 27, 751-755.
4. **Canudas de Wit C., Olsson H., Aström K.J., Lischinsky P.** (1995), A new model for control of system with frictio, *IEEE Transactions on Automatic Control*, 40(3), 419-425.
5. **F. Aarsnes U.J., Di Meglio F., Shor R.J.** (2018), Avoiding stick slip vibrations in drilling through startup trajectory design, *Journal of Process Control*, 70, 24-35.
6. **Gao H., De Volder M., Cheng T., Bao G., Reynaerts D.** (2016), A pneumatic actuator based on vibration friction reduction with bending longitudinal vibration mode, *Sensors and Actuators A: Physical*, 252, 112-119.
7. **Grudziński K., Warda B.J.** (1993), A study of the influence of chosen tribological factors on the mixed friction characteristics and stick-slip vibrations, *Archives of Mechanical Technology and Automation*, 12, 499-514 (in Polish).
8. **Gutowski P., Leus M.** (2012), The effect of longitudinal tangential vibrations on friction and driving forces in sliding motion, *Tribology International*, 55, 108-118.
9. **Gutowski P., Leus M.** (2015), Computational model for friction force estimation in sliding motion at transverse tangential vibrations of elastic contact support. *Tribology International*, 90, 455-462.
10. **Kapelke S., Seemann W.** (2018), On the effect of longitudinal vibrations on dry friction: Modelling aspects and experimental investigations, *Tribology Letters*, 66(3), 1-11.
11. **Kligerman Y., Varenberg M.** (2014), Elimination of stick-slip motion in sliding of split or rough surface, *Tribology Letters*, 53(2), 395-399.
12. **Kröger M., Neubauer M., Popp K.** (2008), Experimental investigation on the avoidance of self-excited vibrations, *Philosophical Transactions of the Royal Society A: Mathematical, Physical and Engineering Sciences*, 366(1866), 785-810.
13. **Leus M., Gutowski P.** (2011), Practical possibilities of utilization of tangential longitudinal vibrations for controlling the friction force and reduction of drive force in sliding motion, *Mechanics and Mechanical Engineering*, 15(4), 103-113.
14. **Littmann W., Stork H., Wallaschek J.** (2001a), Reduction of friction using piezoelectrically excited ultrasonic vibrations, *Proceedings of the SPIE's 8th Annual International Symposium on Smart Structures and Material*, Billingham, Washington, 302-311.
15. **Littmann W., Stork H., Wallaschek J.** (2001b), Sliding friction in the presence of ultrasonic oscillations: superposition of longitudinal oscillations. *Archive of Applied Mechanics*, 71, 549-54**.**
16. **Mfoumou G.S., Kenmoé G.D., Kofané T.C.** (2019), Computational algorithms of time series for stick-slip dynamics and time-delayed feedback control of chaos for a class of discontinuous friction systems, *Mechanical Systems and Signal Processing*, 119, 399-419.
17. **Mokhtar M.O.A., Younes Y.K., El Mahdy T.H., Attia N.A.** (1998), A theoretical and experimental study on dynamics of sliding bodies with dry conformal contacts, *Wear*, 218(2), 172-178.
18. **Neubauer M., Neuber C-C., Popp K.** (2005), Control of stick-slip vibrations, *Solid Mechanics and its Applications*, 130, 223-232.
19. **Ozaki S., Hashiguchi K.** (2010), Numerical analysis of stick-slip instability by a rate-dependent elastoplastic formulation for friction, *Tribology International*, 43, 2120-2133.
20. **Popov V.L., Starcevic J., Filippov, A.E.** (2010), Influence of ultrasonic in-plane oscillations on static and sliding friction and intrinsic length scale of dry friction processes, *Tribology Letters*, 39(1), 25-30.
21. **Popp K., Rudolph M.** (2003), Avoidance of stick-slip motion by vibration control, *Proceedings in Applied Mathematics and Mechanics*, 3, 120-121.
22. **Popp K., Rudolph M.** (2004), Vibration control to avoid stick-slip motion, *Journal of Vibration and Control*, 10, 1585-1600.
23. **Qiu H., Yang J., Butt S.** (2018), Investigation on bit stick-slip vibration with random friction coefficients, *Journal of Petroleum Science and Engineering*, 164, 127-139.
24. **Qu H., Zhou N., Guo W., Qu J.** (2016), A model of friction reduction with in-plane high-frequency vibration, *Proceedings of the Institution of Mechanical Engineers, Part J: Journal of Engineering Tribology*, 230(8), 962-967.
25. **Rymuza Z.** (1992), The stick-slip phenomenon, *PAK*, 12, 290-295, (in Polish).
26. **Tang L., Zhu X., Qian X., Shi C.** (2017), Effects of weight on bit on torsional stick-slip vibration of oilwell drill string, *Journal of Mechanical Science and Technology*, 31(10), 4589-4597.
27. **Tang L., Zhu X., Shi C., Tang J., Xu D.** (2015), Study of the influences of rotary table speed on stick-slip vibration of the drilling system *Petroleum*, 1(4), 382-387.
28. **Teidelt E., Starcevic J., Popov V.L.** (2012), Influence of ultrasonic oscillation on static and sliding friction, *Tribology Letters*, 48(1), 51-62
29. **Wang P., Ni H., Wang R., Li Z., Wang Y.** (2016), Experimental investigation of the effect of in-plane vibrations on friction for different materials, *Tribology International*, 99, 237-247.
30. **Wang P., Ni H., Wang R., Liu W., Lu S.** (2017), Research on the mechanism of in-plane vibration on friction reduction, *Materials*, 10(9), 1-21.
31. **Zhu X., Tang L., Yang Q.** (2014), A literature review of approaches for stick-slip vibration suppression in oilwell drillstring, *Advances in Mechanical Engineering*, 2014, 967952, 1-17.
32. **Zuleeg J.** (2015), How to measure, prevent, and eliminate stick-slip and noise generation with lubricants, *SAE Technical Paper* 2015-01-2259, 1-7.

sciendo

DOI 10.2478/ama-2019-0008

acta mechanica et automatica, vol.13 no.1 (2019)

PERIODIC TRENDS IN TWO-PHASE FLOW THROUGH A VERTICAL MINICHANNEL: WAVELET AND MULTISCALE ENTROPY ANALYSES BASED ON DIGITAL CAMERA DATA

Grzegorz GÓRSKI[*], Grzegorz LITAK[,***], Romuald MOSDORF[*], Andrzej RYSAK[**]**

g.gorski@pb.edu.pl, g.litak@pollub.pl, r.mosdorf@pb.edu.pl, a.rysak@pollub.pl

[*]Faculty of Mechanical Engineering, Bialystok University of Technology, ul. Wiejska 45C, 15-351 , Bialystok, Poland
[**]Faculty of Mechanical Engineering, Lublin University of Technology, ul. Nadbystrzycka 36, 20-618 Lublin, Poland
[***]Department of Process Control, AGH University of Science and Technology, ul. Mickiewicza 30, 30-059 Krakow, Poland

received 24 March 2018, revised 15 March 2019, accepted 21 March 2019

Abstract: By changing the air and water flow relative rates in the two-phase (air-water) flow through a minichannel, we observe aggregation and partitioning of air bubbles and slugs of different sizes. An air bubble arrangement, which show non-periodic and periodic patterns. The spatiotemporal behaviour was recorded by a digital camera. Multiscale entropy analysis is a method of measuring the time series complexity. The main aim of the paper was testing the possibility of implementation of multiscale entropy for two-phase flow patterns classification. For better understanding, the dynamics of the two-phase flow patterns inside the minichannel histograms and wavelet methods were also used. In particular, we found a clear distinction between bubbles and slugs formations in terms of multiscale entropy. On the other hand, the intermediate region was effected by appearance of both forms in non-periodic and periodic sequences. The preliminary results were confirmed by using histograms and wavelets.

Key words: digital camera data, two-phase flow, patterns identification, multiscale entropy, wavelets

1. INTRODUCTION

Two-phase dynamics is a common issue in many technical minichannel systems of various diameters, ranging from micro- to centimetres. Different properties of the flowing phases lead to the main problems with pressure and temperature control during flows. That problems motivated many works on patterns identification of two-phase flow in minichannels from measurements or modelling (Zhao and Rezkallah, 1993; Wongwises and Pipathattakul, 2006; Chen et al., 2006; Zong et al., 2010; Anjos et al., 2014). More advanced studies on flow patterns were conducted by Wang et al. (2003), who used Hurst and Lyapunov exponents, as well as the correlation dimension. Simultaneous to that investigations, Jin et al. (2003) used the correlation dimension and, additionally, the Kolmogorov entropy. Later, Mosdorf et al. (2005) provided the results of non-linear approaches to the temperature and pressure fluctuations in microchannels. More recently, recurrence statistics were performed to the two-phase flows (Gorski et al., 2015a; 2015b; 2016) by employing a laser-phototransistor light transitivity sensor. These investigations enable to identify the transitions from bubbles to slugs and churn, and conclude on corresponding patterns stabilities. Multiscale character of flows were raised by Fan et al. (2013, 2015), who also used the data of light transmission through a minichannel. Finally, the complex multiscale morphological analysis using electric conductance signals was proposed by Lian et al. (2016).

The main aim of the paper was testing the possibility of implementation of multiscale entropy for the two-phase flow patterns' classification. For better understanding, the dynamics of two-phase flow patterns inside the minichannel histograms and wavelet methods were also used. The concepts of wavelets and multiscale entropy applied directly to the digital camera snapshots (Rysak et al., 2016).

2. EXPERIMENTAL SETUP

We performed the measurements and analysed the related data recorded for different flow patterns (water-air at 21°C) in a circular channel having a diameter of 2 mm. In Fig. 1, the schema of experimental stand is presented. In the conditions of the small diameter minichannel, a special generator of mini bubbles was designed (8). The proportional pressure regulator (Metal Work Regtronic with an accuracy of 1 kPa) was used to maintain the constant overpressure in the supply tank (10 – Fig. 1) – the overpressure was 50 kPa. Flow patterns were recorded using the Phantom v. 1610 digital camera at 5000 fps (1280 × 64 pixels). The amount of air flowing through the minichannel was also measured by laser-phototransistor sensor (3). Data from the sensors was acquired by the acquisition system (Data translation 9804, an accuracy of 1 mV for voltages in the range of -10 V to 10 V), (11) at a sampling rate of 5 kHz.

The measurement results are presented in Fig. 2 (camera snapshots) for changing air volume flow rate q_a {0:00632, 0.1} l/min and changing water volume flow rate q. Note that air bubbles were produced with different shapes depending on the airflow $\mathrm{q_a}$. In the limit of small q_a and large q (Fig. 2a), the air bubbles are of fairly small and variable sizes. Their sizes are increasing with decreasing q (Fig. 2d). On the other hand, for larger (q_a), decreasing q leads to stabilizing of air slugs (elongated bubbles) – see Figs. 3a–d.

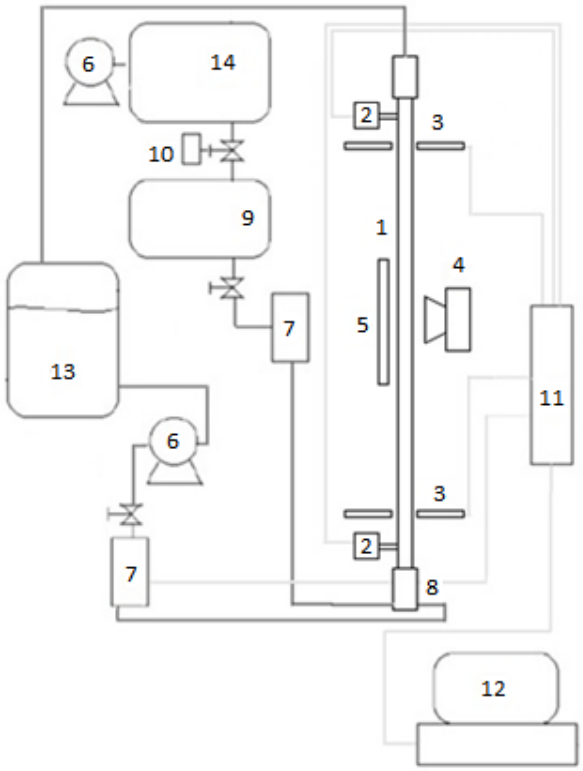

Fig. 1. Experimental setup: 1 – vertical minichannel with a diameter of 3 mm, 2 – pressure sensors (MPX12DP), 3 – laser-phototransistor sensor, 4 – Phantom v. 1610 camera, 5 – lighting, 6 – pumps (air or water), 7 – flow meters, 8 – mini bubbles generator, 9 – air tank, 10 – automatic valve to maintain a constant pressure in the tank 9, 11 – data acquisition station (DT9800), 12 – computer, 13 – water tank, 14 – air tank

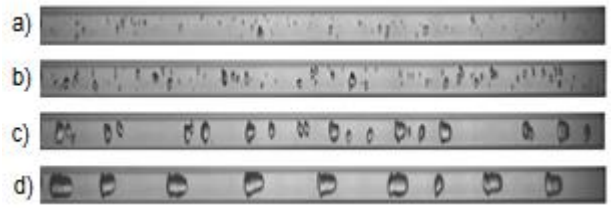

Fig. 2. Photos of the selected flow cases with increasing water volume flow rate q [l/min]: 0.234 (a), 0.173 (b), 0.091 (c), and 0.027 (d), respectively. The air volume flow rate was fixed to q_a = 0:00632 l/min.

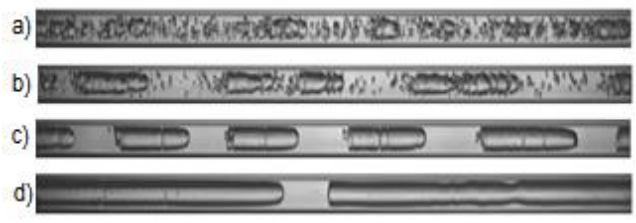

Fig. 3. Photos of the selected flow cases with increasing water volume flow rate q [l/min]: 0.216 (a), 0.145 (b), 0.071 (c), and 0.012 (d), respectively. The air volume flow rate was fixed to q_a = 0.1 l/min.

Following the pioneering image processing techniques (Otsu, 1979; Haralick et al., 1987), we explore the digital camera signal obtained from the bubbles and slugs contours passing through the cross-sectional gate observation (Rysak et al., 2016). Note that in the previous attempts of digital conversion, the contrast was introduced between different phases (Mydlarz-Gabryk et al., 2014; Riano et al., 2015; Ansari and Azadi, 2016). Here, we present the alternative and simpler way with processing pixels of contours between two flowing phases.

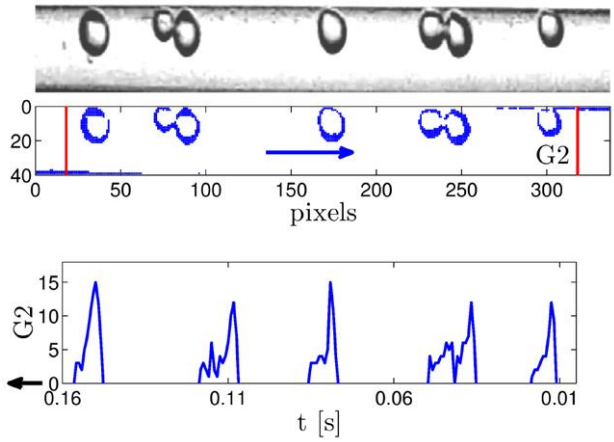

Fig. 4. The digital camera signal was obtained from the bubbles and slugs contours passing through the cross-sectional gate observation G2 (Rysak et al., 2016). Note difference in the horizontal axis orientation.

The contour frames were obtained by converting filtered images to 0–1 values matrices. One of the captured image frames of the two-phase flow is shown in the upper part in Fig. 4. The middle figure shows its contour frame representation. The red line on the right hand side indicates the gate G2, where pixels are counted. The movement of the mixture takes place to the right (arrow). With the laps of time, the structures of the gas flowing through the gate G2 build a time series (as shown in the bottom image in Fig. 4). Consequently, we observe the time series in terms of photo pixels passing through the defined gate.

3. DIGITAL TIME SERIES ANALYSIS

The results of the resulting time series corresponding to the cases presented in Figs. 2 and 3 are presented in Figs. 5 and 6, respectively. Note that q_a = 0 would correspond to single phase (water) flow. Most of the time series looks random (Fig. 5). However, the pattern is changing from single lines representing small bubbles in Fig. 5a and 5b to longer slugs in Fig. 5d. On the way, in Fig. 5c, there is a mixture of these formations, which looks like a chaotic transient (Sen et al., 2008). On the other hand, the longest stable level of 10 pixels corresponds to the slug flow (as shown in Fig. 6 at the lower panel [b]).

Interestingly, one can observe the interesting periodic intermittent (water-air) flow (see Fig. 6 at the middle panels). This is a spatio-temporal self-organization phenomenon of the flow determined by the air-water mixture of fluid and the flow conditions (see Fig. 6c): the flow rates, their viscosity, and the geometry of minichannel. I believe it should be well imitated, which corresponds to a convergence in the bubbles sizes. However, the phase variations (Fig. 6c) confirm that the periodic tendencies are not fully developed and the time series are characterised by only short time correlations.

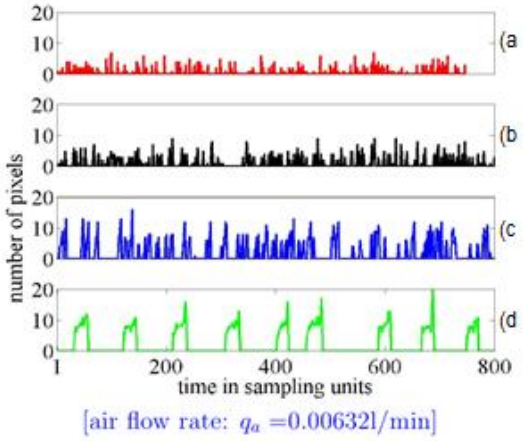

Fig. 5. Time series in terms of number of pixels xi passing through the gate in the central cross-section of the camera view (Fig. 1). The cases presented downward correspond to (a)–(d) in Fig. 2. The sampling time step was 0.2×10^{-3} s. Number of points (range of horizontal axis) was 800.

4. PIXEL STATISTICAL DISTRIBUTIONS – HISTOGRAMS

Distributions of pixels registered by the digital camera can be investigated by histograms. Interestingly, we observe the evolution from the system of air bubbles' deficiency to larger bubbles, and finally the elongated bubbles – slugs. In case of the low amount of air flow q_a = 0.00632 l/min, the small air bubbles are noticeable in a large water space (Fig. 2a–b).

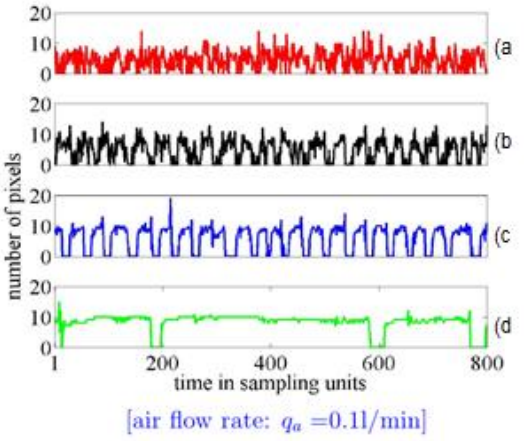

Fig. 6. Time series in terms of number of pixels xi passing through the gate in the central cross-section of the camera view (Fig. 1). The cases presented downward correspond to (a)–(d) in Fig. 3, respectively. The sampling time step was 0.2×10^{-3} s. Number of points (range of horizontal axis) was 800.

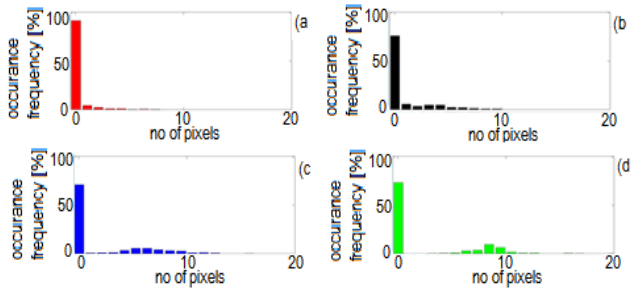

Fig. 7. Histograms for the cases presented in Fig. 2

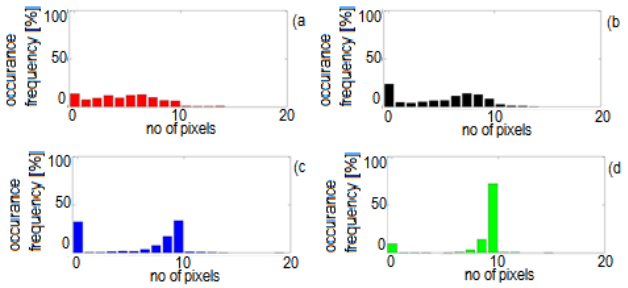

Fig. 8. Histograms for the cases presented in Fig. 3

Consequently, these cases are accompanied by a fairly large maximum in histograms with 0 pixel (Figs. 7a, b), which is clearly visible. By decreasing the water flow, we observe two maxima in histograms (Figs. 7c, d) with continued domination of 0 pixel peak. Finally, for higher amount of air flow, the 0 pixel probability peak is strongly reduced (Figs. 8a–8d). Additionally, the cases in Figs. 8c, d, with the strong increase in the longer length occurrence frequency of pixel numbers, reflects the presence of slugs.

5. WAVELET ANALYSIS

A statistical approach of the pixels counting presented in the last section gave the idea of the distribution of bubbles and slugs in terms of the appearance of their characteristic lengths. On the other hand, bubbles and slugs can appear in a random way or with a given periodicity. To clarify this point, we decided to use continuous wavelets, which can distinguish the short interval periodic self-organizing structures. This is an alternative method to the earlier proposed recurrence studies (Gorski et al., 2015b), which were conducted for laser-photoresistor transitivity data (Gorski et al., 2015b).

In the current study, to show the emerging periods, we present the wavelet analysis of the results. We study the time series of pixels *Np*(*t*) given by the continuous wavelet transformation (CWT) (Kumar and Foufoula-Georgiou, 1997; Torrence and Compo, 1998; Lonkwic et al., 2017). The corresponding continuous wavelet transform with respect to the wavelet function $\psi(.)$ is defined as follows:

$$W_{s,n}(Np) = \sum_{i=1}^{N} \frac{1}{s} \psi\left(\frac{i-n}{s}\right) \frac{(Np(t_i)-\langle Np\rangle)}{\sigma_{Np}}, \quad (1)$$

where: $\langle Np\rangle$ and σNp are the averages and standard deviations of pixel number registered, respectively. Finally, the wavelet ψ (.) is referred to as the mother wavelet, and the letters s and n denote the scale and the time indices, respectively. The wavelet power spectrum (WPS) of the Np time series is defined as the square modulus of the CWT:

$$P_w = \left|W_{s,n}\right|^2. \quad (2)$$

In the present calculations, we used a complex Morlet wavelet as the mother wavelet. The Morlet wavelet consists of a plane wave modulated by a Gaussian function and it is described by:

$$\psi(\eta) = \pi^{-1/4} e^{i\theta_0 \eta} e^{-\eta^2/2}, \quad (3)$$

where: θ_0 is the centre frequency, also referred to as the order of the wavelet, and η is a renormalized time variable. Namely, θ_0 defines the number of oscillations in the wavelet and thus controls the time/frequency resolutions. In our analysis, we used θ_0 = 6,

which provides a good balance between the time and frequency resolutions. Also, for the a.m. choice, the scale is approximately equal to the period, and therefore, the terms scale and period can be interchanged for interpreting the results. For general discussion, see: Kumar and Foufoula-Georgiou (1997), Torrence and Compo (1998) and Lonkwic et al. (2017). The corresponding results of CWT as the wavelet power spectra are presented in Figs. 9 and 10. Using these techniques, it was possible to select the regions of periodic formations. On the logarithmic colour scale, these regions are shown by the dark red–brown colour. For instance, Figs. 10b and 10c show clear periods with around 35 sampling times. A less spectacular period of about 80 sampling times is also visible in Fig. 9d. Other cases are more random showing much shorter periods.

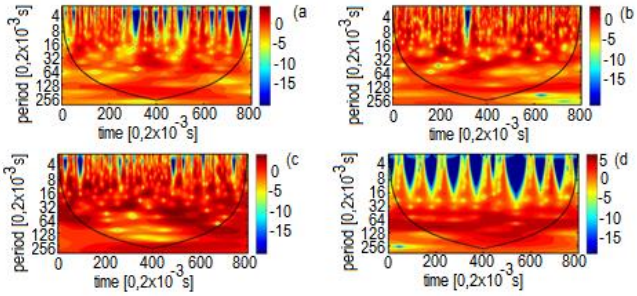

Fig. 9. Wavelets for the cases presented in Fig. 2. Colours, from blue to red, corresponds to increase in the wavelet power. The black U-like curve limit the internal region of importance.

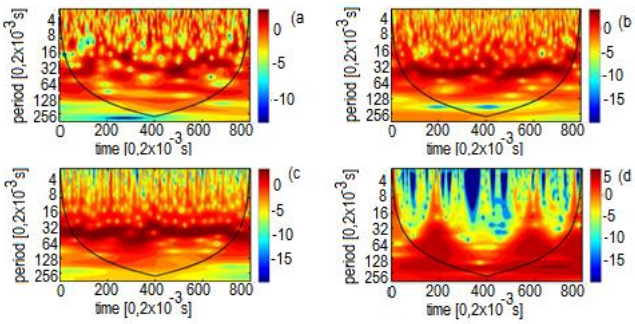

Fig. 10. Wavelets for the cases presented in Fig. 3. Colours, from blue to red, corresponds to increase in the wavelet power. The black U-like curve limit the internal region of importance.

6. MULTISCALE ENTROPY

To improve the understanding of the behaviour of complex systems that manifest themselves in non-linear behaviour, the multiscale entropy (Costa et al., 2003; 2005) analysis is becoming increasingly more popular (see: Borowiec et al., 2010; Litak et al., 2011; Wu et al., 2013, Borowiec et al., 2014). This method provides, for measured signals, a relative level of complexity of finite length time series. Unfortunately, there is no consensus of the complexity definition, but it is combined with 'meaningful structural richness' (Grassberger, 1991) contained over multiple spatio-temporal correlations.

The concept of multi-scale entropy (MSE) (Costa et al., 2003, 2005) is based on the coarse-graining procedure that uses a coarse-grained time series, as an average of the original data points within non-overlapping windows by increasing the scale factor τ according to the following formula (see the cases τ = 2 and n in Fig. 11):

$$x_j^{(\tau)} = \frac{1}{\tau}\sum_{i=(j-1)\tau+1}^{j\tau} x_i, \qquad (4)$$

where x_i is a raw one-dimensional acceleration time series $x = \{x_1, x_2, \ldots, x_N\}$. In this approach for each scale factor τ, the MSE calculation based on the time series of the coarse-grained $x_j(\tau)$:

$$\mathrm{MSE}(x, \tau, n, r) = SampEn(x^{(\tau)}, m, r), \qquad (5)$$

where m = 2 is the pattern length and r is the similarity (tolerance) criterion and is usually chosen to be $r < \sigma(x)$,[25] here σ(x) is the standard deviation of the original time series and $x(1)i = x_i$.

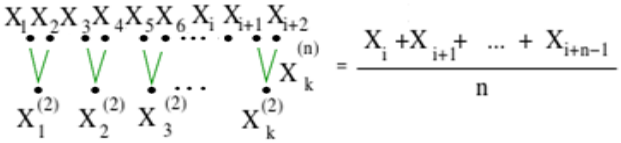

Fig. 11. Schema of multiscale entropy calculation. Here, X_i denotes the i-th value on the time series shown in Fig. 5.

To estimate *SampEn*($x^{(\tau)}, m, r$) from Eq. 6 (see also Fig. 11), we count the number of vector pairs denoted by $x^{(\tau)}{}_i$ and $x^{(\tau)}{}_j$ in the time series of length m and $m+1$ having distance $\mathrm{d}[x^{(\tau)}{}_i, x^{(\tau)}{}_j] < r$. We denote them by P_m and P_{m+1}, respectively. Finally, we define the sample entropy to be Richman and Moorman (2000):

$$SampEn(x^{(\tau)}, m, r) = -\log\frac{P_{m+1}}{P_m}. \qquad (6)$$

Strictly speaking, it is the minus of the logarithm of the conditional probability that the two sequences with a tolerance r form points that remain within r of each other at the next point. Continuing the research activity, Wu et al. (2013) introduced the concept of a composite multi-scale entropy (CMSE), which for higher scale factor provides entropy more reliably than the usual multi-scale entropy by including multiple [k] combinations of neighbour points. The prescribed algorithm for CMSE calculations is the following formula:

$$CMSE(x, \tau, m, r) = \frac{1}{\tau}\sum_{k=1}^{\tau} SampEn(x^{(\tau)}[k], m, r). \quad (7)$$

The results of the complexity measure in terms of CMSE estimations for all the time series of our consideration (Figs. 5a, b) are presented in Fig. 12 for smaller q_a and in Fig. 13 for larger q_a. All of the results indicate rather non-periodic character of the flow phenomenon. However, comparing the results (Figs. 13a–13c) with the associated photos (see Figs. 3a–3c) and time series in Figs. 6a–6c), we can draw conclusions that complexity (expressed by turbulence flow) level is the highest at Fig. 13b. This is the intermediate region of coexistence of bubbles and slugs. Note also that Figs 12a–12d show a similar structure with shifted maximum to the right hand side for decreasing q_a. This change is related to the size of bubbles (and possibly their velocities) appearing in the flow (Fig. 2). In contrast, Figs. 13a–13d show a spectacular transition, which is also visible in Fig. 3. The bubble like flow is experiencing qualitative metamorphosis and the

bubbles flow is changing to the slugs flow. In the entropy picture, this leads to the change of negative to positive inclination (compare Figs. 13a to 13d). Such an inclination could be a signal of oversampling (Borowiec et al., 2010); however, in our case, this effect is of physical origin – the increasing correlation time due to appearance of long slugs (see Fig. 3d).

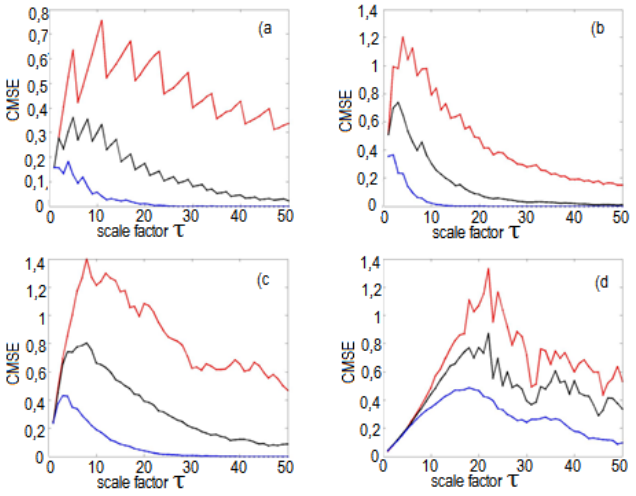

Fig. 12. The Multiscale entropy for the cases presented in Fig. 2. Colours corresponds to different similarity factors: red curve – $r = 0.25\sigma(x)$, black curve – $r = 0.5\sigma(x)$, blue curve – $r = 1.0\sigma(x)$ (where $\sigma(x)$ denotes the corresponding standard deviation of the original time series).

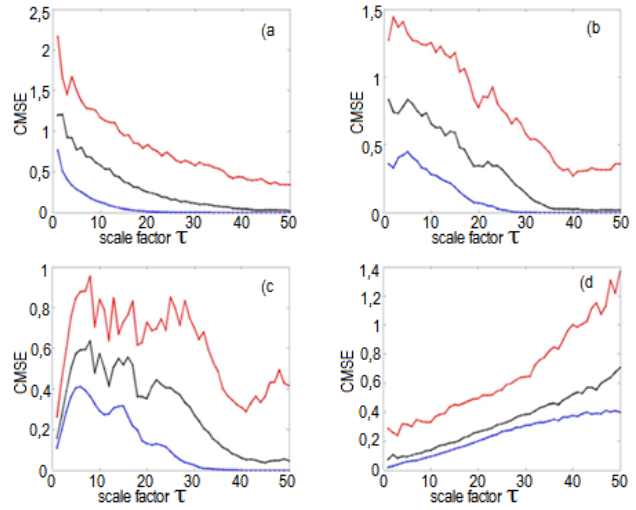

Fig. 13. The Multiscale entropy for the cases presented in Fig. 3. Colours corresponds to different similarity factors: red curve – $r = 0.25\sigma(x)$, black curve – $r = 0.5\sigma(x)$, blue curve – $r = 1.0\sigma(x)$ (where $\sigma(x)$ denotes the corresponding standard deviation of the original time series).

7. CONCLUSIONS

Analysis of time series and further application of the multiscale entropy made possible to distinguish the particular patterns of bubbles and slugs creations on the basis of multiscale entropy. The changes in patterns were caused by the stability of larger size air bubbles or slugs, which was increased for various values of flow rates of air (q_a) and water (q). In the limit of small air volume flow rate q_a, there was a disturbed noisy flow of water with small bubbles. Moreover, in this limit, the bubbles were characterized by different sizes and velocities.

For larger q_a, we identified aggregation of air bubbles of different sizes to create stable air slugs. Formation of bubbles and slugs was clearly signalled by the histograms. By means of wavelet analysis, we observed the conditions of periodic interchange in the flow of water-air mixture. Finally, slugs' appearance was accompanied by the change of negative to positive inclination in entropy. The present results based on the digital camera data are much more transparent as compared to our previous attempts, where we used the laser transmittivity time series (Gorski et al., 2015). In the previous case, increasing the scattering of the laser light occurred by passing through the owing corrugated surfaces of elongated bubbles. In this article, we focused on an automatic two-phase flow identification and related bifurcations in shape formations. Therefore, the identification of bubbles of 3D shapes (Mukin, 2016) is beyond this study.

REFERENCES

1. **Anjos G.R., Borhani N., Mangiavacchi N., Thome J. R.** (2014), A 3D moving mesh Finite Element Method for two-phase flows, *Journal of Computational Physics*, 270, 366–377.
2. **Ansari M.R., Azadi R.** (2016), Effect of diameter and axial location on upward gas-liquid two-phase flow patterns in intermediate-scale vertical tubes, *Annals of Nuclear Energy*, 94, 530–540.
3. **Borowiec M., Rysak A., Betts D.H., Bowen C.R., Kim H.A., Litak G.** (2014), Complex response of a bistable laminated plate: Multiscale entropy analysis, *European Physical Journal Plus*, 129, 211.
4. **Borowiec M., Sen A.K., Litak G., Hunicz J., Koszalka G., Niewczas A.** (2010), Vibrations of a vehicle excited by real road profiles, *Forschung im Ingenieurwesen*, 74, 99–109.
5. **Chen L., Tian Y.S., Karayiannis T.G.** (2006), The e_ect of tube diameter on vertical two-phase flow regimes in small tubes, *International Journal of Heat and Mass Transfer*, 49, 4220–4230.
6. **Costa M., Goldberger A.L., Peng C.-K.** (2005), Multiscale entropy analysis of biological signal, *Physical Review*, E 71, 021906.
7. **Costa M., Peng C.-K., Goldberger A.L., Hausdorff J.M.** (2003), Multiscale entropy analysis of human gait dynamics, *Physica*, A 330, 53–60.
8. **Fan C., Li H., Ren X.** (2015), The order recurrence quantification analysis of the characteristics of two-phase flow pattern based on multi-scale decomposition, *Transactions of the Institute of Measurement and Control*, 37, 793–804.
9. **Fan C.-L., Jin N.-D., Chen X.-T., Gao Z.-K.** (2013), Multi-scale permutation entropy, A complexity measure for discriminating two-phase flow dynamics, *Chinese Physics Letters*, 30, 090501.
10. **Gorski G., Litak G., Mosdorf R., Rysak A.** (2015b), Self-aggregation phenomenon and stable flow conditions in a two-phase flow through a minichanel, *Zeitschrift fuer Naturforschung*, A 70, 843–849.
11. **Gorski G., Litak G., Mosdorf R., Rysak A.** (2016), Dynamics of a two-phase flow through a minichannel, Transition from churn to slug flow, *European Physical Journal Plus,* 131, 111.
12. **Gorski G., Litak G., Mosdorf R., Rysak A.,** (2015a), Two phase flow bifurcation due to turbulence, Transition from slugs to bubbles, *European Physical Journal*, B 88, 239.
13. **Gorski G., Litak G., Mosdorf R., Rysak R.** (2015), Dynamics of two-phase flow through a minichannel, Fourier and multiscale entropy analyses, *Applied Mechanics and Materials*, 791, 217–223.
14. **Grassberger P.** (1991), Information and complexity measures in dynamical systems, In: Atmanspacher H., Scheingraber H. (Eds.), *Information Dynamics*, New York, Plenum Press, 15–33.
15. **Haralick R.M., Srernberg S.R., Zhuang X.** (1987), Image analysis using mathematical morphology, *IEEE Transactions on Pattern Analysis and Machine Intelligence*, PAMI-9, 532–550.

16. **Jin N.D., Nie X.B., Ren Y.Y., Liu X.B.** (2003), Characterization of oil/water two-phase flow patterns based on nonlinear time series analysis, *Flow Measurement and Instrumentation* 14, 169–175.
17. **Kumar P., Foufoula-Georgiou E.** (1997), Wavelet analysis for geophysical applications, *Reviews of Geophysics*, 35, 385–412.
18. **Lian E.Y., Ren Y.Y., Han Y.F., Liu W.X,. Jin N.D., Zhao J.Y.** (2016), Multi-Scale morphological analysis of conductance signals in vertical upward gas-liquid two-phase flow, *Zeitschrift fuer Naturforschung*, A 71, 1031–1052.
19. **Litak G., Syta A., Rusinek R.** (2011), Dynamical changes during composite milling, recurrence and multiscale entropy analysis. *International Journal of Advanced Manufacturing Technology*, 56, 445–453.
20. **Lonkwic P., Łygas K., Wolszczak P., Molski S., Litak G.** (2017), Braking deceleration variability of progressive safety gears using statistical and wavelet analyses, *Measurement* , 110, 90–97.
21. **Mosdorf R., Cheng P., Wu H.Y., Shoji M.** (2005), Non-linear analyses of flow boiling in microchannels, *International Journal of Heat and Mass Transfer,* 48, 4667–4683.
22. **Mukin R.V.** (2016), Bubble reconstruction method for wiremesh sensors measurements, *Exp. Fluids*, 57, 133.
23. **Mydlarz-Gabryk K., Pietrzak M., Troniewski L.** (2014), Study on oil-water two-phase upflow in vertical pipe, *Journal of Petroleum Science and Engineering*, 117, 28–36.
24. **Otsu N.** (1979), A threshold selection method from gray-level histograms, *IEEE Transactions on Systems, Man, and Cybernetics*, SMC-9, 62–66.
25. **Riano A.B., Rodriguez I.H., Bannwart A.C., Rodriguez O.M.H.** (2015), Film thickness measurement in oil-water pipe flow using image processing technique, *Experimental Thermal and Fluid Science*, 68, 330–338.
26. **Richman JS, Moorman JR** (2000), Physiological time-series analysis using approximate entropy and sample entropy. American Journal of Physiology, *Heart and Circulatory Physiology*, 278, H2039–H2049.
27. **Rysak A., Litak G., Mosdorf R., Gorski G.** (2016), Investigation of two-phase flow patterns by analysis of Eulerian space-time correlations*, International Journal of Multi-phase Flow*, 85, 23–37.
28. **Sen A.K., Litak G., Taccani R., Radu R.,** (2008), Wavelet analysis of cycle-to-cycle pressure variations in an internal combustion engine Chaos, *Solitons & Fractals*, 38, 886–893.
29. **Torrence C., Compo G.P.** (1998), A practical guide to wavelet analysis, *Bull. Amer. Meteor. Soc.*, 79, 61–78.
30. **Wang S.F., Mosdorf R., Shoji M.** (2003), Nonlinear analysis on uctuation feature of two-phase flow through a T-junction, *International Journal of Heat and Mass Transfer*, 46, 1519–1528.
31. **Wongwises S., Pipathattakul M.** (2006), Flow pattern, pressure drop and void fraction of two-phase gas-liquid flow in an inclined narrow annular channel, *Experimental Thermal and Fluid Science* 30, 345–354.
32. **Wu S.-D., Wu C.-W., Lin S.-G., Wang C.-C., Lee K.-Y.** (2013), Time series analysis using composite multiscale entropy, *Entropy*, 15, 1069–1084.
33. **Zhao L., Rezkallah K.S.** (1993), Gasliquid flow patterns at microgravity conditions, *International Journal Multiphase Flow*, 19, 751–763.
34. **Zong Y.-B., Jin N.D., Wang Z.-Y., Gao Z.-K., Wang C.** (2010), Nonlinear dynamic analysis of large diameter inclined oil-water two phase flow pattern, *International Journal of Multiphase Flow*, 36, 166–183.

Acknowledgments: The presented research was funded by the National Science Centre, Poland – the number of decision UMO.2017/27/B/ST8/02905.

sciendo

DOI 10.2478/ama-2019-0009

acta mechanica et automatica, vol.13 no.1 (2019)

RESEARCH ON THE PROPERTIES OF Co-TiC AND Ni-TiC HIP-SINTERED ALLOYS

Tetiana CHEREPOVA,[**] Galyna DMITRIEVA,[**] Oleksandr TISOV,[*] Oleksandr DUKHOTA,[*] Myroslav KINDRACHUK[*]

[*]Engineering Department, Aerospace Institute, National Aviation University, 1 Kosmonavta Komarova Ave., UA-03058, Kyiv, Ukraine
[**]G.V. Kurdyumov Institute for Metal Physics, of N.A.S. of Ukraine, 36 Academician Vernadsky Boulevard, UA-03142 Kyiv, Ukraine

cherepova_ts@meta.ua, dmytrievaGP@nas.gov.ua, tisov@nau.edu.ua, zlpat@nau.edu.ua, nau12@ukr.net

received 13 April 2018, revised 22 March 2019, accepted 27 March 2019

Abstract: Three types of sintered alloys were fabricated based on cobalt, nickel and high-temperature alloy ZhS32-VI matrix with titanium carbide strengthening phase. TiC content was in a range of 30–50 vol. %. The melting temperatures of alloys are higher than 1320°C, and they may undergo undamaged through all technological procedures together with turbine blades, including soldering and outgassing. DSC analyses indicates no additional thermal effects until melting, which confirms their structural stability. The examinations of microstructure revealed three types of constituents – TiC particles, matrix solid solution and blow outs – structural defects having negative effects on all the studied properties. It was found that heat resistance of nickel based sintered alloys at the temperature of 1100°C is superior as compared with the alloys based on cobalt and alloy ZhS32-VI. It has been established that wear resistance in conditions of fretting wear at temperatures of 20, 850, 950 and 1050°C of sintered alloy with ZhS32-VI matrix is mostly superior as compared with the other alloys. The properties of produced alloys allow to use them for manufacturing of components of friction couples operating in conditions of high temperature fretting wear, including protective pads of turbine blades top shrouds contact faces.

Key words: Cobalt, nickel, titanium carbide, sintered alloys, heat resistance, wear resistance, melting temperature

1. INTRODUCTION

The problems of improving power, reliability and durability are the particular focus areas of designing, operation and repair of aircraft gas turbine engines. Their long service life is strongly related to wear resistance of the contact surfaces of turbine rotor blades. They are continuously affected by high temperature, heavy loads, high rates of heating and cooling and corrosion-inducing products of fuel combustion. After prolonged use, turbine blades are usually worn out at the contacting surface of blade shrouds. The effective method to improve their wear resistance is deposition of a wear resistant material to the surface of blade shroud (Tretiachenko et al, 1975).

New generation engines should have increased power, weight-to-power efficiency and reduced fuel consumption. This is achieved through technological methods, and particularly by increasing the fuel combustion temperature. In turn, all this leads to increased loading (mechanical and thermal) of gas turbine engine (GTE) components, reducing their service life. To overcome the arising problems, new materials should be produced. Their key properties are heat resistance, mechanical (compression and shear) strength and fretting resistance. They should comply with a set of requirements of engine manufacturers (Leontiev et al, 2006).

As of today, one of the methods used for Motor Sich engines is the use of cast eutectic alloys as a material for various cladding processes. They are applied to the shroud friction surface. Namely, the cobalt based alloys XTH-61 and XTH-62 (Dmytrieva et al, 2015, Cherepova et al, 2014) are the most widely used.

These alloys are strengthened by NbC particles. Coarser particles – proeutectic crystals, fine particles – a product of eutectic transition. The cobalt matrix is reinforced by macro and micro carbide particles simultaneously, providing a combined strengthening mechanism. Wear resistance of this type of natural composites is dependent on matrix mechanical strength, type of reinforcement and components ratio. Generally, increasing of carbide amount promotes improvement of wear resistance. However, the higher amount of carbides produces higher stresses in matrix material. In conditions of high temperature, this may cause matrix material softening, and then, sintered alloy will not be able to perform its task.

The matrix of these alloys has acceptable heat resistance, but not high enough carbides content. Unfortunately, the amount of carbides in cast alloy is limited: increasing leads to coarsening of carbide grain and embrittlement. Further improvement of wear resistance is possible by methods of powder metallurgy. It allows precise control of both amount and size of carbides. As a matrix material, authors decided to use cobalt and nickel based heat resistant alloys (nickel and cobalt alloyed with chromium, iron and aluminium), and one more alloy – complex high-temperature alloy ZhS32-VI. As a strengthening phase, titanium carbide was selected. Produced sintered alloys (HIP) have superior wear resistance if compared with the above mentioned cast alloys. In addition, the ratio of the components and the size of the carbides may be varied in the broad range of values. Levashov et al. (2003) conducted a good research on the properties of Nickel alloy KhN70Yu+TiC sintered material. In this research, the matrix material was alloyed with chromium, aluminium and iron, but in lesser amounts compared to our experimental Ni-matrix. At the same time, KhN70Yu+TiC sintered material was strengthened with γ' precipitates, as in alloy ZhS32-VI. Also, they reported considerable effect of nanomodification by ZrO_2, Al_2O_3, W, WC, WC–Co, NbC, and Si_3N_4 on the structure and mechanical properties of the

sintered material. Shuster et al. (2016) studied the tribological properties of TiC+ ZhS6U (nickel based alloy) cermet in dry sliding (ball-on-disk) at room temperature. They reported good wear resistance of the material, especially if it is additionally coated with TiC or TiN layer, preventing outcropping of TiC particles from the test piece. Unfortunately, no high-temperature tests were made.

TiC-particles are widely used for the strengthening of structural materials. This may be both bulk and surface strengthening. One of the methods is laser melting of preplaced powder material on the surface of AISI 304 steel part (Chinmaya and Manoj, 2015). TiC with 10–14 μm grain size was used. Laser provides good bonding of preplaced material components and adhesion of the coating to substrate. Cladding of TiC-Co composite coating on the surface of 2Cr13 steel was done by Wei, 2012. He used the coating to increase the useful life of various engineering products, including moulds and turbine blades. Coating had a complex structure with several layers distinguished. The substrate was self-hardened, followed by bonding and transition zones. The cladding layer consisted of oversaturated cobalt dendrites with dispersed TiC particles. For steels, additional strengthening effect provided by self-hardening (depending on steel grade) may be achieved. But, in case of superalloys, this will change the composition and structure of the surface layer (as a result of interdiffusion and melt mixing), but this is not very much expected.

Steel 316L is also a very popular material as a matrix for TiC reinforced MMC's. Chukwuma et al., 2016. Production technique – melt infiltration. TiC contend was 70–90 vol. %, grain size 4–10 μm. Sliding wear tests indicated a trade-off between TiC grain size and matrix-to-filler ratio. Coarser grain size promoted higher specific wear rate, increasing the binder content increased wear rate. Also, the formation of tribolayer with high O content was revealed. The predominant wear mechanism on the initial stage – two-body abrasive wear, being followed by three-body abrasive wear. But, at higher temperatures (which was not studied in the considered research), a tribo-chemical friction-induced layer will be formed in the early period of friction, and may protect the material from carbides spallation and abrasive action of nonoxidized TiC grain fragments. Sakamoto et al., 2015 used 2 wt. % TiC nanoparticles to significantly enhance the mechanical properties of 316L austenitic stainless steel.

TiC-Co composites were studied by Sun-A Jung et al., 2015. The specimens were prepared by using the combination of high energy milling followed by liquid phase sintering. The TiC grain size was 7–10 μm. The importance of grain of TiC and matrix material were highlighted. Namely, fine powders of Co inhibit the TiC grain growth during sintering. Unfortunately, the authors did not do any tribological examinations. Karantzalis et al., 2013, fabricated the Co and Co-based composites reinforced by TiC particles. They used the method of vacuum arc melting to fuse the alloy constituents. Larger amount of TiC promoted coarsening of its grains. The sliding wear test gave promising results.

Another Co-TiC sintered alloy was studied by Jung et al. (2015). Modification of powder starting material with nanosized Co powder allowed to decrease the sintering temperature. Obtained alloy has good thermal stability and mechanical properties, and is reported to be harder than analogical Ni-based alloy, which is in good agreement with the current paper.

Anasori et al., 2014, 2016 reported an excellent damping capacity of Mg-alloys bonded carbides. They studied the energy absorption of alloys with 5, 20 and 50% (vol.) of TiC and Ti_2AlC. The favourable size of particulate reinforcements is 5–15 μm. The effect of damping is achieved by inherent damping capacity of materials, area of matrix-carbide interface, dissimilarity of heat expansion coefficient. This increases the amount of dislocations. So, we believe that 'crashed' carbide particles will provide better energy absorption compared to 'as cast' carbides, and better relief for friction-induced stresses.

Zhang at el, 2000, studied the microstructure and mechanical properties of combustion synthesized and hot compacted gradient TiC-Ni coatings. Ni content wary from 10 to 50 wt. %. The average size of TiC grain was (according to the microstructures published) 1–10 μm and is dependent on nickel content (more nickel – finer TiC grain). Maximum mechanical properties are observed when Ni content is 20–30 wt. %.

Bin et al., 2013 studied the microstructure and tribological behaviour of TiC reinforced nickel-based alloy. They report about decreasing trend of friction coefficient when the content of TiC particles rises up to 30%. At the same time, the wear rate reduces by a value of one third. Further increase of TiC content worsens the tribological behaviour of the composite. They also report about a critical load of about 10–12 MPa when the transition from slight adhesion wear to severe abrasive wear as a result of desquamation of hard tribolayer and material constituents.

Bin et al., 2013, also found that TiC particles reduce friction coefficient and wear losses of Ni-based alloy. The main wear mechanism is micro-cutting. The increase in temperature up to 300°C intensifies the adhesion interaction and increases the wear loss from 4 to 7 mg. This is not very understandable because 15% Cr alloyed Ni usually has better or at least similar wear resistance if compared with the room temperature test results. The reason of this, as we think, is in the use of 7005 aluminium alloy as a substrate for TiC-Ni plasma spray coating. It's load carrying capacity at 300°C is reduced. Yuxin et al., 2009, used direct laser fabrication technique to fabricate 20 to 60 vol. % TiC reinforced Ni-based material. They highlight enhanced wear resistance as the TiC content rises.

Shokat et al., 2015, studied the spark plasma sintering method fabricated in situ Ni-TiC coating. The resultant coating had a structure of Ni matrix strengthened by about 40 vol. % of TiC nanoparticles. Authors, unfortunately, did not study the mechanical properties of the obtained coating, except hardness. Wear tests also were not conducted.

TiC is also used to strengthen aluminium-based alloys. Baskaran et al., 2015 studied the friction behaviour of high strength heat treatable aluminium alloy 7075 with the addition of 4 or 8% of TiC to the material. Unfortunately, the authors omitted the temper state of the alloy being examined. So, the strengthening of precipitation-hardened alloys by TiC is also being done.

Taoyuan Ouyang et al., 2016, highlight the property of TiC particles to release TiO_2 oxide playing role of healing agent. This is observed only at high temperatures, and the preoxidation of the surface may be used demonstrating about 29% better oxidation resistance. Thus, MMC's containing TiC particles may have self-healing effect at high temperature friction and fretting interaction.

Having summarized the above material, the following figure-outs have been made:

- TiC is a very promising material to be used as strengthening phase in the production of MMC's for various friction applications. They have good wear resistance in dry sliding friction. As matrix material, many metals and alloys are used, including cobalt, nickel, magnesium, aluminium alloys and steels.
- Most scientists did the wear assessments of Me-TiC composites at room temperatures in conditions of dry sliding friction.

The results of fretting-wear tests are hardly available in the opened literature. The same refers to the high temperature fretting testing of these materials. The heat resistance and high temperature oxidation behaviour of the mentioned composites is also not highlighted.

- Most of the authors have produced composites by sintering techniques. The volume fraction of carbides is 40–60% for most studies. Microstructural examinations indicate good mixing and uniform distribution of alloying elements and carbide particles in matrix material.
- Depending on the type of material and test conditions, increasing of TiC content to high values may have both beneficial (Chukwuma et al., 2016) or adverse effect (Bin et al., 2013). But, it should be mentioned that reinforcing metal matrix by TiC has a desired effect on friction behaviour at an individual level for each system matrix-to-filler ratios.

For the current research, we decided to cover the following issues:

- to produce MMC's based on nickel and cobalt alloyed matrices having the same alloying system; precipitation-strengthened alloys may also be modified by TiC particles, and for our research we used nickel-based alloy ZhS32-VI
- to study the properties of fabricated alloys by doing microstructure examinations of alloys and assessments of their wear resistance in conditions of high temperature fretting (up to 1050°C); studying their thermodynamic stability and high temperature oxidation behaviour
- to assess the possibility of using these materials for the protection of GTE turbine blades as bonded plates to the surface of top shroud contact face

Current work presents the results of examinations of basic properties of sintered alloys with heat resistant matrix and titanium carbide as a strengthening phase; basically: melting point, heat resistance at maximum possible temperature and wear resistance in conditions of high temperature fretting wear. The main objective of the article is to make a presentation of these materials as future aerospace materials.

2. MATERIALS AND METHODOLOGY OF RESEARCH

The objects of the work are three types of alloys. First, sintered alloys using powders of cobalt, titanium carbide and alloying elements – chromium, iron and nickel. Second, the same components, except cobalt substituted with nickel. As a matrix material for the third type of alloys, a high-temperature precipitation hardening nickel-based alloy ZhS32-VI was used, the filler is the same as for the other two alloys – titanium carbide. The specimens of the alloys were produced by HIP method with SPD-120 equipment, utilizing graphite moulds and induction heating. The air was replaced by CO to avoid the oxidation of unwanted components. The particle size of used powders was 5–20 μm: cobalt powder PK-1U (total impurities up to 0.65%), nickel powder of PNE-1 grade (99.9 % of Ni content), chromium PACh-99H5, iron PIV1, aluminium PA-0 and alloy ZhS32-VI (OST 1.90.126-85). Chemical composition of the materials for matrix alloy production is given in Tab. 1. Titanium carbide TiC (according to standard TU 06173-74) with particle size 5–10 μm was used as the strengthening phase of metal matrix composites being studied.

For alloys of 1st and 2nd type, in order to get the required level of heat resistance, alloying elements (solved in nickel or cobalt) were selected analogically to an alloy XTN-62, except tungsten. The solid solution strengthening effect of tungsten was balanced by adding sufficient amount of TiC. To consume the undesired carbon in TiC grains (about 1.5%) and to avoid formation of other carbides, a precisely measured amount of titanium hydrate was used.

Components of the alloys were mixed with alcohol in planetary ball mill for 2 hours, and after this, the prepared mixture was dried. Premixed components then were placed in a die mould with initial pressure 20 kN applied. Then, the die mould was placed into an induction heater and was heated up to 1000°C. This pre-treatment allows to burn oxygen and to get CO (carbon monoxide) protective atmosphere during burning of graphite. The rate of temperature rise was 50°C/min. The temperature was measured by optical pyrometer 'Promin' with accuracy ± 20°C. The best results of compaction were obtained when the temperature T was in the range of 1320–1450°C and the pressure P – 10 MPa. The powders were under load until the end of shrinkage, which was controlled by the dial indicator with and accuracy of 10 μm. Specimens for tribological tests were cut by electro-erosive method.

The density of alloys being investigated was measured using the Archimedes immersion technique. We were focused on achieving the minimum value of porosity.

Temperature of phase transformations – beginning and the end of melting, beginning and the end of solidification, solid state transformations were determined by the method of differential scanning calorimetry (DSC) with 'Netzsch DSC 404 F1 Pegasus' instrument. The other method is differential thermoanalyses (DTA) with high temperature differential thermoanalyzer VDTA-8M (specimens were heated at the rate of 50–80°C/min. in helium atmosphere).

Microstructural examinations were carried out using the light microscope OLYMPUS IX70 at magnifications of × 50–500 and by scanning electron microscopy (JSM-6400 [JEOL Ltd]), additionally equipped with energy dispersion system.

XRD profiles of the specimens after heat resistance test were done using JEOL JSM6360LA SEM equipped with EDS.

Heat resistance of alloys being investigated was determined by weight gain per unit area. For testing, the specimens were placed into induction furnace in individual Al_2O_3 crucible. The heating up to T = 1100°C was carried out in the atmosphere of laboratory air. Temperature of heating was controlled by thermocouple. Annealing time intervals were 10 hours followed with furnace cooling, and the total annealing time was 50 hours. The weight increment was measured after each annealing stage.

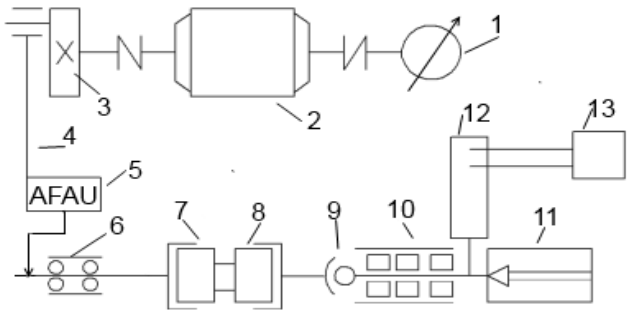

Fig. 1. The layout of wear test machine MFK-1: 1 – dial type rpm counter; 2 – electrical motor; 3 – adjustable crank-shaft unit; 4 – vertical connecting rod; 5 – amplitude fine adjustment unit; 6 – headstock; 7 – moving specimen; 8 – fixed specimen; 9 – self-aligning fixture; 10 tailstock; 11 – loading unit; 12 – strain gauge unit; 13 – data collector

DOI 10.2478/ama-2019-0009

Tab. 1. Chemical composition of metal components of powder alloys matrix

#	Material	Chemical element, mass fractions										
		Fe	Cr	Co	Ni	Al	Cu	Mn	Si	C	S	P
1	PK-1U	< 0.2	-	min 99.35	< 0.4	-	< 0.04	-	< 0.02	< 0.02	-	-
2	PACh 99H5	< 0.5	min 99	-	-	< 0.5	< 0.01	-	< 0.2	< 0.03	< 0.02	< 0.02
3	PIV1	Balance	-	-	-	-	< 0.02	< 0.1	< 0.08	-	< 0.015	< 0.15
4	PA1	< 0.35	-	-	-	min 99	< 0.02	-	< 0.4	-	-	-
5	ZhS32-VI	W 8.2	5.1	9.3	Balance	5.8	Mo 1.1	Nb 1.6	Ta 4.0	Re 4.0	Zr 0.05	B 0.015
6	PNE-1	0.01	-	0.15	min. 99.8	-	0.01	-	-	0.02	0.03	-

The study of material wear at fretting conditions requires the simulation of contact interaction between the contiguous surfaces in the mode of tangential oscillatory displacement. In this paper, such conditions were modelled on a wear test machine MFK-1 (Dukhota and Tisov, 2010). Its layout is shown in Fig. 1.

This allowed coarse adjustment of fretting amplitude. The frequency of rotation and the number of revolutions were recorded in rpm at counter 1. The fixed specimen 7 was fixed in a freely centred chuck, mounted on the shaft headstock 6. The loading of the samples was carried out by the screw type loading unit 11. The axial load on the samples was recorded using a dynamometer ZIP 02-79 (GOST 2283-79) with a measuring range 0.22 kN. Registration of friction force was carried out by data collector 13 with the help of strain gauge 12.

The amplitude of moving sample 7 oscillations was adjusted by changing the eccentricity of crank shaft 3 (coarse) and by the change in the horizontal arm length of amplitude fine adjustment unit 5. Coarse and fine adjustment allowed to change amplitude value in 10–1000 μm range, with accuracy – 2–10 μm. The relative displacement amplitude is defined as the difference between amplitudes of movable and fixed specimens oscillations. The amplitude was measured directly on the samples with the help of optical binocular microscope MBS-2 (with magnification 8–56) using a stroboscopic effect (stroboscope TST-100).

Linear wear was determined by profiling the ring-shaped wear track that was formed on the working surface of a fixed specimen in eight equilateral directions (Fig. 2) and was determined by the formula 1:

$$H_i = \sum_{1}^{8} h_j \qquad (1)$$

where: h_j – distance between mean lines of initial surface and wear track bottom profiles.

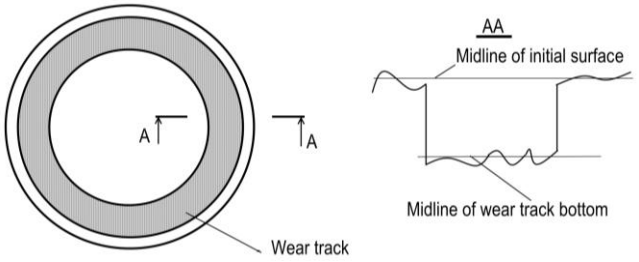

Fig. 2. Measuring linear wear

Profiling was carried out with the help of a 'Caliber'-type profilometer, which allows to measure the wear value h_j down to 0.1 mm with an accuracy of 1 × 10^{-4} mm. Each wear track was virtually divided into 8 sectors. The profilograms were made starting from the centre. To determine the linear wear, a mean value of these 8 profilograms was calculated.

3. RESULTS AND DISCUSSION

3.1. Estimation of heat sensitivity of Alloys

The melting temperature of the produced alloys is a very important issue. It should comply with the technological process of blades manufacturing, particularly soldering and outgassing procedures (1270°C); so in our case, taking into account the inaccuracies and random temperature deviations, it should be not less than 1300°C. The composition of alloys with TiC content 30, 40 i 50% (volume fractions), with cobalt, nickel and alloy ZhS32-VI matrix and their melting points are listed in Tab. 2.

Thermal heating curves of powder alloys with TiC content 30–50%, obtained by DTA and DSC confirm the possibility to fabricate composite materials based on nickel, cobalt and alloy ZhS32-VI without any phase transitions in solid state. Earlier, the attempts to study this by DTA analysis were performed, indicating good thermal properties of Ni-TiC sintered alloys, modified by cobalt or molybdenum. The maximum peaks are in the same temperature range as in current paper (Takashi et al. [1981]). Volkova et al. (1989) also reports high stability of the system. TiC particles dissolve nickel at maximum of 0.8%, and long holding time during sintering (up to 100 hours) helps to round their edges. Dissolved amounts of TiC will precipitate in nickel matrix, forming eutectic structure.

The absence of any additional thermal effects at heating is an evidence of structural and phase stability of produced composite materials. An example of the heating-cooling curves for Ni–40 vol. TiC alloy are given in Fig. 3.

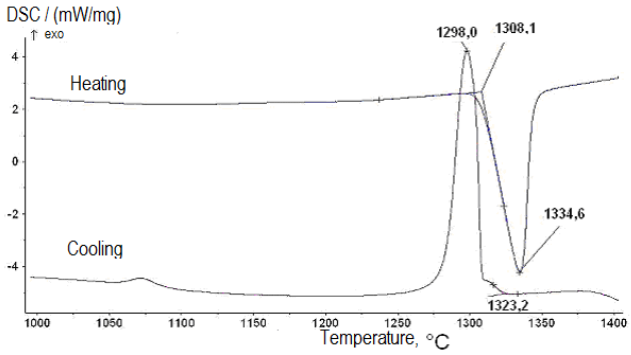

Fig. 3 The DSC curves of Ni-based alloy with 40 vol.% TiC

At temperatures above melting point, alloys lose their phase stability. This is proved by the rising of additional thermal effects at cooling. Melting temperatures of produced alloys are of the same value: 1320–1370°C, alloys based on ZhS32-VI are a little superior to others. The content of titanium carbide has no noticeable effect on melting temperature. Based on this, we can state that during sintering, TiC is not decomposed, and excessive carbon is effectively consumed by TiH. The minimum temperature of melting start of alloys (solidus temperature) is not less than 1320 ± 10ºC and is not dependent on TiC content in range of 30–50 vol. %.

Tab. 2. Composition and melting point of composite sintered alloys

№	Base, mass %			TiC		TiH, mass.%	Alloying elements, mass %			$T_{melt.}$, °C
	Co	Ni	ZhS32-VI	% vol.	mass.%		Cr	Fe	Al	
74	55.5	–	–	30	17.84	1.16	19.6	2.95	2.95	1350
13	50.0	–	–	40	25.36	1.64	17.7	2.65	2.65	1320
14	43.83	–	–	50	33.8	2.2	15.51	2.33	2.33	1325
80	–	55.5	–	30	17.84	1.16	19.6	2.95	2.95	1330
6	–	50.0	–	40	25.36	1.64	17.7	2.65	2.65	1320
7	–	43.83	–	50	33.8	2.2	15.51	2.33	2.33	1320
100	–	–	81	30	19	–	–	–	–	1370
101	–	–	73	40	27	–	–	–	–	1355
102	–	–	64	50	36	–	–	–	–	1355

3.2. Hardness values

A very important indication of wear resistance is the hardness of alloys. We measured it using the Rockwell method. Hardness test results indicate strong impact of TiC content on hardness of alloys being investigated. Generally, increase of carbide content leads to increase of hardness. It has been found that increase of TiC content over 50% (vol.) has no beneficial effect on hardness. The hardness of cobalt based alloy having 30% (vol.) of TiC is 52 HRC. Alloys with 50 and 60% (vol.) of TiC have the same value of hardness, namely 67 HRC. The hardness of alloys with 50% (vol.) of TiC for nickel and cobalt matrix is 64 and 67 HRC, respectively.

3.3. Redistribution of elements beneath the oxide film

Wear and fretting resistance are structure sensitive properties. The matrix-filler ratio is one of decisive factors of wear resistance. The microstructural examinations indicate a uniform distribution of components of the alloys. There are just some areas with reduced or increased TiC content, but they are not capable to alter the properties of the examined materials, Fig. 4 represents the microstructure of 50% vol. of TiC Co-based alloy with EDS scanning areas after heat resistance tests– the material beneath oxide film was analysed. Chemical composition of scanned areas is given in Tab. 3.

The darkest phase is titanium carbide with some minor content of the other alloying elements. Matrix material represents a mixture of cobalt (light phase) and chromium (grey phase) solid solutions. Light phase contains reduced (compared to nominal composition) amount of chromium, but increased amount of aluminium and iron. Lower chromium content in cobalt-based solid solution may become a reason for reduced heat resistance of the alloy.

Based on EDS analyses of Ni-40% vol. TiC alloy after heat resistance testing, the chemical composition of the alloy was determined (Fig. 5). The results of the analyses are shown in Tab. 4.

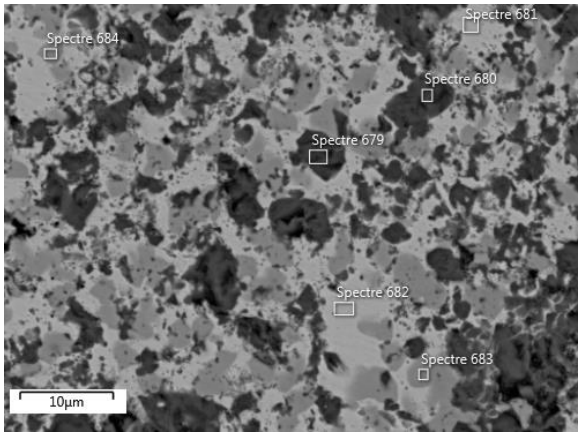

Fig. 4. Microstructure and distribution of chemical elements of cobalt-based alloy with 50% vol. of TiC after heat resistance test

Tab. 3. Chemical composition of scanned areas of cobalt alloy

№	Composition, mass %					Note
	Co	Cr	Al	Fe	Ti	
679	2.06	1.08	0.1	0	96.76	(TiC)
680	1.95	0.84	0	0.28	96.93	
681	76.47	12.76	2.87	4.24	3.67	Light phase
682	78.32	12.9	2.87	4.17	1.74	
683	12.93	81.41	0	1.14	4.52	Grey phase
684	23.11	73.33	0.23	1.92	1.41	
	43.8	15.5	2.33	2.33	33.8 TiC + TiH	Nominal composition

Three types of phases were clearly distinguished. The darkest phase – TiC grains, consisting of major amount of titanium with some admixtures of nickel and chromium. In contrast to cobalt-based alloys, aluminium and iron were not detected in the composition of titanium carbide, but it contains some amount of chromium and nickel. The grey phase was a nickel-based solid solution, containing significant, that is, more than 26 vol. % of chromium. Amount of the other alloying elements here was also higher

DOI 10.2478/ama-2019-0009

if compared to nominal composition. This nickel solid solution with increased amount of alloying elements would probably have better heat resistance than cobalt solid solution. The light phase was a chromium based solid solution. Here, chromium segregation was more significant if compared to the cobalt-based alloy, and it contained fewer admixtures.

These results proved dissimilar diffusion rate of alloying elements in cobalt and nickel. For nickel, this process was much faster, which was indicated by the higher content of chromium, aluminium and iron. This provided a more dense oxide film with, particularly, high content of chromium.

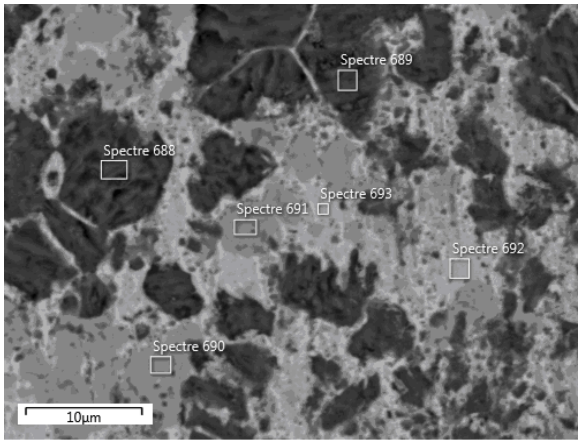

Fig. 5. Microstructure and distribution of chemical elements of Ni – 40 vol. % TiC alloy after heat resistance test

Tab. 4. Chemical composition of scanned areas of nickel alloy

№	Composition, mass %					Note
	Ni	Cr	Al	Fe	Ti	
688	0.5	0.22	0	0	99.28	(TiC)
689	0.87	0.52	0	0	98.61	
690	2.13	92.77	0	1.39	3.71	Light phase
691	1.72	91.45	0	1.1	5.73	
692	60.09	26.22	3.43	6.44	3.83	Grey phase
693	60.3	26.45	3.36	6.39	3.5	
	50	17.7	2.65	2.65	27 TiC + TiH	Nominal composition

The light part of the micrograph was a nickel or cobalt based solid solution of alloying elements. Darker areas were particles of TiC. The size of carbide particles was 5–10 μm, as initially it was in powders, so no TiC grain growth during prolonged heating at sintering was observed.

3.4. Impact of porosity on heat resistance of Ni- and Co-based powder alloys

The analyses of heat resistance of the alloys have indicated that during the first 10 hours of test, high temperature oxidation runs quite fast; subsequently, it slows down and becomes almost constant. Heat resistance of alloys was dependent on heat resistance of both matrix and filler material. As far as heat resistance of TiC was less than heat resistance of cobalt and especially ZhS32-VI matrix, the increase of carbides content led to decrease of heat resistance. The other structural factor influencing heat resistance was porosity. The tests of heat resistance showed that increase of porosity led to decrease of heat resistance. The results of estimation of porosity impact on heat resistance of cobalt based alloys are presented on Fig. 6 and this is characteristic for all alloys despite matrix material and carbides content (Cherepova et al., 2015, Cherepova et al., 2016a). This is evident from Fig. 6 presenting weight increment at temperature 1100°C for alloys with identical content of TiC – 50% vol. but dissimilar porosity.

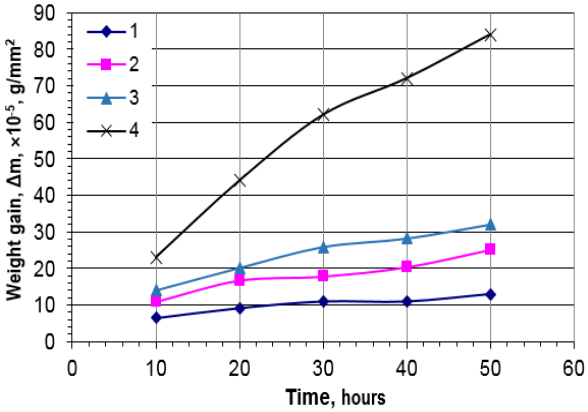

Fig. 6. Oxidation rate of cobalt-based alloys containing 50% vol. of TiC with dissimilar porosity: № 1 – 3.1%; № 2 – 6.0%; № 3 – 10.4%; № 4 – 28.0%

The rise of porosity from 3 to 28 % caused an increase of weight gain in order of 3 after 10 hours of annealing. For alloys 1-3, further test gave likely steady weight gain, but for alloy № 4, it changed rapidly. After 50 hours of annealing, compared to alloy № 1, it had 6.5 times higher weight gain. Having this results, we supposed the existence of direst impact of porosity on heat resistance of Co-TiC alloys. The data from Fig. 6 allows to estimate the porosity impact on heat resistance as follows:

$$I_p = (Wg_{28}\text{-}Wg_{3,1})/(28\text{-}3.1) \quad (1)$$

where I_p is calculated value of porosity impact, Wg – weight gain for alloy with porosity marked in subscript. Increase of porosity caused proportional increase of weight gain – about 2.84×10^{-5} g/mm^2 per 1% of porosity.

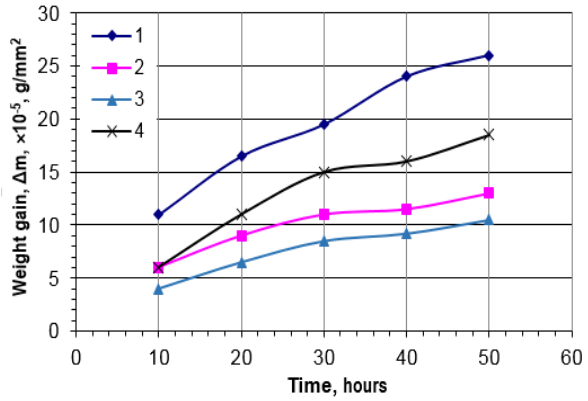

Fig. 7. Oxidation rate of nickel-based alloys containing 40% vol. of TiC with porosity: № 1 – 10%; № 2 – 4.4%; and 30% vol. of TiC with porosity: № 3 – 0% (cast alloy); № 4 – 7.1%

DOI 10.2478/ama-2019-0009 acta mechanica et automatica, vol.13 no.1 (2019)

To evaluate the influence of porosity on oxidation of nickel-based alloys, four reference specimens were fabricated, containing 30 and 40 vol. % of TiC, respectively. Their porosity ranged from 0% (cast alloy) up to 7.1%. The results are presented in Fig. 7.

Here, the presence of porosity also causes increased weight gain. A cast alloy with 30 vol. % of TiC and theoretical density has the highest heat resistance. The alloy having the same carbide content but 7.1 % of porosity has 1.75 times higher weight gain. The calculated impact of porosity was 1.14 $\times 10^{-5}$ g/mm^2 per 1% of porosity. The alloy containing 40 vol. % of TiC had the worst heat resistance. Increasing of porosity from 4.4 to 10% for this alloy caused increment of weight gain in 2 times and the calculated impact of porosity was 2.2 $\times 10^{-5}$ g/mm^2 per 1%

The presence of high number of pores facilitates oxygen supply into the material. The thickness of oxide layer in surface material may reach several tenth of micrometres. Porosity increases the surface area of material. Internal surfaces of pores are also subjected to oxidation. So, the interaction area increases, leading to higher oxidation rate of composite material. But, it should be mentioned that intrinsic heat resistance of matrix material (alloyed cobalt or nickel) and titanium carbide do not depend on porosity.

3.5. Examination the composition of oxide films

The results of EDS analyses of the edge of this alloy (Fig. 8) indicate the main elements taking part in oxidation. They are aluminium, chromium and cobalt (more intensive colour corresponds to higher content of chemical element). Fig. 8 gives the answer about the most active elements taking part in the formation of oxide film. They are, except the main matrix material, chromium and titanium. The oxides, formed by these elements are well known to be good barriers for further oxygen penetration into the material. Also, they are good to reduce the wear of examined materials in conditions of high temperature fretting wear.

As far as the content of aluminium in alloy is insignificant, it plays only auxiliary role in the oxidation process. Its amount in surface layer is not significant, but activated diffusion increases its quantity. Increased carbon content in surface layer is caused by oxidation and decomposition of TiC. Next analysed element is cobalt. Its content in surface layer seems to be unchanged, but results of previous analyses indicate areas (Fig. 4) with decreased or increased content of this element. Chromium content is sharply decreased in surface layer, but this is explained by significant oxygen uptake by oxide film, which is clearly observed on the corresponding diagram, Fig. 8. Also, partially it is substituted by aluminium. The change of iron distribution can hardly be detected on the diagram. Finally, the distribution of titanium corresponds to the microstructural distribution of TiC particles. Oxygen content is quite significant in surface layer. This is explained by the formation of protective oxide layer; it is mainly combined with cobalt, chromium and titanium.

The results of XRD analyses of oxide layer after the heat resistance test outline the primary chemical compounds formed during oxidation (Fig. 9–10).

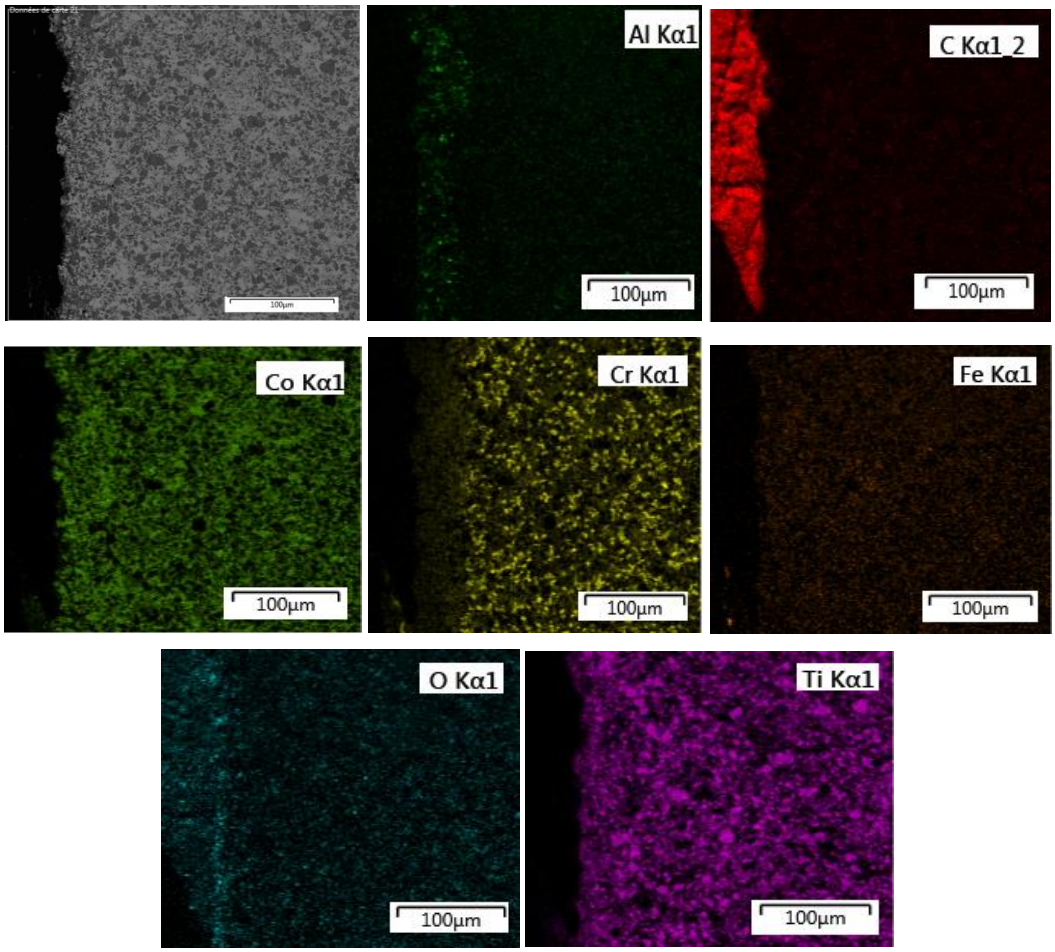

Fig. 8. EDS image and associated elemental map of the edge of the Co-50 vol. % TiC composite alloy

DOI 10.2478/ama-2019-0009

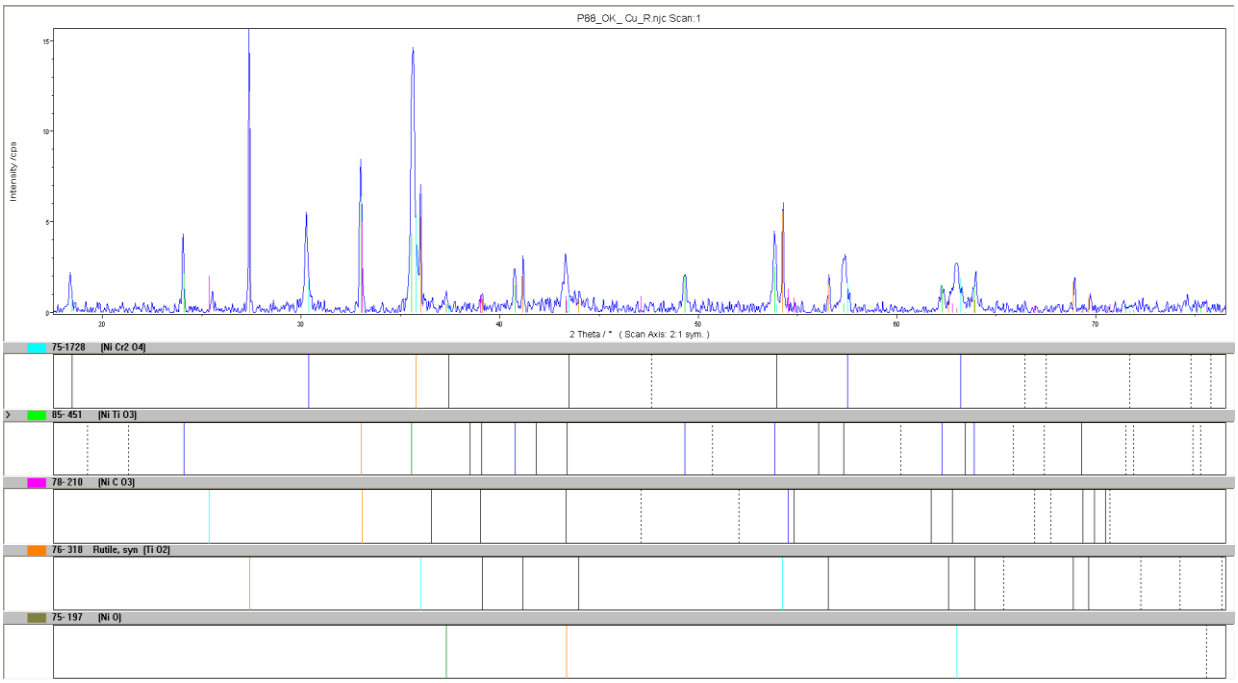

PDF-No	In Range	Matched	FOM	SOM	Name Min.	Formula
85-451	35	12	0.589	4.210	Nickel titanium oxide	$NiTiO_3$
76-318	20	8	0.622	4.419	Rutile, syn	TiO_2
75-1728	17	6	1.893	5.784	Nickel chromium oxide	$NiCr_2O_4$
78-210	25	8	2.360	5.524	Nickel carbon oxide	$NiCO_3$
75-197	5	1	4.669	25.000	Nickel oxide	NiO

Fig. 9. XRD profile of scale powders of Ni+ 40 % vol. TiC after heat resistance test (1100°C)

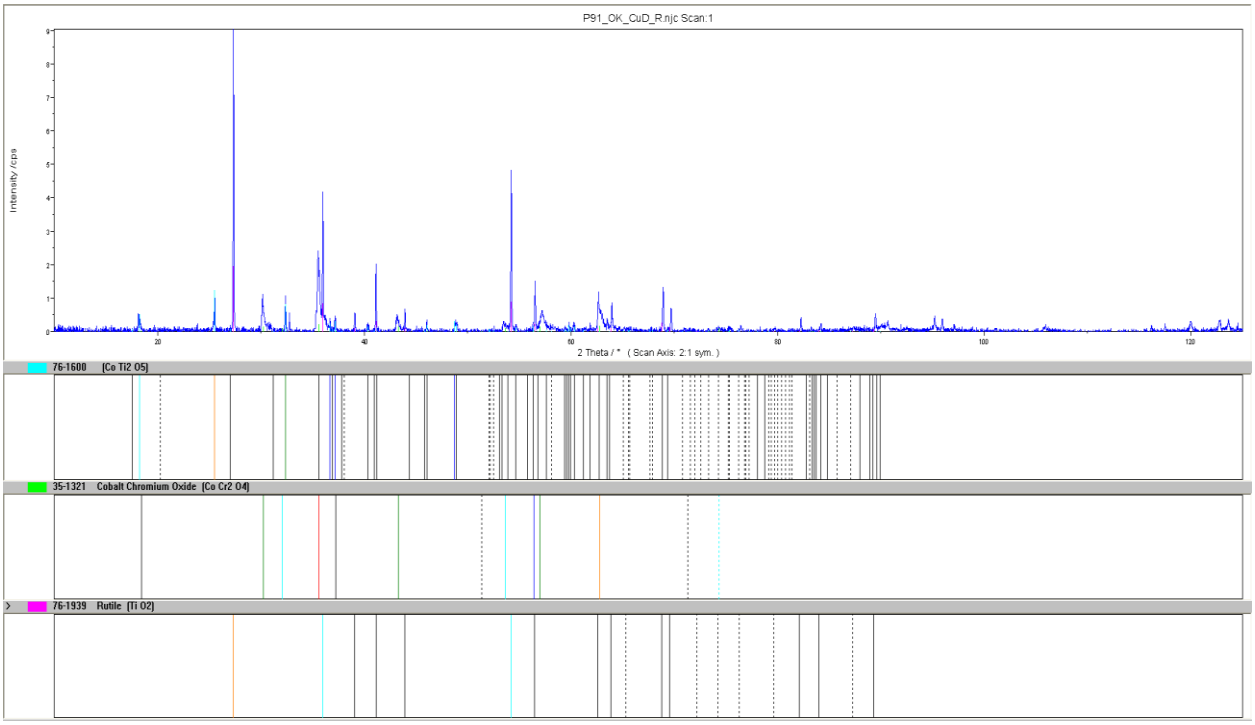

PDF-No	In Range	Matched	FOM	SOM	Name Min.	Formula
76-1939	20	3	0.685	9.428	Rutile	TiO_2
76-1600	86	6	2.983	14.333	Cobalt titanium oxide	$CoTi_2O_5$
35-1321	13	1	12.092	31.843	Cobalt chromium oxide	$CoCr_2O_4$

Fig. 10. XRD profile of scale powders of Co+ 50 % vol. TiC after heat resistance test (1100°C)

DOI 10.2478/ama-2019-0009

Based on the results of X-ray structural analyses, the basic components of scale on the surface of specimens (Ni + 40% vol. TiC), after tests for heat resistance, were rutile TiO_2, nickel-titanium oxide $NiTiO_3$, nickel-chromium oxide $NiCr_2O_4$ and vustite NiO. Fig. 9 presents the results of heat resistance testing of alloys containing 40% vol. of TiC. Test temperature was 1100°C. Here, the combination of oxides is more complex if compared to the cobalt-based alloy. Here, 5 chemical compounds were found, and the major was the quantity of nickel chromium oxide. The amount of titanium was much less than it was in previous case. It is interesting to mention the presence of unstable nickel carbonate $NiCO_3$. Usually, it decomposes into nickel and carbon oxides. It may appear temporally, as far as nickel oxide is found in significant quantities, and carbon oxide later evacuates from the oxide film.

Based on the results of X-ray structural analyses, the basic components of scale on the surface of specimens (Co+50% vol. TiC), after tests for heat resistance, were ruthile (Fig 10), cobalt-titanium oxide $CoTi_2O_5$ and cobalt-chromium oxide $CoCr_2O_4$. In other specimens of this type, the traces of ilmenite $FeTiO_3$ were detected. The amount of titanium oxide was the highest among the formed chemical compounds. Cobalt titanium oxide followed it. This indicates that cobalt matrix does not provide a good protection of carbide grain. Chromium diffusion, as it was shown earlier in this paper, was not high enough to form a dense protective layer. The carbon content in oxide layer was not detected, while its content in sublayer (Fig. 8) was significant. It may be explained by higher reactivity of chromium to oxygen (carbides and carboxides were not formed) and evaporation of carbon oxides out from the oxide layer. These factors provide lower heat resistance if compared with nickel-based alloy.

3.6. Heat resistance test results

The final test for heat resistance was done for sintered alloys containing the same amount of titanium oxide – 40 vol. % in order to find the best combination of matrix type. The results of these tests are presented on Fig. 11.

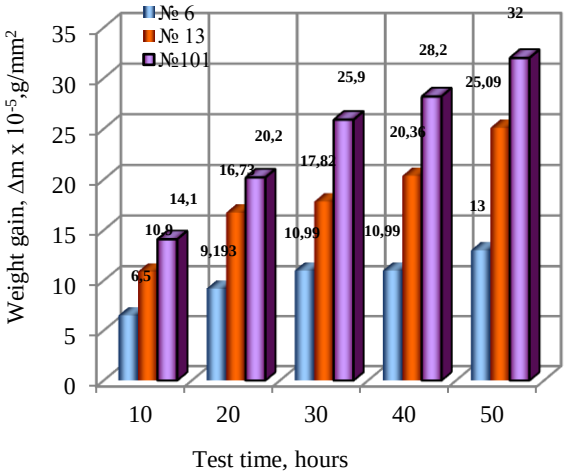

Fig. 11. Heat resistance of alloys with 40 % vol. of TiC: № 6 – nickel-based; № 13 – cobalt-based; № 101 – based on ZhS32-VI

During all 50 hours of tests, the weight increment of nickel-based alloys remained the lowest. Of course, additional impact on heat resistance was provided by porosity. However, for the examined alloys, deviation was not significant and may be neglected. For all temperatures and stages of the test, heat resistance of nickel-based sintered alloy remained superior to others.

The oxidation of nickel and cobalt based alloys runs according to similar mechanism with formation of similar oxides (Fig. 9–10). They have the same amount and kind of alloying elements. Generally, they may be considered as Ni – Cr and Co – Cr systems. If chromium content is high enough, and a dense layer of Cr – containing oxides are formed, the oxidation rate of alloys is almost the same, but oxidation resistance of cobalt is less than that of nickel. The adhesion of oxide layer to the substrate of nickel-based alloy is also higher (Dukhota and Tisov, 2010). These factors explain lower heat resistance of cobalt based alloys.

Alloy based on ZhS32-VI, which is used to produce turbine rotor blades, has the lowest heat resistance. This is explained by the purpose of the alloy. The main requirement to it is strength at high temperatures, but not high heat resistance. The surface of turbine blade is reliably protected by ambient barrier coatings. That is why heat resistance of sintered alloy based on ZhS32-VI is the lowest among the examined alloys, but it still has acceptable value.

3.7. Wear resistance of examined alloys

Wear resistance of alloys at high temperatures depend on heat resistance and high temperature strength. The results of fretting-wear test of cobalt-based (Cherepova and Dmytrieva, 2016a, 2016, Cherepova and Dmitrieva, 2016b), nickel-based (Cherepova et al, 2016) and alloys based on ZhS32-VI (Dmitrieva et al, 2017). These alloys were tested in a wide range of temperature and loads, in fretting-wear conditions (Dukhota et al, 2017). The summarized test result of alloys with titanium carbide (50% vol.) as a strengthening phase are presented in Fig. 12. Maximum testing temperature was 1050°C

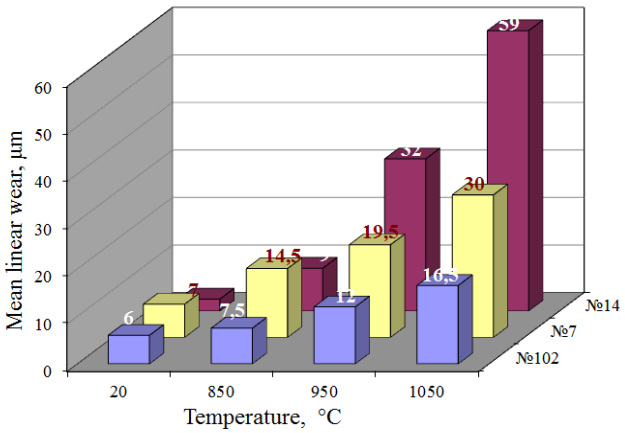

Fig. 12. Mean linear wear of sintered alloys with 50% vol. of TiC based on: №7 – nickel; №14 – cobalt; №102 – ZhS32-VI

Test results indicated superior fretting resistance of sintered alloy based on ZhS32-VI at all test temperatures. Most significantly, this was seen at temperature 1050°C – its linear wear was twice less than that of alloy based on nickel and almost three times less than that of alloy based on cobalt. This is explained by high strength of ZhS32-VI alloy, strengthened by precipitation of

Ni_3Al γ' and by significant solution strengthening. Basically, it was stronger than nickel- and cobalt-based matrices.

At temperature range up to ≈ 900°C, the nickel based alloys have twice as much value of wear as compared with cobalt-based alloys. However, at temperature of 1050°C cobalt-based alloys are twice as much superior than the nickel-based alloy. At lower temperatures, cobalt matrix is stronger, and for both alloys the oxidation is not significant. Predominant wear mechanism (based on earlier researches (Cherepova and Dmitrieva, 2016a, Cherepova et al., 2014, Dmitrieva et al., 2017) is abrasive wear. So, wear resistance is provided by strength and hardness of sintered alloys. At higher temperatures, oxidation wear is predominant and heat resistance and oxide layer adhesion to the substrate play an important role. As it was mentioned above, adhesion of nickel alloy oxide layer is stronger as compared with cobalt alloy.

Based on the conducted investigation, produced and examined alloys have good values of melting temperatures, wear resistance, heat resistance and technological properties and may be recommended for application as wear protective material for turbine rotor blades top shrouds. The availability of several materials with predictable wear resistance facilitates the choice of appropriate material for particular (stress and temperature) working conditions.

4. CONCLUSIONS

1. Three types of sintered alloys strengthened by TiC powders having alloyed cobalt, nickel or alloy ZhS32-VI matrices were produced. Results of DTA and SDC confirm that these alloys have no additional thermal effects and phase transitions until melting. Their melting temperatures are of the same order with industrial nickel-based alloys (basic materials for turbine blades manufacturing) and are in the range of 1320–1370°C.
2. The tests for heat resistance indicated the highest properties of nickel-based alloy, followed by cobalt-based alloy and alloy with ZhS32-VI matrix. Heat resistance of sintered alloys is greatly affected by porosity: porosity increase from 3% up to 28% for 50% TiC cobalt based alloy weight gain rises in order of 8. This is due to the facilitated oxygen inflow into the material, and high surface area of alloy, which includes the surface of pores. Increased porosity provides bigger specific area of the alloy, and therefore, the area, exposed to oxidation is much bigger then nominal surface area of test specimen. This results in increased weight gain during heat resistance test.
3. Based on the X-ray structural analyses, we revealed the formation of compound oxides $CoTi_2O_5$ and cobalt-chromium oxide $CoCr_2O_4$., ilmenite $FeTiO_3$ TiO_2, nickel-titanium oxide $NiTiO_3$, nickel-chromium oxide $NiCr_2O_4$ and vustite NiO. On the wear surface, they formed 'glazed' ceramic-like layer protecting the material from further oxidation and improving its wear behaviour. This layer plays the role of a barrier, and oxygen diffusion into material is arrested. Also, being smooth, it reduces frictional losses. This layer is also better resistant to abrasive action of worn outcropped particles.
4. Wear tests in conditions of high temperature fretting indicate dissimilar wear resistance of materials. Cobalt alloys have the best wear resistance at room temperature. At higher temperature alloy based on ZhS32-VI matrix is superior as compared with others. Especially at temperature 1050°C, it is two and three times more wear resistant as compared with Ni- and Co-based alloys respectively.
5. Fabricated alloys have high enough melting point to undergo soldering and outgassing procedures entirely with turbine blade. Heat resistance of examined composites is superior or at least the same if compared with alloys (basically with ZhS32-VI) used for manufacturing turbine blades. They also have good fretting resistance at high temperatures. Mentioned properties accompanied with structural stability and uniformity make these sintered composites promising to be used as wear protectives for contact faces of turbine blade top shrouds.

REFERENCES

1. **Babak A., Barsoum M.W.** (2016). Energy damping in magnesium alloy composites reinforced with TiC or Ti2AlC particles, *Materials Science & Engineering*, A 653, 53–62.
2. **Babak A., Casi E.N., Barsoum M.W.** (2014), Fabrication and mechanical properties of pressureless melt infiltrated magnesium alloy composites reinforced with TiC and Ti_2AlC particles, *Materials Science and Engineering*, 618, 511–522.
3. **Baskaran S., Anandakrishnan V, Muthukannan Duraisel Vam, Keerthivasan N**. (2015) Study on dry sliding friction behaviour of tic reinforced AA7075 in-situ composites by Taguchi analysis, *International Journal of Mechanical And Production Engineering*, 3(3), 9–12.
4. **Bin C., Ye-fa T., Long H., Hua T., Li G.** (2013), Tribological properties of TiC particles reinforced Ni-based alloy composite coatings, *Transactions of Nonferrous Metals Society of China*, 23(6), 1681–1688.
5. **Cherepova T.S., Dmitrieva G.P.** (2016a) The Wear Features of Powder Cobalt Alloys Strengthened with Titanium Carbide, *Powder Metallurgy and Metal Ceramics*, 55(5-6), 374–378.
6. **Cherepova T.S., Dmitrieva G.P., Nosenko A.V., Semirga A.M.** (2014) Wear-resistant alloy for protection of contact surfaces of working aircraft engine blades from oxidation at high temperatures, *Science and Innovation*, 10(4), 20–28.
7. **Cherepova T.S., Dmytrieva H.P.** (2016b) Properties of titanium carbide-strenghtened cobalt-based sintered alloys, *Metal Physics and Advanced Technologies*, 38(11), 1497–1512 (in Ukrainian).
8. **Cherepova T.S., Dmytrieva H.P., Hosenko V.K.** (2015) Heat resistance of cast and sintered alloys based on nickel and cobalt strengthened with carbides, *Metallurgy and Heat Treatment of Metals,* 3, 36–40 (in Ukrainian).
9. **Cherepova, T.S., Dmitrieva, G.P., Nosenko, V.K.** (2016a). Heat resistance of the powder cobalt alloys reinforced with niobium or titanium carbide, *Science and Innovation*, 12(1), 5–10.
10. **Cherepova, T.S., Dmytrieva, H.P., Dukhota, O.I., Kindrachuk, M.V.** (2016b) Properties of nickel powder alloys hardened with titanium carbide, *Materials Science*, 52(2), 173–179.
11. **Chinmaya K.S., Manoj M.** (2015). Effect of pulse laser parameters on TiC reinforced AISI 304 stainless steel composite coating by laser surface engineering process, *Optics and Lasers in Engineering*, 67, 36–48.
12. **Chukwuma C., Onuoha X., Chenxin J., Zoheir N.F., Georges J.K., Kevin P.P.** (2016). The effects of TiC grain size and steel binder content on the reciprocating wear behaviour of TiC-316L stainless steel cermets wear, *Wear*, 350-351, 116–129.
13. **Dmitrieva G.P., Cherepova T.S., Kosorukova T.A., Nichiporenko V.I.** (2015) Structure and properties of wear resistant cobalt-based alloy with niobium carbide, *Metal Physics and Advanced Technologies,* 37(7), 973–986 (in Russian).
14. **Dmytrieva H.P., Cherepova T.S., Dukhota O.I., Nychyporenko V.I.** (2017), Investigation of properties of sintered alloys based on ZhS32-VI with titanium carbide, *Powder Metallurgy*, 11/12, 68–75 (in Ukrainian).

15. **Dukhota O.I., Tisov O.V.** (2010), The study on wear resistance of heat resistant composite alloys in conditions of high temperature fretting-wear, *Problems of friction and wear*, 53, 195–200 (in Ukrainian).
16. **Dukhota O.I., Tisov O.V., Cherepova T.S., Dmytrieva H.P., Kharchenko V.V.** (2017), Tribotechnical examinations of high temperature wear resistant particle-reinforced alloys, *Problems of friction and wear,* 3(76), 60–66 (in Ukrainian).
17. **Jung S.-A., Kwon H., Suh C.-Y., Oh J.-M., Kim W.** (2015). Preparation of a fine-structured TiC–Co composite by high-energy milling and subsequent heat treatment of a Ti–Co alloy, *Ceramics International*, 41(10), 14326–14331.
18. **Karantzalis A.E., Lekatou A., Evaggelidou M.** (2013), Microstructure and sliding wear assessment of Co–TiC composite materials, *International Journal of Cast Metals Research*, 27(2), 73–79.
19. **Levashov E.A., Mishina E.S., Malochkin O.V., Stanskii D.V., Mour J.J., Fadeev M. I.** (2003). Effect of nanocrystalline powders on the structure and properties of dispersion-hardened alloy TiC – 40% KhN70Yu, *Metallurgis*t, 47(3/4), 133–139.
20. **Lieontiev V.A., Zilichihis S.D., Kondratiuk Ye.V., Zamkovoi V.Ye.** (2006). Recovery of workability of GTE using new technologies and materials, *Herald of Engine Constructing*, 4, 99–103 (in Russian).
21. **Ouyang T., Wu J., Yasir M., Zhou T., Fang X., Wang Y., Liu D., Suo J.** (2016), Effect of TiC self-healing coatings on the cyclic oxidation resistance and lifetime of thermal barrier coatings, *Journal of Alloys and Compounds*, 656, 992–1003
22. **Sakamoto T., Kurishita H., Matsuo S., Arakawa H, Takahashi S, Tsuchida M., Kobayashi S., Nakai K,. Terasawa M., Yamasaki T., Kawai M.** (2015) Development of nanostructured SUS316L-2%TiC with superior tensile properties, *Journal of Nuclear Materials*, 466, 468–476.
23. **Shuster L.S., Mamleyev R.F., Kamaletdinova R.R., Chertovskikh S.V., Kireev R.M.** (2016). Wear of friction pairs made of titanium carbide-based metal–ceramic material, *Journal of Friction and Wear*, 37(2), 165–169.
24. **Sun-A.J., Hanjung K., Chang-Yul S., Jung-Min O., Wonbaek K.** (2015), Preparation of a fine-structured TiC–Co composite by high-energy milling and subsequent heat treatment of a Ti–Co alloy, Ceramics International, 41, 14326–14331.
25. **Takahashi S., Ikeno S., Imai E.** (1981). Differential thermal analysis and structure of the Ni-TiC system, *Journal of Materials Science*, 16(12), 3418–3426.
26. **Tretiachenko G.N., Kravchuk G.N., Kuriat R.I., Voloshchenko A.P.** (1975) Bearing capacity of gas turbines blades at nonstationary haet and force effect, *Kyiv.: Naukova Dumka* (in Russian).
27. **Volkova N. M., Dudorova T. A., Gurevich Y. G.** (1989). Influence of hold time on carbide grain growth in TiC-Ni alloys, *Soviet Powder Metallurgy and Metal Ceramics*, 28(8), 613–617.
28. **Wei Z.**(2012). Research on Microstructure and Property of TiC-Co Composite Material Made by Laser Cladding, *Physics Procedia*, 25, 205–208.
29. **Yuxin Li, Peikang Bai, Yaomin Wang, Jiandong Hu, Zuoxing Guo** (2009). Effect of TiC content on Ni/TiC composites by direct laser fabrication, *Materials & Design*, Vol. 30, Iss. 4. 1409–1412.
30. **Zhang X.-H., Han J.-C., Du S.-Y., Wood J.V.** (2000). Microstructure and mechanical properties of TiC-Ni functionally graded materials by simultaneous combustion synthesis and compaction, *Journal of Materials Science*, 35(8), 1925–1930.
31. **Zohari S., Sadeghian Z., Lotfi B., Broeckmann C.** (2015). Application of spark plasma sintering (SPS) for the fabrication of in situ Ni–TiC nanocomposite clad layer, *Journal of Alloys and Compounds*, 633, 479–483.

Acknowledgements: the present work is supported by funding from the Ministry of Education and Science of Ukraine, (Project # 0117U004330 'Scientific fundamentals of designing novel technologies of surface engineering for elements of aircraft tribomechanical systems made of titanium alloys') and by the National Academy of Science of Ukraine (Project # 0115U003007 'Phase equilibria in multicomponent eutectic alloys based on Al, Co, Ni and Ti, promising for use in power and civil engineering').

.

ABSTRACTS

Grzegorz Żywica, Paweł Bagiński
Investigation of Gas Foil Bearings with an Adaptive and Non-Linear Structure

The article discusses the results of simulation-based and experimental research carried out on gas foil bearings. Owing to the use of a set of flexible thin foils in such bearings, they exhibit certain beneficial features that cannot be found in other types of bearings. They have nonlinear operational characteristics and allow the dissipation of excess energy, thus reducing the vibration level. Moreover, gas foil bearings can self-adapt themselves to the current operating conditions by changing the shape of the lubrication gap. Therefore, they can be used to improve the dynamic performance of rotors, in particular, those operating at very high rotational speeds. This article explains the mechanisms for changes of stiffness and vibration damping in compliant components of a foil bearing. The results of the analysis of the bearing's subassemblies using advanced numerical models are presented. They are followed by conclusions that were drawn not only from these results but also from the results of the experimental research. It has been proven that the rotor supported on carefully designed foil bearings is capable of maintaining a low vibration level, even if it operates at a high rotational speed.

Volodymyr Zelenyak
Mathematical Modeling of Stationary Thermoelastic State for a Plate with Periodic System Inclusions and Cracks

Two-dimensional stationary problem of heat conduction and thermoelasticity for infinite elastic body containing periodic system of inclusions and cracks is considered. Solution of the problem is constructed using the method of singular integral equations (SIEs). The numerical solution of the system integral equations are obtained by the method of mechanical quadrature for a plate heated by a heat flow, containing periodic system elliptic inclusions and thermally insulated cracks. There are obtained graphic dependences of stress intensity factors (SIFs), which characterise the distribution of intensity of stresses at the tops of a crack, depending on the length of crack, elastic and thermoelastic characteristics inclusion, relative position of crack and inclusion.

Piotr Gierlak
Position/Force Control of Manipulator in Contact with Flexible Environment

The paper presents the issue position/force control of a manipulator in contact with the flexible environment. It consists of the realisation of manipulator end-effector motion on the environment surface with the simultaneous appliance of desired pressure on the surface. The paper considers the case of a flexible environment when its deformation occurs under the pressure, which has a significant influence on the control purpose realisation. The article presents the model of the controlled system and the problem of tracking control with the use of neural networks. The control algorithm includes contact surface flexibility in order to improve control quality. The article presents the results of numerical simulations, which indicate the correctness of the applied control law.

Serpil Şahin, Hüseyin Demir
Numerical Solution of Natural Convective Heat Transfer under Magnetic Field Effect

In this study, non-Newtonian pseudoplastic fluid flow equations for 2-D steady, incompressible, the natural convective heat transfer are solved numerically by pseudo time derivative. The stability properties of natural convective heat transfer in an enclosed cavity region heated from below under magnetic field effect are investigated depending on the Rayleigh and Chandrasekhar numbers. Stability properties are studied, in particular, for the Rayleigh number from $\mathbf{10^4}$ to $\mathbf{10^6}$ and for the Chandrasekhar number 3, 5 and 10. As a result, when Rayleigh number is bigger than $\mathbf{10^6}$ and Chandrasekhar number is bigger than 10, the instability occurs in the flow domain. The results obtained for natural convective heat transfer problem are shown in the figures for Newtonian and pseudoplastic fluids. Finally, the local Nusselt number is evaluated along the bottom wall.

Grzegorz Mieczkowski
Static Electromechanical Characteristics of Piezoelectric Converters with Various Thickness and Length of Piezoelectric Layers

The paper presents the analysis of electromechanical characteristics of piezoelectric converters subjected to an electric field and mechanical load. The analyses were performed based on a method consisting implementation of special segments responsible for electrical boundary conditions to a homogeneous beam. Constitutive equations were developed, allowing one to obtain static electromechanical characteristics for piezoelectric actuators with freely defined boundary conditions and geometry. Moreover, based on constitutive equations obtained, a particular solution for cantilever transducer subjected to concentrated force has been developed. The resulting analytical solution was compared with the data available in the literature, and the developed FEM solution. Furthermore, the influence of factors such as relative length, thickness and location of particular piezoelectric layers on electromechanical characteristics of the transducer was defined.

Jerzy Jaroszewicz, Krzysztof Łukaszewicz, Vladimir Antonyuk
Design of the Vibrostabilisation Stand for Reducing Residual Stresses in Discs used in the Construction of Multi-Plate Clutches and Brakes

Heavy-duty, oil-cooled brake discs (MMOTs) are often used in heavy-duty brake systems manufactured by companies such as Caterpilar, Clark, Komatsu and Liebherr. These discs are usually made of special steels, and in most cases, the flatness of the working surfaces should not exceed 0.15–0.30 mm. Although the technological processes of friction disc production include several stages of heat treatment and grinding, the required accuracy is not achieved in some cases. In addition, the remaining residual stresses lead to the deformation of the discs during their lifetime. In production practice, three methods are used to reduce residual stresses: thermo-fixing, dynamic stabilisation and vibratory stabilisation consisting in bringing discs to transverse resonance vibrations and maintaining resonance until significant stress reduction. The article proposes a method of stabilising the discs using the resonance phenomenon at the first few frequencies. In this article, Cauchy's function method and characteristic series method are used to develop solution value problem for clamped circular plates with discrete inclusions as concentrated masses and springs. Calculation methods for quick estimation of the own frequency of discs with additional ring mass enabling the use of low power vibration inductors are presented. The use of a special membrane and a pneumatic cushion in the construction of the stand allows to induce vibrations of higher frequencies.

Mariusz Leus, Marta Abrahamowicz
Experimental Investigations of Elimination the Stick-Slip Phenomenon in the Presence of Longitudinal Tangential Vibration

The article presents a scheme and description of the test stand as well as selected experimental results of the influence of longi-tudinal tangential vibrations on the stick-slip phenomenon. The tests were carried out at a constant forced vibration frequency f = 2000 Hz, as a function of the amplitude of the vibration velocity v_a. The position of the sliding body and the drive force necessary to make the body slip and maintain this motion were measured. The measurements were made in two successive stages. In the first stage, when the substrate on which the sliding occurred was stationary. In the second one, the substrate is in a vibrating motion in the direction parallel to the slip. The conducted experimental analyses have shown that longitudinal tangential vibrations can contribute to the reduction or even complete elimination of the stick-slip phenomenon.

Grzegorz Górski, Grzegorz Litak, Romuald Mosdorf, Andrzej Rysak
Periodic Trends in Two-Phase flow Through a Vertical Minichannel: Wavelet and Multiscale Entropy Analyses Based on Digital Camera Data

By changing the air and water flow relative rates in the two-phase (air-water) flow through a minichannel, we observe aggregation and partitioning of air bubbles and slugs of different sizes. An air bubble arrangement, which show non-periodic and periodic patterns. The spatiotemporal behaviour was recorded by a digital camera. Multiscale entropy analysis is a method of measuring the time series complexity. The main aim of the paper was testing the possibility of implementation of multiscale entropy for two-phase flow patterns classification. For better understanding, the dynamics of the two-phase flow patterns inside the minichannel histograms and wavelet methods were also used. In particular, we found a clear distinction between bubbles and slugs formations in terms of multiscale entropy. On the other hand, the intermediate region was effected by appearance of both forms in non-periodic and periodic sequences. The preliminary results were confirmed by using histograms and wavelets.

Tetiana Cherepova, Galyna Dmitrieva, Oleksandr Tisov, Oleksandr Dukhota, Myroslav Kindrachuk
Research on the Properties of Co-TiC and Ni-TiC HIP-Sintered Alloys

Three types of sintered alloys were fabricated based on cobalt, nickel and high-temperature alloy ZhS32-VI matrix with titanium carbide strengthening phase. TiC content was in a range of 30–50 vol. %. The melting temperatures of alloys are higher than 1320°C, and they may undergo undamaged through all technological procedures together with turbine blades, including soldering and outgassing. DSC analyses indicates no additional thermal effects until melting, which confirms their structural stability. The examinations of microstructure revealed three types of constituents – TiC particles, matrix solid solution and blow outs – structural defects having negative effects on all the studied properties. It was found that heat resistance of nickel based sintered alloys at the temperature of 1100°C is superior as compared with the alloys based on cobalt and alloy ZhS32-VI. It has been established that wear resistance in conditions of fretting wear at temperatures of 20, 850, 950 and 1050°C of sintered alloy with ZhS32-VI matrix is mostly superior as compared with the other alloys. The properties of produced alloys allow to use them for manufacturing of components of friction couples operating in conditions of high temperature fretting wear, including protective pads of turbine blades top shrouds contact faces.